Characterising the Lunar radiation environment using the Floating Gate Dosimeters

An evaluation of the Lunar Zebro payload

Stan Broere

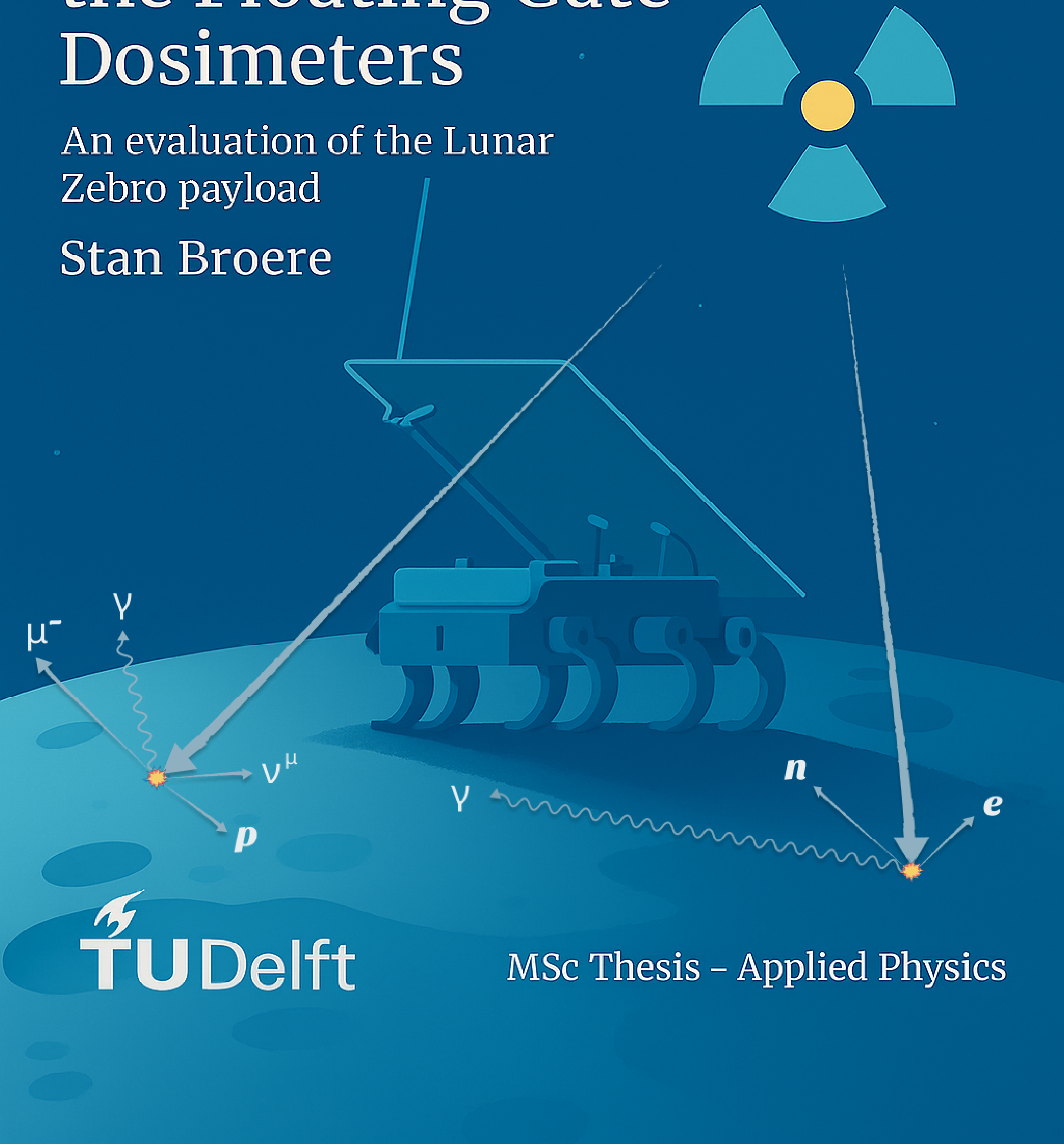

TU Delft

MSc Thesis – Applied Physics

Characterising the Lunar radiation environment using the Floating Gate Dosimeters

An evaluation of the Lunar Zebro payload

by

Stan Broere

to obtain the degree of Master of Science
at the Delft University of Technology,
To be defended publicly on Friday, 14 March 2025, at 14:00.

Student number:	5199298	
Project duration:	June 03, 2024 – March 14, 2025	
Thesis committee:	Dr. ir. D. Lathouwers,	TU Delft, Chair
	Dr. A Meniccuci,	TU Delft, Supervisor
	Dr. ing. J Plomp,	TU Delft, Supervisor
	Dr. H. Shut,	TU Delft, Examiner

Style: TU Delft Report Style, with modifications by Daan Zwaneveld

“We are all explorers. There is no complete map of space. Even the map we carry in our minds is an imperfect one, a sketch in the sand that is forever washed away.”

– Frank Herbert, *Dune*

Preface

This thesis focuses on investigating the Floating Gate Dosimeter (FGDOS), particularly in mixed-field environments, to assess its reliability for space applications. The study is motivated by the need for robust and radiation-hardened systems in future lunar exploration missions, where radiation exposure can significantly impact performance and longevity. This study aims to contribute to the development of more resilient hardware for future lunar missions.

My fascination with space, particle physics, and instrumentation has been a red thread throughout my studies. During my master's, I came into contact with Dr. Alessandra Menicucci, through a project related to developing and investigating radiation sensors for a lunar application. I was intrigued. When the literature review revealed the possibility of conducting measurements at CERN, it was the icing on the cake. This thesis is the result of my curiosity and passion for exploring the intersection of physics, electronics, and space technology.

I would like to express my gratitude to my supervisors, Dr. ir. Jeroen Plomp, Dr. ir. Danny Lathouwers, and Dr. Alessandra Menicucci, for their invaluable guidance and insightful discussions throughout this research. Their expertise has greatly shaped my understanding of conducting radiation experiments.

I would also like to thank the people at CERN CHARM for the opportunity and guidance—especially Dr. Salvatore Danzeca and Dr. Salvatore Fiore—for their expertise and support during my time at CHARM. Their insights into radiation effects and experimental techniques have been instrumental in shaping this work.

Furthermore, I would like to thank Michel Thijs, Lassi Tiihonen, Bartłomiej Dudek, Anthony Bats, Jasper van Dijk, Abhimanyu Shanbhag, Zamran Khan, Nicole Banga, and Ilse van der Kraaij for their support during the thesis.

I also extend my appreciation to the TU Delft Moonshot program for providing the funds that made this research possible.

Finally, I would like to thank my friends and family for their unwavering support, patience, and encouragement, especially during the challenging phases of this thesis. Their belief in me kept me motivated throughout this journey.

This thesis is written in the context of a Master in Applied Physics, specifically within the track of Instrumentation. As such, it presents the research from a predominantly physics perspective, though engineering aspects are also explored where relevant.

For those who may read this, I hope this work serves as a useful aid and sparks curiosity in this fascinating domain. And to future master's students interested in this topic—I am always open to discussing the results in more detail. Research is a continuous journey, and I look forward to seeing where the next steps will lead.

Stan Broere
Delft, March 2025

Summary

As humanity returns to the Moon, our understanding of its radiation environment remains incomplete. To address this gap, the Lunar Zebro rover, equipped with a state-of-the-art radiation payload, aims to improve our understanding. This is done by the use of Floating Gate Dosimeters (FGDOS), which convert radiation into electron-hole pairs that cause a discharge of charge on the floating gate, in turn enabling the measurement of radiation. This thesis examines the performance of the FGDOS and the Lunar Zebro radiation payload under various radiation conditions, evaluates their sensitivities, and outlines future research directions. To accomplish this, proton and gamma tests were conducted at HollandPTC and the Reactor Institute Delft (RID) to gauge the FGDOS response to different fluxes and particle types. This, in combination with a few functionality tests , such as temperature characterisation, allowed the foundation to be laid for conducting radiation measurements in a mixed-field radiation environment at CERN's Highly Accelerated Mixed-Field facility (CHARM). Here, the state-of-the-art payload was exposed to a range of energies and particles, allowing the lunar environment to a certain extent to be characterised. In addition, a layer of boron carbide was placed onto one of the FGDOS sensor to investigate the effect of neutron sensitivity.

Several key findings emerged from this research. First, a linear scaling was observed for both gamma and proton radiation as a function of dose rate, however the gamma measurement contain big uncertainties. The sensitivity measurement at HollandPTC and RID experiments were lower than expected, but consistent with previous studies by Meyere et al. [1] and Shanbhag et al. [2]. However, the sensitivity measured at CHARM was consistent with findings from Zimmaro et al. [3] and Sealicon[4]. Additionally, introducing a boron carbide layer led to a slight increase in neutron sensitivity, will the addition of shielding material reduce the sensitivity. A critical operational issue was identified in the radiation payload's Floating Gate Dosimeter, related to the recharging of the Floating Gate, likely caused by a firmware-related bug. Moreover, an increase in power consumption was observed as a function of the total ionizing dose. Finally, a sensitivity curve was established, showing its dependence on the charge stored on the floating gate.

The findings demonstrate that while the FGDOS has potential for radiation measurements on the lunar surface, the payload is not yet flight-ready. Challenges related to lower sensitivity, recharging, and discharge behaviour require further investigation. Additionally, the absence of a clear radiation simulation model leaves uncertainty regarding the expected radiation environment. A series of future work directions are postulated in this thesis, but in the short term, additional radiation tests should be conducted at facilities capable of providing high-flux Co-60 gamma, such as the ESA ESTEC Co-60 facility to overlap with previous research. Furthermore, a post-analysis of the CHARM setups is necessary to investigate the cause of the communication failure in one of the setups during the experiment. Finally, further investigations into neutron sensitivity would be of great interest for both future space missions and terrestrial applications.

Contents

List of Figures

List of Tables

List of symbols

Symbol	Definition	Unit
Q_{gen}	Generated charge	C (Coulomb)
E_{dep}	Deposited energy by ionizing particles	J (Joule)
W_{e-h}	Energy required to generate one electron-hole pair	eV (electron-volt)
ρ_{ox}	Oxide density	kg/m^3
A	Area	m^2
t_{ox}	Oxide thickness	m (meter)
D	Dose	Gy (Gray)
$R(\mathcal{E})$	Recombination rate influenced by the electric field	Dimensionless
Q_{col}	Collected charge	C (Coulomb)
C	Capacitance of the capacitor	F (Farad)
ϵ	Permittivity of the dielectric	F/m (Farad per meter)
V_{cap}	Voltage across the capacitor	V (Volt)
V_{init}	Initial voltage across the capacitor	V (Volt)
ΔV	Voltage variation across the capacitor	V (Volt)
$\mathcal{E}$	Electric field in the insulator	V/m (Volt per meter)
ϵ_r	Relative permittivity of the dielectric	Dimensionless
ϵ_0	Permittivity of free space	8.85 × 10^{-12} F/m
v	Speed of incident particle	m/s (Meter per second)
$R(E)$	Fraction of proton energy transferred during interaction	Dimensionless
$\frac{\mu_{\text{en}}}{\rho}$	Mass energy transfer coefficient	cm^2/g
Φ	Particle fluence	Particles/cm^2
k_{Gy}	Unit conversion parameter	1.6 × 10^{-7} Gy·g·MeV^{-1}
TID	Total ionizing dose	Gy (Gray)
S_r	Radiation sensitivity of the sensor	kHz/Gy
f_{sens}	FGDOS sensor output	Hz
f_{ref}	FGDOS reference component output	Hz
$\dot{D}$	Dose rate	Gy/s
I_r	Current	A (Ampere)
V_{init}	Initial FG voltage before irradiation	V (Volt)
D_r	FG constant	Dimensionless
V_r	Constant $\epsilon_r \cdot t_{\text{ox}}$	V (Volt)
v_r	Equivalent voltage noise	V (Volt)
S_m	Mass stopping power	MeV cm²/g
S	Stopping power	MeV/cm
k_{tp}	Ionization chamber correction for temperature and pressure	Dimensionless
P	Pressure	Pa (Pascal)
T	Temperature	K (Kelvin)
σ	Standard deviation	Dimensionless
N	Number of measurements	Dimensionless
ρ	Density of material	g/cm³
k_{nlr}	Non-linear dynamic range correction factor	Dimensionless
t	Time	s (Second)
n_{sens}	Sensor noise	Hz
τ	Recovery rate	s (Second)
n	Number of particles per second through beam	Particles/s
e	Charge of a single proton	1.602 × 10^{-19} C

Continued on next page

Continued from previous page

Symbol	**Definition**	**Unit**
E	Incident energy of particle	eV
σ_{cs}	Cross section	cm²
ϕ	Flux	Particles/cm²/s
dx	A distance traveled	m (Meter)
π	Pi (Mathematical constant)	3.1415
R_0	Nuclear radius	m (meter)
r_e	Electron radius	2.8179 × 10^{-15} m
m_e	Mass of electron	9.109 × 10^{-31} kg
c	Speed of light	299,792,458 m/s
N_A	Avogadro's number	6.022 × 10^{23} mol^{-1}
Z	Atomic number	Dimensionless
A_w	Atomic weight of absorbing material	g/mol
γ	Lorentz factor	Dimensionless
z	Charge of incident particle	C (Coulumb)
δ	Density correction	Dimensionless
I	Mean excitation potential	eV
W_{max}	Maximum transferable energy	eV
β	is the ratio of v to c	Dimensionless

Acronyms

Al	Aluminium	19
CERN	European Organization for Nuclear Research	38, 58
CHARM	CERN Highly-Accelerated Mixed Field Facility	38–40, 42, 56, 58, 59, 99, 106
CMEs	Coronal Mass Ejections	10
Co-60	Cobalt-60	24, 29, 30, 34–36, 43, 44
COTS	Commercial Off-The-Shelf	16, 36, 62
CraTER	Cosmic Ray Telescope for the Effects of Radiation	13, 14
Cs-137	Caesium-137	29, 30, 43, 44
Cu	Copper	39
DD	Displacement Damage	7, 9, 26, 39, 40
FG	Floating Gate	19–21, 23–25, 28, 33, 36, 52, 54, 60, 62, 85, 87
FGDOS	Floating Gate Dosimeter	1, 2, 17, 19, 23–25, 28, 30–32, 34–36, 40, 49, 53–55, 57, 60, 62, 74, 84, 88, 103, 108
FPGA	Field-Programmable Gate Arrays	8, 23
FSM	Finite State Machine	22
GCRs	Galactic Cosmic Rays	11, 13–15
HEH	High-energy Hadrons	39
HZE	High (H), Atomic Number (Z), and Energy (E)	11
I2C	Inter-Integrated Circuit [Communication Protocol]	75
IC	Intergrated Circuit	22, 33, 44, 54, 74, 81
IEL	Ionizing Energy Loss	5
IRRAD	CERN Proton Irradiation Facility	38
ISS	International Space Station	11
LEO	Low Earth Orbit	11
LET	Linear Energy Transfer	5, 11, 14, 35, 63, 106, 107
LND	Lunar Lander Neutron & Dosimetry	13, 14, 32, 35, 60, 62
LRO	Lunar Reconnaissance Orbiter	13, 14
MCU	Microcontroller Unit	23, 47, 49, 50, 52, 74
MISO	Master In, Slave Out	22, 75, 79
MOSFET	Metal-Oxide-Semiconductor Field-Effect Transistor	7
MOSI	Master Out, Slave In	22, 75, 79
NCS	Chip Select	22, 75, 79

NIEL	Non-Ionizing Energy Loss	5, 9
NIRQ	Inverted Interrupt Request	22
NSTBY	Inverted Standby Mode	22, 50
PCB	Printed Circuit Board	16, 57, 79, 81, 82
PS	Proton Synchrotron	38, 100
RID	Reactor Institute Delft	2, 29, 58, 60, 83, 84
SCK	Serial Clock	22, 75, 79
SCL	Serial Clock	75
SDA	Serial Data	75
SEB	Single Event Burnout	8
SEEs	Single Event Effects	7, 8, 40, 47, 50–54, 79, 99
SEFI	Single Event Functional Interrupt	8
SEGR	Single Event Gate Rupture	8
SEL	Single Event Latch-up	8, 64
SEPs	Solar Energetic Particles	10, 15
SET	Single Event Transient	8
SEU	Single Event Upset	8, 16, 40, 64
Si	Silicon	14, 80, 82, 84, 85, 103
Si02	Silicon dioxide	3, 19
SPE	Solar Particle Events	10, 54
SPI	Serial Peripheral Interface	22, 79
TID	Total Ionizing Dose	vii, 7, 16, 24–26, 35, 39, 40, 48, 49, 51–56, 87, 107, 108, 110
TU	Technical University	15
WCK	Window clock	75

1

Introduction

For millennia humanity has looked at the Moon in wonder and awe. But this decade, humankind is on the brink of a new age of deeper space exploration. As outlined in NASA's Artemis program, establishing a human presence on the lunar surface serves to lay down the groundwork for future missions to Mars and beyond. [5, 6]. However, one of the significant challenges of lunar missions is the intense and variable radiation environment, which poses significant risks to both robotic systems and humans. Prolonged exposure to this type of radiation can lead to data corruption, electronic component failure, and, for humans, an increased risk of cancer, acute radiation sickness, and long-term degenerative effects on the nervous and cardiovascular systems.[7, 8]. These hazardous environments requires innovative solutions to accurately and reliably monitor the robotic systems, and allow to mitigate potential failures and ensuring the safety and success of the lunar operation. In addition, the Moon is a historic archive of our Sun and Solar System. Scientific discoveries are locked in its regolith that could lead to an improved understanding of our own planet and its evolution [5, 6]. It also harbors resources, such as water, that are among the rarest and most precious commodities in space, offering potential sustenance and fuel for future explorers. Through radiation measurements, it is possible to learn more about the hidden scientific gems buried on the Moon . [5]

As outlined by the Artemis vision, humanity's return to the moon will begin with robots, with rovers being used to explore the surface of the moon more extensively than any human will in the near future. In recent decades, space robotics has undergone a paradigm shift, driving the development of miniaturised, modular, and cost-effective spacecraft, enabling more efficient and scalable space exploration[9, 10, 11]. The Lunar Zebro, a rover designed by the students of the TU Delft, is one of those endeavours. The aim of the rover is to demonstrate the usefulness of a nano-rover concept on the Moon, with the eventual aim for a more ambitious goal, like operating a swarm of rovers on an extra-terrestrial body [12, 13]. To this extent, a scientific measurement device was constructed, referred to as the "Radiation payload"[1], to investigate the radiation environment on the lunar surface. Surprisingly, the radiation environment on the lunar surface is not well understood. In recent history, a couple of missions have measured the radiation environment using flyby and landers[14, 15, 16, 17]. These missions have provided valuable insights into the lunar radiation environment. However, no dedicated radiation rover has ever been deployed on the lunar surface. To bridge this gap, physical radiation transport models are used to enhance scientific understanding by simulating how cosmic rays and solar energetic particles interact with the lunar surface[18]. However, uncertainties in the input parameters can lead to significant variations in model predictions, making additional experimental measurements essential for validation and refinement.

To address this, the Radiation Payload is equipped with four Floating Gate Dosimeter (FGDOS) sensors, which enable measurements of accumulated radiation dose and, to a certain extent, the dose rate. This data will help validate existing radiation models and improve our understanding of radiation exposure

---

[1] A payload is the instruments or equipment carried by spacecraft, satellite, or rover, designed to fulfill a mission objective, such as data collection and communication.

in the lunar environment.

In this thesis, the effectiveness of the current Lunar Zebro payload in characterising the lunar radiation environment is examined, along with potential improvements for future missions. To address this, two research questions were formulated:

- What are the characteristics of the current radiation payload, including the FGDOS sensor, under mission conditions with respect to different types of radiation?
- How can the current radiation payload be optimised to enhance scientific data collection?

To answer these questions, experiments were conducted using gamma radiation, protons, and mixed fields at different facilities, namely Reactor Institute Delft (RID), HollandPTC, and CERN.

The structure of this thesis is designed to guide the reader through the progression of the research. Until now the borders of this thesis are sketch, but chapter 2, will give color to the outline by guiding the reader through the relevant background theory, with each next section building onto the previous one. After an understanding is obtained of the fundamental literature, chapter 3 will explore the experiments conducted at RID to investigate the behavior of the sensor to gamma irradiation, particular low dose rates (uGy/h). This is followed up by chapter 4, which covers the irradiation mission at CERN CHARM, where electronic components can be irradiated in a mixed-field, allowing to study the current design in a radiation environment similar to its operation environment. Finally, chapter 5 will revisit the original research questions posed earlier and provide a summary of the key findings. Based on these insights, chapter 6 will outline recommendations for future research and potential improvements.

Supplementary information can be found in Appendix A, Appendix B, Appendix C, which includes details on the HollandPTC irradiation test, a guide to temperature compensation for the FGDOS, and a more in-depth explanation of the hardware used.

Additionally, Appendix F contains additional plots and images to provide further insight into various aspects of the study. An exploratory investigation into the use of the Timepix detector is discussed in Appendix G.

Finally, Appendix E, Appendix I, Appendix J and Appendix H include additional literature and supporting information relevant to the main research conducted in this thesis.

2

Literature review

This chapter focuses on the literature necessary to understand the research. In section 2.1, the radiation mechanism is introduced. This is followed by a discussion on the radiation environments in outer space and on the lunar surface, in section 2.2 and section 2.3, respectively. Building on this knowledge, section 2.4 provides a brief introduction to the Lunar Zebro rover, including its mission and system. Finally, with all the obtained information, the radiation sensor, namely the Floating Gate Dosimeter, is introduced in section 2.4.

2.1. Radiation Mechanisms

This thesis places significant emphasis on radiation. For this reason, it is important to understand the effects that different types of particles have, with the knowledge built from the ground up. This section will explain the key particles of the Standard Model and their interactions with one another. This will lead to the effects of radiation on electronics, discussed in subsection 2.1.3.

2.1.1. Particle interaction

The interactions between particles are determined by their properties and energy levels. In this thesis, the focus will primarily be on the interactions of photons, charged particles, and neutrons with Si02. Each type of interaction is briefly explained below.

Photons

Photons can interact with atoms through three primary interaction mechanisms, which are illustrated in Figure 2.1

- **Photoelectric Effect:** In this phenomenon, the photon transfers its energy to an electron. If the photon's energy exceeds the electron's binding energy, the electron is ejected from its atomic cloud. The interaction is with the atom as a whole and cannot take place with a free electron [19, 20]
- **Compton Scattering:** The incoming gamma-ray photon is deflected through an angle θ with respect to its original direction. The photon transfers a portion of its energy to the electron (assumed to be initially at rest). The remaining energy is retained by the photon, resulting in a longer wavelength and a scattered trajectory. Because all angles of scattering are possible, the energy transferred to the electron can vary from zero to a large fraction of the gamma-ray energy [19, 20, 21]
- **Pair Production:** For this process to occur, the photon must pass near an atomic nucleus and have energy exceeding the threshold of $2m_ec^2$, where m_e is the mass of the electron and c is the speed of light in a vacuum. The photon is entirely absorbed, leading to the creation of an electron-positron pair.[19, 20, 21]

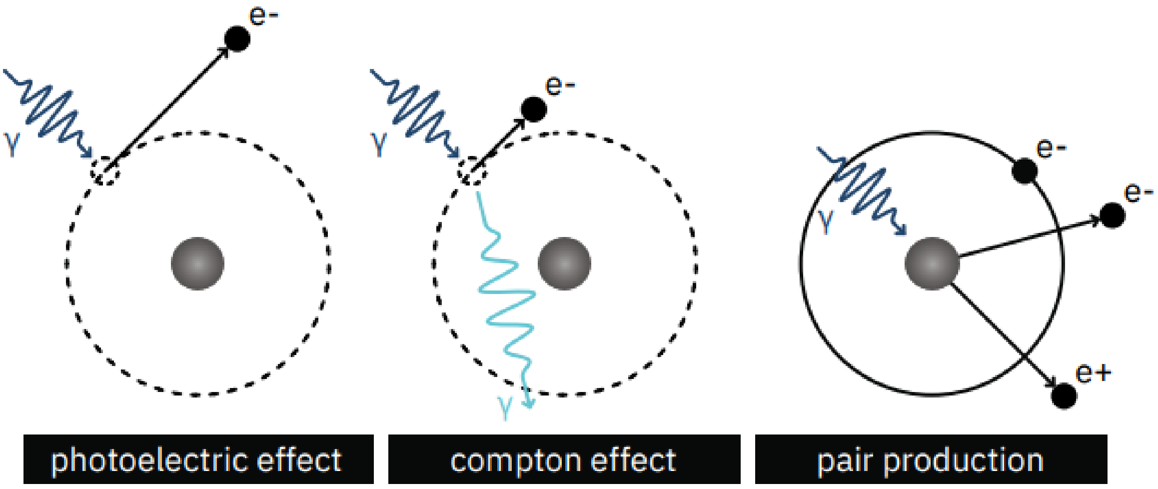

Figure 2.1: Illustration of photon-matter interactions [22]

Charged particles
In the standard model, there are a bunch of particles that contain an electrical charge (q $\neq 0$ C). This includes pions, protons, kaons, muons, etc. This interaction is shown in figure Figure 2.2 and explain below:

- **Excitation**: When a charged particle travels close to an orbiting electron with an energy lower than the binding energy of the electron, the electron will absorb this energy and move into a higher energy state. After some time, the electron will fall back to its original state and emit a photon in the process. [19, 20, 21]
- **Bremsstrahlung**: When a particle without much mass (e.g. an electron) passes past the nucleus of an atom, the electric field of the nucleus can deflect the charged particle. The particle then loses some of its energy which is emitted as a photon.[19, 20, 21]
- **Ionization**: When a charged particle travels through an electron cloud with an energy higher than the binding energy of the electron, the electron can be ejected from the cloud.[19, 20, 21]

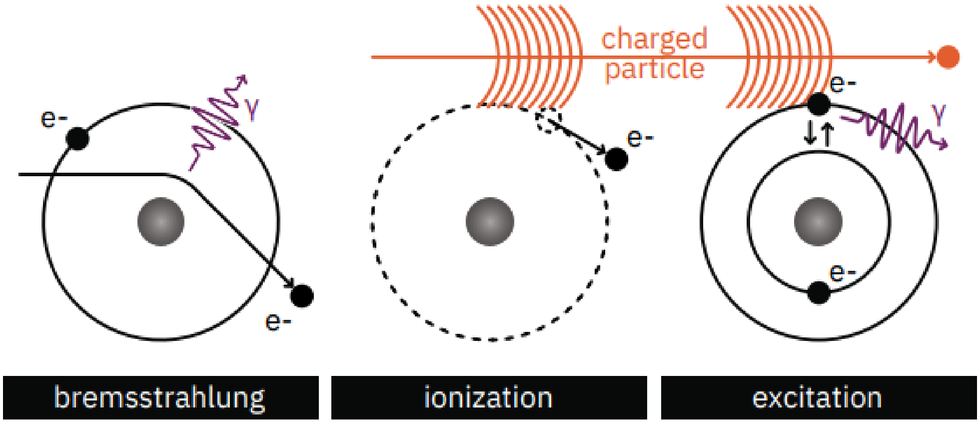

Figure 2.2: Illustration of charged particle-matter interactions. [22]

Neutrons
Neutrons are nearly identical to protons in terms of mass and nuclear properties, with the primary distinction being their lack of electric charge. This means that neutrons only interaction mechanism is via nuclear interactions, as can be seen in Figure 2.3.

- **Absorption/capture**: When a neutron (mostly thermal neutrons that have an energy higher than 24 MeV) hits the nucleus, the energy of the nucleus is increased and is left in an excited state. This energy is later released by the release of a photon.
- **Fission**: A neutron that is absorbed by a very heavy nucleus, the nucleus can split into smaller nuclei also referred to as fission fragments. This is also energy released in the form of photon emission.
- **Inelastic scattering**: A neutron is absorbed by the nucleus. Subsequently, the nucleus emits a neutron of lower energy than the striking neutron and the nucleus stays in an excited state while being scattered. Later, the energy is released by photon emission.
- **Elastic scattering**: A neutron that strikes the nucleus transfers part of its energy to the nucleus. Both the neutron and the nucleus are scattered. [19, 20, 21]

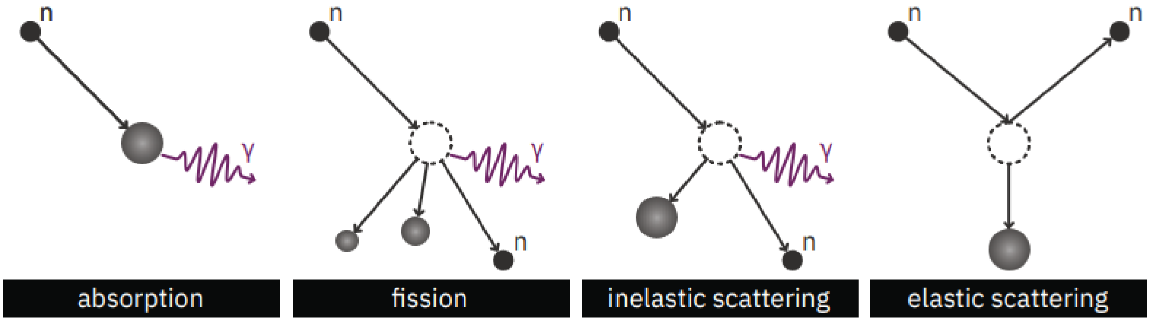

Figure 2.3: Illustration of neutrons-matter interactions [22].

2.1.2. Energy loss

When a particle collides with matter, it can cause ionization as a consequence. Direct ionization occurs if the particle transfers energy, such that it is sufficient to eject electrons from atoms, forming ions. In such instances, the primary particle may further produce secondary particles which might indirectly cause ionization which is termed as indirect ionization.

As a result of passing through matter, particles lose energy through any number of mechanisms which can be generally grouped into Ionizing Energy Loss (IEL) and Non-Ionizing Energy Loss (NIEL) [21].

Ionizing Energy Loss (IEL) refers to the loss of energy in processes such as ionization, where atoms are directly ionized, for example, through the photoelectric effect.

Non-ionizing energy Loss (NIEL) is the loss of energy that occurs without ionization. These include nuclear displacements which cause displacement damage, pair production, or emission of bremsstrahlung radiation. These interactions eventually expend the particle's energy until it has been completely absorbed or stopped.

To determine the amount of energy that inline particles lose as they move through a material, a general concept is the *stopping power* (S) and is defined as,

$$S = -\frac{dE}{dx} = -LET, \tag{2.1}$$

which is defined as the differential energy loss dE divided by the differential path length dx. The Linear Energie Transfer (LET) is an indicator of the amount of energy absorbed in the material and is usually measured in Mev/cm [23].

In the radiation effects community, stopping power is commonly normalized by the mass density of the material (ρ), resulting in a quantity that is independent of the material's phase. This quantity is known as the *mass stopping power* (S_m), and since energy loss occurs due to interactions with both electrons (elec) and nuclei (nuc) in the medium, it is commonly expressed as the sum of two contributions [23], namely:

$$S_m = -\frac{1}{\rho}\frac{dE}{dx}\bigg|_{elec} - \frac{1}{\rho}\frac{dE}{dx}\bigg|_{nuc} . \tag{2.2}$$

The stopping power depends not only on the particle type but also on its energy and the target material where ionisation takes place. Figure 2.4 shows the stopping power for different ions in silicon.

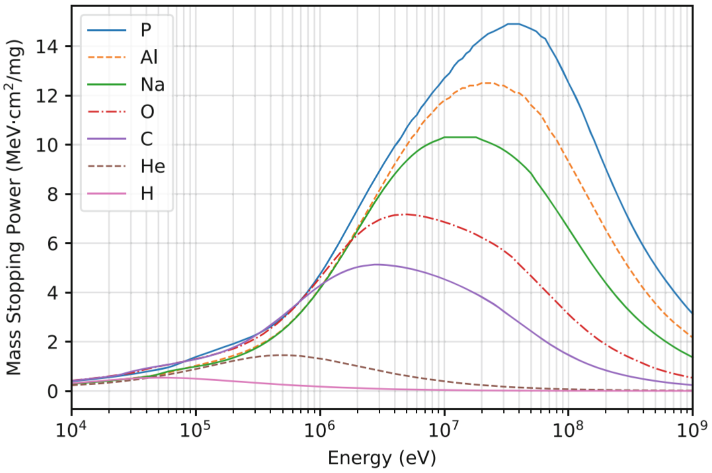

Figure 2.4: Variation of the stopping power as a function of energy for different ions in silicon, with hydrogen (protons) being the lowest ion and phosphorus the highest ion [23].

2.1.3. Radiation Effects on Microelectronics

When particles interact with microelectronics, they alter the material's properties, potentially degrading its performance and functionality. These interactions can be classified into three main categories: Total ionizing dose (TID), Single event effects (SEEs), and Displacement damage (DD)[24]. Each category is briefly described below:

Total Ionizing Dose

Total ionizing dose (TID) effects occur when ionizing radiation interacts with semiconductor materials, leading to the formation of electron-hole pairs. When high-energy particles pass through the material, they displace electrons from their atomic orbitals. If the energy transferred exceeds the material's ionization threshold, secondary interactions can amplify the effect, allowing a single high-energy particle to generate thousands of electron-hole pairs.[21, 24]

In MOSFET devices, these pairs are predominantly formed in the oxide layer. Under the influence of an electric field, the generated electrons and holes begin to move. While most electrons are quickly removed from the oxide, some holes become trapped near the interface between the oxide and the silicon substrate. This charge build-up (see (1) in Figure 2.5) at the interface gradually disrupts the electrical behavior of the device, leading to degradation of critical performance parameters such as threshold voltage and channel mobility [25].

Additionally, the accumulation of holes near the silicon-oxide boundary (see (3) in Figure 2.5), can result in the formation of interface traps, which further alter the electrical properties of the semiconductor. These traps contribute to long-term device degradation, as they shift key operational characteristics and reduce the overall reliability of the microelectronics[21].

An mathematical derivation of TID in mixed field environments is discussed in Appendix I

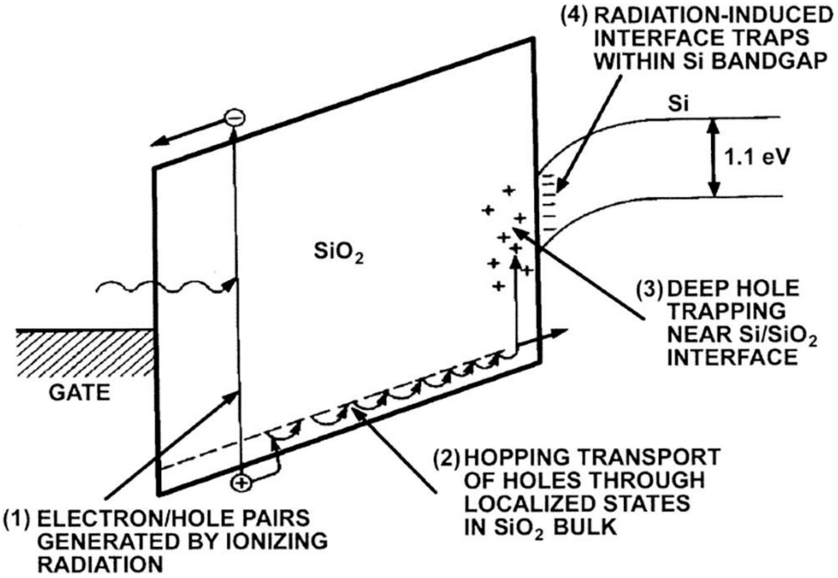

Figure 2.5: Total ionizing doses (TID) mechanisms in SiO2. [26]

Single Event Effects

Single Event Effects (SEEs) describe various phenomena where a single energetic particle disrupts the operation of electronic devices. These disruptions can range from temporary malfunctions to permanent hardware damage. The particles most commonly responsible for SEEs include hadrons, neutrons, and heavy ions. While heavy ions primarily cause SEEs through ionization in sensitive regions of semiconductors, hadrons, and neutrons typically generate localized charge through nuclear interactions within or near the semiconductor material[23, 25].

SEEs can be classified into two main categories: destructive and non-destructive. Destructive events, often involving high currents, can cause irreversible hardware damage. In contrast, non-destructive events are temporary, leading to issues such as corrupted data or unintended changes in the device's operational state—typically software-related failures[23, 25].

The underlying mechanisms of SEEs involve three key steps. First, as a particle passes through the semiconductor, it generates electron-hole pairs, creating localized charge. Next, the charges drift under the influence of an electric field, inducing a transient current. Finally, the charges diffuse over time, gradually reducing the current. These processes, which ultimately lead to SEEs[23, 27], are illustrated in Figure 2.6.

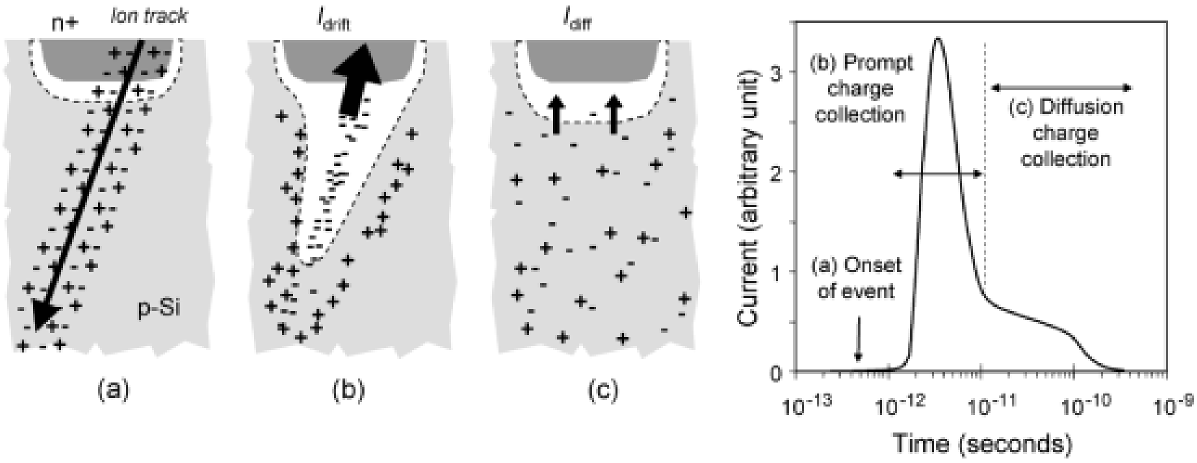

Figure 2.6: Schematic representation of charge collection in a silicon junction: (a) immediately after an ion strike, (b) during prompt (drift) collection, and (c) during diffusion collection. (d) shows a graph of the junction current induced as a function of time.[28]

SEEs have a wide range of effects, and their impact depends on the specific interaction and the type of device affected. Table 2.1 provides a detailed of some SEE types, their definitions, and whether they result in destructive or non-destructive outcomes. This understanding is essential for mitigating SEE-related risks in electronic systems, particularly those used in radiation-prone environments.

Table 2.1: Types of Single Event Effects (SEEs) with definitions and destructiveness[23, 25]

SEE Type	**Definition**	**Destructive?**
Single Event Upset (SEU)	Occurs in digital circuits when a particle strike changes the state of data stored in elements like flip-flops, latches, or memory bits.	No, recoverable via a soft reboot.
Single Event Functional Interrupt (SEFI)	A soft error that causes the component to reset, lock up, or otherwise malfunction. Interruptions caused by a particle strike. Typically occurs in configuration registers of processors, FPGA, or SDRAMs.	No, reset by software or power cycling. Stored data may or may not be lost.
Single Event Transient (SET)	SETs are voltage spikes or glitches caused by a particle strike. They occur in non-latched elements like combinational logic, clock lines, or control lines and can propagate depending on the pulse width and transistor capacitance.	No, but increased sensitivity due to technology scaling poses risks.
Single Event Latch-up (SEL)	SELs involve an abnormally high current state caused by a particle strike in sensitive regions of a device, potentially leading to function loss.	Yes, if power is not quickly removed, catastrophic failure due to overheating or bond wire damage can occur.
Single Event Gate Rupture (SEGR)	SEGRs occur when a particle strike creates a conductive path through the gate oxide or any dielectric layer, leading to increased gate leakage current.	Yes, can degrade or destroy the device.
Single Event Burnout (SEB)	SEBs happen when a particle strike induces a high current state in a device, which, if not controlled, leads to thermal runaway and failure.	Yes, can cause catastrophic thermal damage.

Displacement damage

Displacement damage (DD) refers to the dislodging of atoms from their normal lattice sites in a target material by impinging energetic radiation, creating interstitials . The empty spots left behind are called vacancies. These interstitials and vacancies are mobile, and they can cluster together or interact with impurities in the lattice, forming stable defect centers, as illustrated in Figure 2.7. Radiation-induced defect centers are responsible for a range of parameter degradation effects in components [29].

Energetic particles such as neutrons, protons, electrons, α-particles, and heavy ions can damage semiconductor materials by displacing atoms in the crystal lattice. Secondary electrons generated by high-energy photons also contribute to displacement damage. This results in stable defect states forming within the bandgap, which can cause various effects depending on factors such as temperature, carrier concentration, and the defect site's location. These effects include: (a) Enhanced thermal generation; (b) Enhanced recombination; (c) Enhanced temporary trapping; (d) Reduced carrier concentration [25, 29].

DD is particularly critical in semiconductors that rely on minority carrier current flow. As noted earlier, the NIEL is a widely used parameter to quantify degradation caused by DD. Research has shown that many radiation effects contribute to defect formation in materials scale linearly with NIEL. [29, 30]

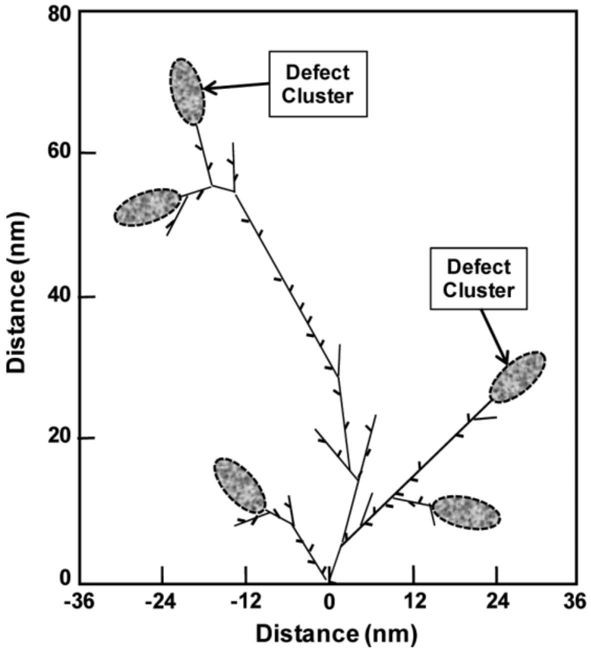

Figure 2.7: Conceptual illustration of the damage produced in Si by a 50-keV primary recoil atom. Isolated defects and amorphous defect clusters are shown[29]

2.2. Space radiation environment

Space radiation arises from the Sun and other astronomical bodies in our universe, comprising a mixed field of high-energetic particles such as electrons, protons, gamma rays, and heavy charge ions ranging from a few MeV to many TeV[31]. The flux and intensity of space radiation vary depending on the environment of observation and the source. In general, space radiation can be divided into three categories:

2.2.1. The Sun

The Sun, a massive sphere of hot plasma, generates its immense energy through nuclear fusion at its core[32]. Alongside electromagnetic radiation, the Sun emits a continuous stream of charged particles, primarily protons, electrons, and alpha particles, collectively known as solar wind. These particles, forming a flow of ionized plasma, possess velocities between about 300 and 800 $km\ s^{-1}$ [33]. The Sun's activity is modulated by the solar cycle, a periodic change in solar phenomena occurring roughly every 11 years (see Figure 2.8). This cycle influences solar irradiance, the frequency of solar flares, and Coronal Mass Ejections (CMEs). CMEs, significant releases of plasma from the Sun's corona, carry elevated levels of radiation. During these events, Solar Energetic Particles (SEPs) are accelerated outward into the solar system, often during violent and sporadic phenomena referred to as Solar Particle Events (SPE)[32, 33].

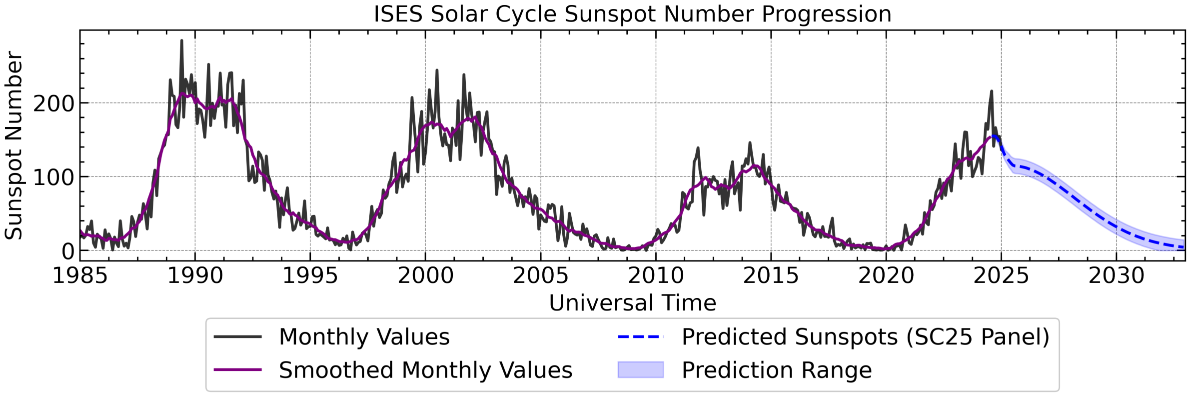

Figure 2.8: The number of sunspots as a function of time. The purple line represents a 13-month weighted, smoothed version of the monthly averaged data. Data obtained from National Oceanic and Atmospheric Administration (NOAA) [34].

During an SPE, SEPs can experience rapid energy and flux increases, reaching peak values of up to several GeV per nucleon, and can reach Earth in timescales as short as minutes following an eruption[33]. While SPE are more likely to occur during the solar maximum phase of the solar cycle, their occurrence is not strictly predictable. On average, approximately 40 SPE [35] (event exceeding energy above 30 MeV) are observed during each solar cycle. Despite being relatively infrequent and short-lived, these events can pose significant hazards to spacecraft and crew, highlighting the importance of studying their behavior and effects, particularly in the context of space exploration and radiation shielding[32, 33].

2.2.2. The Allen Radiation belts

The Earth's magnetic field is a dipole field generated by the movement of liquid metal in its outer core[36]. This magnetic field forms a protective bubble around the planet, known as the magnetosphere, which traps energetic charged particles. These trapped particles create two regions called the Van Allen radiation belts[37].

The inner belts stretch from about 600 km to 10,000 km above the Earth's surface and contain 10-100 MeV protons and 10-100 keV electrons. Most of these particles come from the solar wind or are produced by cosmic rays interacting with the atmosphere[38].

The outer belts lie farther out, between 13,000 km and 40,000 km above the surface. It is made up mainly of high-energy electrons, with energies ranging from 0.1 MeV to 10 MeV. Unlike the relatively stable inner belt, the outer belt is more variable and can change significantly depending on geomagnetic activity[38].

These radiation belts are an important area of research, especially for understanding space weather and its effects on satellites, astronauts, and Earth's magnetic field. [15, 38, 39].

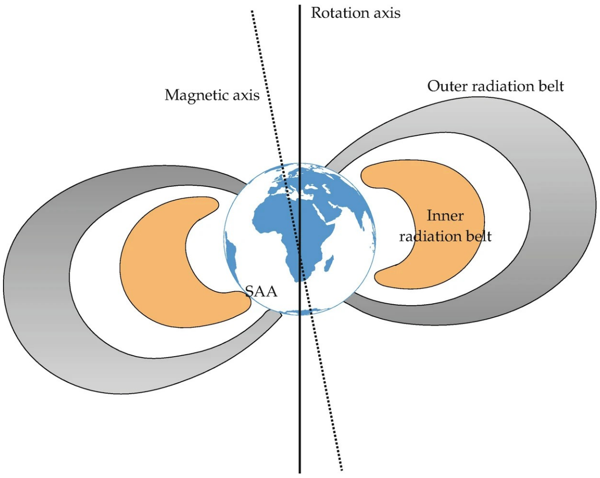

Figure 2.9: Visualisation of the Van Allen radiation belts, highlighting the relative positions of the inner and outer belts around the Earth. The South Atlantic Anomaly (SAA) is also indicated[40].

2.2.3. The Universe: Galactic Cosmic Rays (GCRs)

Another significant source of radiation in space is GCRs, which are high-energy particles originating from outside the solar system, starting at energies of 1 MeV and continuing to around 10^{15} MeV [41], as can be seen in Figure 2.10. GCRs represent a substantial portion of the radiation exposure affecting electronics used in spacecraft operating beyond LEO [39].

Possible sources of GCRs include neutron stars, pulsars, active galactic nuclei, supernovae, and hypernovae explosions. However, due to interactions with the interstellar magnetic field, the precise origin of GCRs remains uncertain, and they are generally thought to arrive isotropically from all directions outside the solar system [42].

GCRs are primarily composed of baryons (approximately 98%) and a smaller fraction of electrons (about 2%). The baryonic component comprises roughly 85% protons, 14% alpha particles, and the remainder includes high-energy, high-charge ions and nuclei, known as HZE particles [42]. These HZE particles are particularly significant due to their high LET, mass, and charge, which enable them to penetrate deeply and contribute substantially to radiation damage and dose[33]. In addition to this, antimatter, such as antiprotons and positrons, is also part of the composition[41].

GCRs are a relatively constant component of the space radiation environment, but their intensity is modulated by solar activity. For example, during periods of high solar activity, the increased solar wind can partially shield spacecraft from GCRs, reducing their intensity. GCRs account for approximately 80% of the effective radiation dose experienced by astronauts aboard spacecraft like the ISS[33].

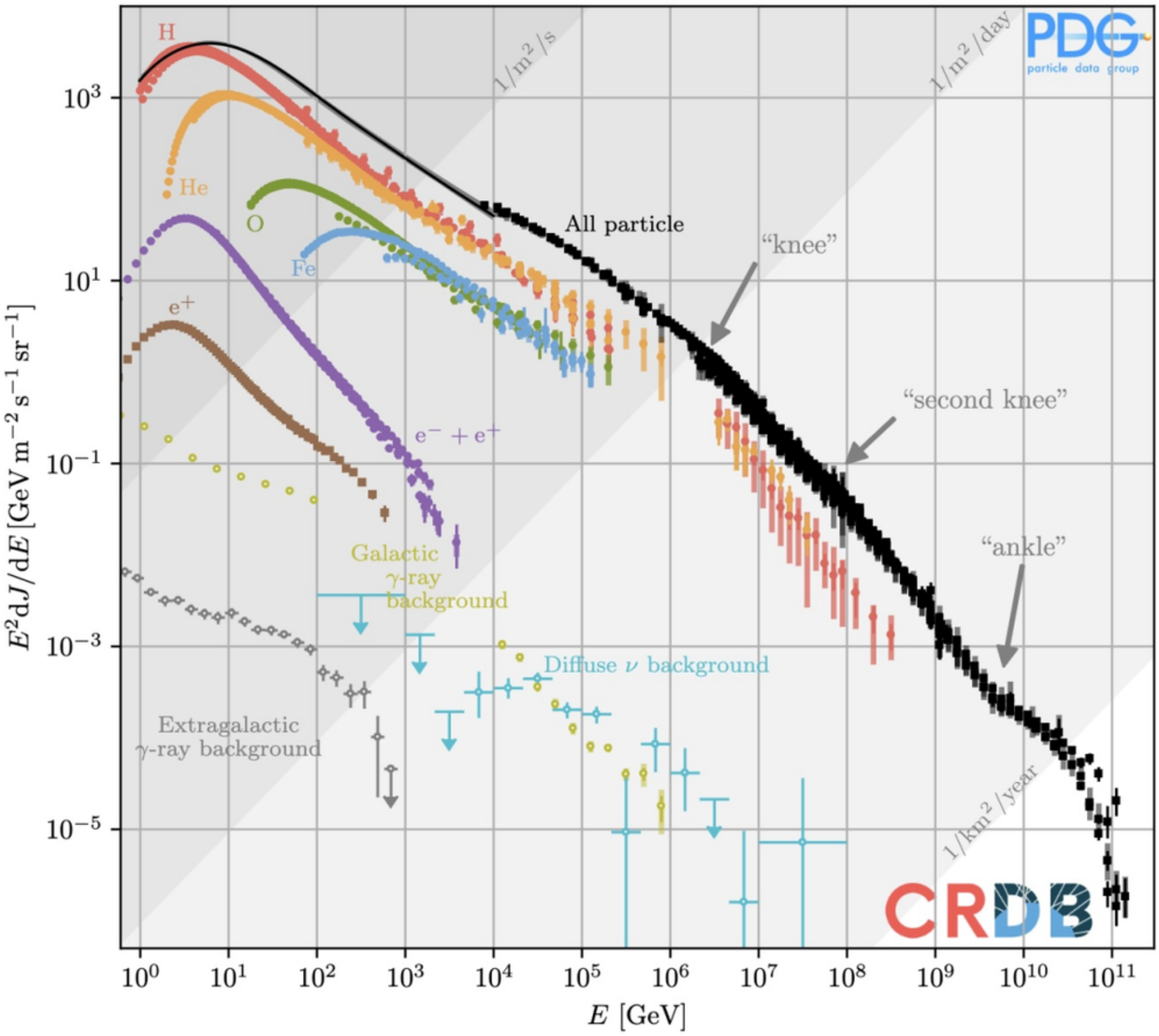

Figure 2.10: The spectrum of cosmic rays. Shown are measurements of the intensity of charged and neutral cosmic rays, multiplied by kinetic energy squared. Energy-integrated intensities are indicated by the various diagonal lines[43]

2.3. Lunar radiation environment

When traveling to the Moon, spacecraft will interact with all three sources of radiation mentioned in section 2.2. However, the radiation environment on the Moon is markedly different from that on Earth. Unlike Earth, the Moon lacks a magnetosphere, which means it cannot deflect or trap incoming charged particles from external sources. Additionally, the Moon has no significant atmosphere to attenuate or shield against incident radiation before it reaches the surface [44].

Particles originating from the Sun or GCRs interact with the lunar regolith, where they are scattered and reflected, producing secondary radiation [45].

Direct measurements of lunar surface radiation remain limited. However, in recent years, several missions have conducted radiation measurements both in orbit and on the lunar surface. Notable examples include:

- CraTER aboard the LRO (2009–present) [46], which operates at an altitude of 50 km.
- RADOM on Chandrayaan-1 (October 2008 – August 2009) in its 100 km orbit [15].
- LND aboard the Chang'E-4 lander, which landed on 3 January 2019 [16].

The RADOM instrument measured an absorbed dose rate of 0.227 mGy per day, averaged over 3,545 hours of measurement time while in a circular polar lunar orbit [15]. Similarly, CraTER measured a radiation exposure of approximately 0.372 mGy(Si) per day in its 50 km orbit [18]. Additionally, a total integrated dose of about 0.7 Gy was reported after 5.5 years [47][1].

Active radiation measurements

The LND experiment was the first instrument to perform active, time-resolved measurements on the lunar surface [16, 48]. It was deployed aboard the Chinese Chang'E 4 lander, which descended into the Aitken Basin, and its operation coincided with the solar minimum phase.

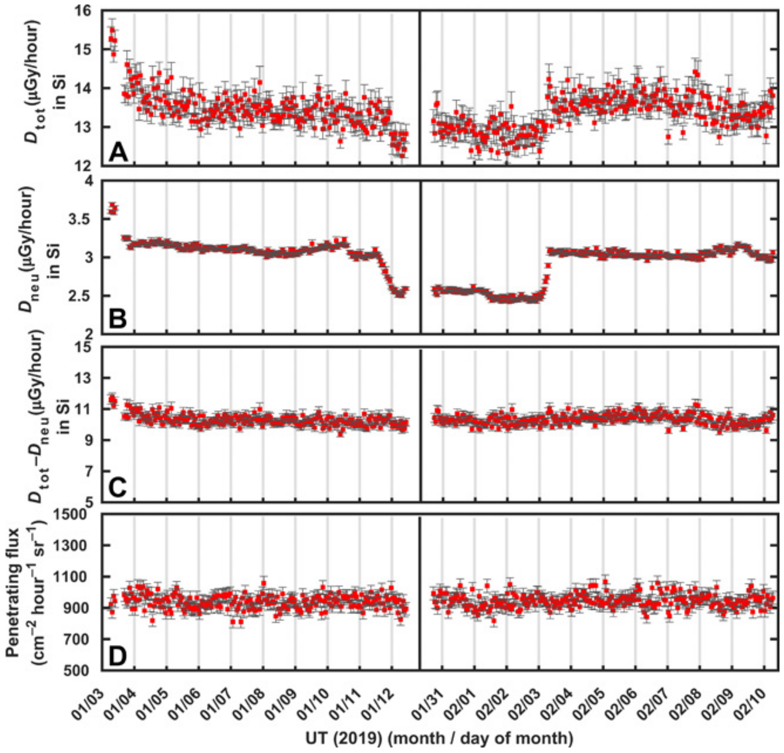

Figure 2.11: Temporal evolution of the radiation environment on the Moon as measured by LND on Chang'E 4 during the first and second lunar day after Chang'E4 landed. The left-hand panels show data for the first lunar day, and the right-hand panels show data for the second lunar day. UT, universal time [16].

---

[1] See Figure 1 in E. Zeitlin et al. [47]

The LND is a silicon-based particle telescope consisting of 10 dual-segment detectors. The addition of conversion foils allows the measurement of neutral particles in conjunction with charged particles. The instrument provides several key measurements[48]:

- Dose rates in silicon from both charged and neutral particles, resolved in time
- Linear energy transfer (LET) spectra
- Charged particle energy spectra
- Thermal neutron count rates
- Energy deposition spectra of neutral particles

LND was also designed to detect fast particles and thermal neutrons, which are secondary radiation produced by interactions between high-energy particles and the lunar surface. The absorbed dose rate measured by LND in silicon (Si)was approximately $13.2 \pm 1\,\mu\mathrm{Gy/h}$, while the dose rate from neutral particles was around $3.1 \pm 0.5\,\mu\mathrm{Gy/h}$ [16], as can be seen in Figure 2.11

Despite these achievements, certain uncertainties were associated with the measurements:

- Noise characterization was conducted before launch, so changes in noise sources during the mission could not be accounted for.
- The exact shielding provided to the LND instrument by the Chang'E 4 lander was unknown and was estimated based on the best available information about spacecraft materials and construction [16].

The current understanding of the radiation environment on the Moon's surface comes mainly from radiation transport models, which use inputs like galactic cosmic ray spectra and solar particle events. While these models are based on solid physical principles, uncertainties in their inputs and interpretations can lead to significant differences in the predicted total absorbed dose rate or dose equivalent rate [49].

Using the detectors mentioned earlier, Spence et al. [18] combined CraTER data from the LRO with simulations by Looper et al. [50] to estimate the dose rate at the skin during a prolonged solar minimum to be about 2.88 mSv/d. They found that around 91.4% of the total absorbed dose near the Moon is due to GCRs, with the other 8.6% coming from "albedo" particles—those reflected, scattered, or created as secondary radiation. The precise contributions are shown in Figure 2.12.

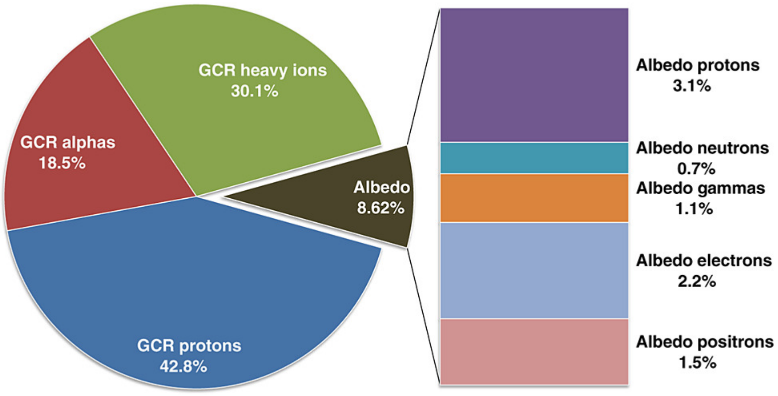

Figure 2.12: Contribution of various sources (from GCRs) to the absorbed dose rate on the lunar surface[18].

2.4. Lunar Zebro: A Lunar Nano-Rover from TU Delft

Building on the previous section of space and lunar radiation environment, this section shifts the focus on the Lunar Zebro rover, a small lunar rover developed by students at TU Delft. The project started in 2017 as a space-focused extension of the Zebro project under the TU Delft Robotics Institute [51, 52]. The project aims to make space exploration more affordable and reliable by using swarm robotics and simple, robust designs. The section will begin with an overview of the rover, providing a brief introduction to its purpose and features, before gradually transitioning to the design and specifics of the currently developed scientific instrument, the "Radiation Payload" .

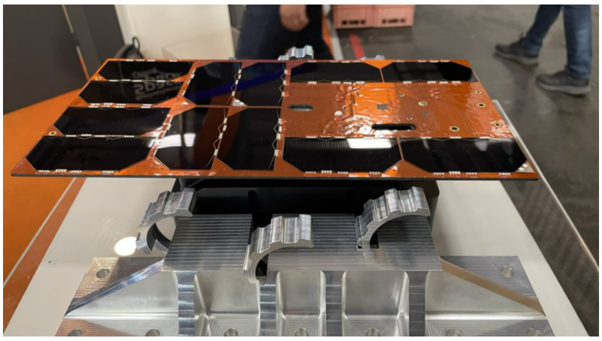

Figure 2.13: The Lunar Zebro rover, as presented during IAC2024

2.4.1. Mission and scientific objectives

As shown in Figure 2.13, the Lunar Zebro rover features a six-legged, C-shaped design. The first mission aims to send a single rover to the Moon to test its capabilities over one lunar day (approximately 14 Earth days) [53]. This duration was chosen due to the extreme temperatures experienced during the lunar night, which could prevent the rover from functioning. Efforts are underway to address this challenge, but for now, the focus of the first mission is on conducting scientific experiments and evaluating the rover's technology in the lunar environment.

The mission will test several key technologies developed for the Lunar Zebro rover [52]:

- Operating a miniaturized rover on the Moon.
- Running a custom-built Electronic Power System (EPS).
- Demonstrate the rover's capability for semi-autonomous navigation.
- Testing the unique *C-shaped legs* on rough lunar terrain.
- Communicating directly with Earth using low-power electronics.
- Navigating the lunar surface with vision-based obstacle detection software.

A significant advantage of the Lunar Zebro rover compared to stationary landers is its mobility. The rover can measure radiation at multiple locations across the lunar surface, providing detailed insights into how radiation levels vary. By equipping the rover with multiple radiation sensors, the mission aims to study the effects of scattering, secondary radiation, and environmental features in greater detail.

The scientific objectives of this mission include, but remain somewhat flexible:

- Observing *SEPs* to validate models of the solar wind and heliosphere.
- Measuring *GCRs*, such as protons and heavy ions, to improve the design of small, radiation-resistant systems for space applications.
- Investigating how lunar radiation levels vary with solar activity.
- Understanding how geological features, such as craters and hills, influence radiation shielding and reflection.

The data collected from this mission will provide insights into the effects of lunar radiation on both electronics and robotics, which is crucial for improving the reliability and durability of space systems. These measurements will also inform the design of future rovers and payloads, enabling the development of more robust and effective instruments for lunar exploration.

In the medium term, this mission lays the groundwork for deploying multiple rovers on the Moon, where coordinated efforts can significantly enhance exploration efficiency. By leveraging swarm robotics, future missions will be able to cover larger areas and gather more data than what a single rover can achieve [54].

In the long term, the Lunar Zebro project aims to transform the way robotic space exploration is conducted. By deploying swarms of small, low-cost, and durable rovers working together, the project seeks to make planetary exploration faster, more accessible, and better suited to challenging environments. This approach has the potential to accelerate discoveries and redefine how we explore other celestial bodies.

2.4.2. Radiation Payload

The *Radiation Payload* was chosen as the main scientific instrument after several design reviews [53, 55, 56], with as goal to measure the radiation directly on the lunar surface. A prototype of the Lunar Zebro Radiation Payload was designed, developed, and subjected to rigorous testing to validate its performance by Shanbhag [2] which built on the work of De Meyere [1] characterization of the radiation sensor, the Floating gate dosimeter (see section 2.5.) This section provides a concise summary of the payload's design process, objectives, and testing outcomes.

For the full design and development of the Lunar Zebro Radiation Payload, employing the V-Model methodology, readers are referred to Shanbhag [2, Chapter 3]

Mission Objectives

The design of the radiation payload was guided by the following mission objectives:

1. To measure exposure to ionizing radiation on the lunar surface.
2. To characterize the radiation environment for lunar missions at various locations, spanning from Earth orbit to the lunar surface.
3. To evaluate the shielding effectiveness of the Lunar Zebro rover's structure in protecting its internal subsystems and components.

Stakeholder Requirements

The payload was developed to meet specific stakeholder requirements, including:

1. A minimum radiation dose measurement range of 100 Gy, with survivability in the mission's radiation environment.
2. Radiation tolerance and low power consumption (<1 W).
3. Compact size (<50 × 50 × 50 mm) and lightweight construction (<100 g).
4. Use of commercial off the shelf (COTS) components to minimize development complexity and cost.

System Requirements

Building on stakeholder requirements, detailed system specifications were defined as follows:

1. The capability for time-resolved radiation measurements.
2. A total payload mass of less than 50 g.
3. A dose resolution of 0.5 mGy and the ability to measure TID up to 120 Gy.
4. Resistance to SEUs and operational survivability for TID up to 200 Gy.
5. Power consumption not exceeding 300 mW.

Using these criteria, the final design achieved a mass of 42 g and a power budget of 127.62 mW, both with a 20% margin for safety and reliability [2]. This design is shown in Figure 2.14, with its interaction with the rover illustrated in Figure 2.16. The current rover design includes two rinted Circuit Board (PCB): the ”mainboard”, which houses the primary components and is located inside the rover, shielded by the chassis for protection, and the ”daughterboard”, an extension of the mainboard, mounted on the outside of the rover to interact directly with the lunar environment. As shown in Figure 2.15, this arrangement enables the sensors to detect a range of values, hopefully enhancing the mission’s scientific outcome.

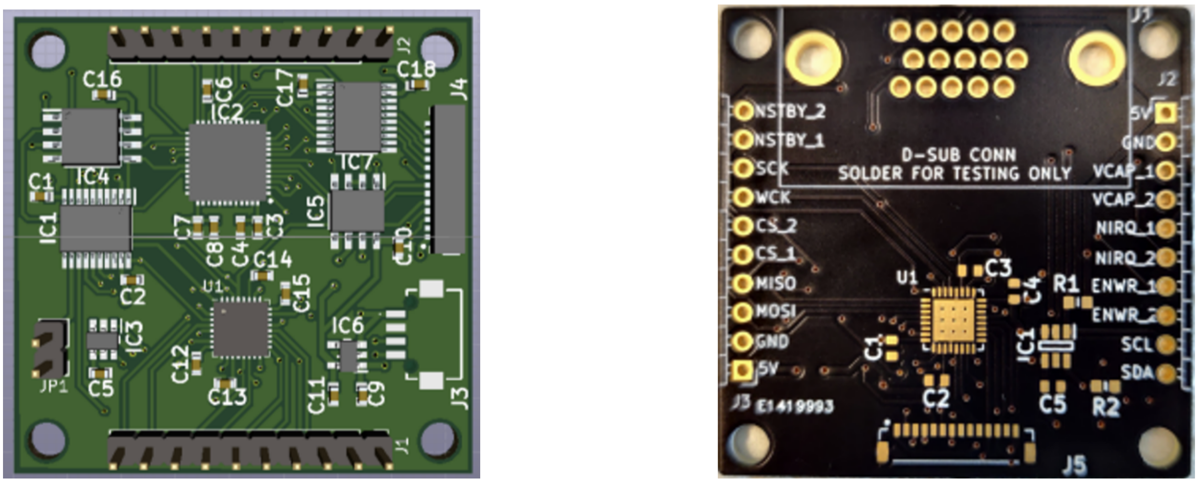

(a) Mainboard

(b) Daughterboard. U1 is the location of the FGDOS

Figure 2.14: Lunar Zebro radiation payload design [2]

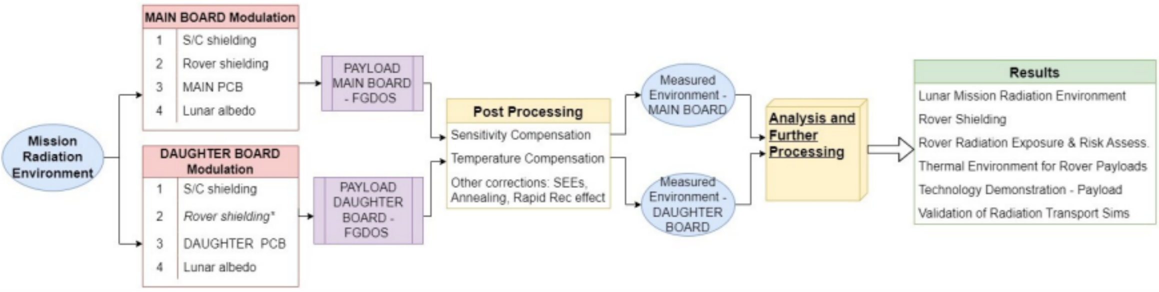

Figure 2.15: Science Scheme of the Radiation Payload [2]

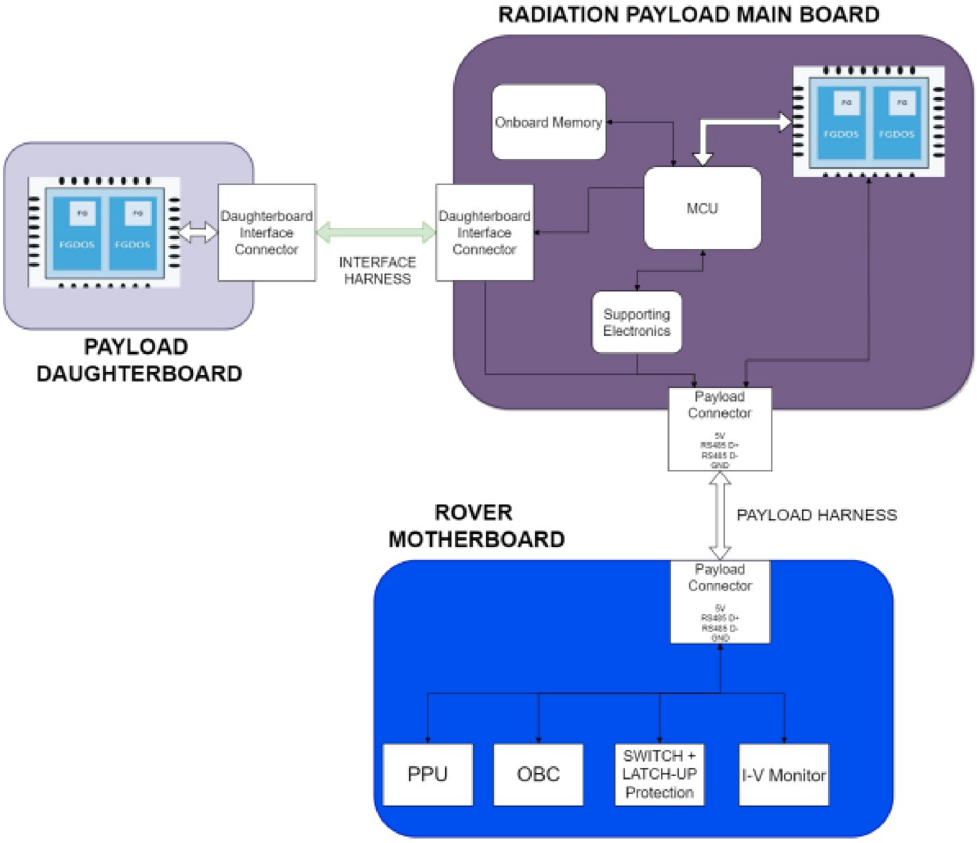

Figure 2.16: Lunar Zebro Radiation payload system architecture. The mainboard contains the components necessary to communicate with the Floating gate sensors and to the rover. The daughterboard acts as an extension to conduct measurement radiation without rover shielding [2].

2.5. Radiation monitoring with Floating gates Dosimeters

As mentioned in the previous section, the Floating Gate Dosimeter (FGD-03F) from Sealicon was selected as the radiation sensor for the Lunar Zebro radiation payload. In the following sections, the sensor will be explained in detail. Firstly, in subsection 2.5.1, a descriptive and quantitative model of the Floating Gate Sensor's response to radiation will be presented. Next, in subsection 2.5.2, the chip layout will be discussed. With this knowledge, the different operational modes of the FGD-03F will be examined in subsection 2.5.3. Finally, the sensor's sensitivity to radiation and temperature will be explored in subsection 2.5.4.

2.5.1. Floating gate sensor

The FGDOS is a radiation sensor based on a floating gate metal–oxide–semiconductor field–effect transistor (MOSFET) structure. A schematic representation of the FGDOS is show in Figure 2.17. The sensor is simple in its design, consistent with a floating gate (FG)[2] for storing charge, Si02[3] to electrically isolated the FG and Aluminium (Al) on top to protect the FG from external electrostatic field [57].

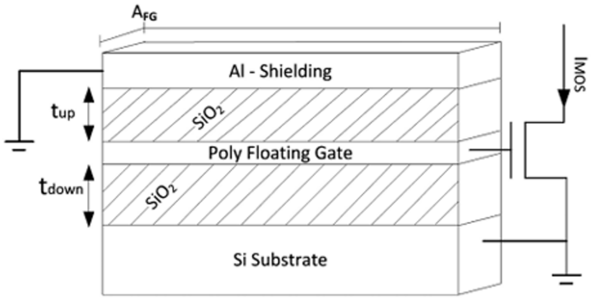

Figure 2.17: Schematic structure of FGDOS without the injector[58]

The charge can be introduced into the FG through several mechanisms, such as avalanche breakdown[4] or tunneling[5] from an auxiliary electrode[57]. Once the charge is stored, the FG can function as a memory cell, retaining its state without requiring continuous power[59]. Additionally, FG can be used for radiation monitoring by exploiting the generation of electron-hole pairs in surrounding oxides. Depending of the the polarity of the FG charge, one of these two types of carriers is attracted towards the FG gradually discharging it. This change in FG charge serves as an indicator of the radiation dose. The FG can thus act as a dosimeter, functioning at zero bias. However, a small bias voltage is needed to read the absorbed dose.

Descriptive and Quantitative Model

A detailed model describing the FG's behavior under radiation exposure can be formulated, but certain assumptions are required. The charge generated by radiation in the oxide can be expressed as[57, 58, 60]:

$$Q_{\text{gen}} = eE_{\text{dep}}W_{e-h}, \tag{2.3}$$

where e is the elementary charge, E_{dep} is the energy deposited by ionizing particles, and W_{eh} is the energy required to generate one electron-hole pair. The deposited energy E_{dep} can be written as:

---

[2] Usually made of Polysilicon, a silicon made up of many small crystals, making it a great electric conductor. Especially if it has been doped.

[3] A dielectric material, reference as oxide layer

[4] Avalanche breakdown occurs when a strong electric field in a semiconductor (and isolators) causes free electrons to gain enough energy to knock additional electrons loose from their atomic bonds. This creates a chain reaction, or "avalanche," of charge carriers, resulting in a sudden and significant increase in current through the materia

[5] Quantum mechanical phenomenon where particles pass through a potential barrier. This occurs because, at the quantum level, particles have a wave-like nature

$$E_{\text{dep}} = \rho_{\text{ox}} A t_{\text{ox}} D, \tag{2.4}$$

where ρ_{ox} is the oxide density, A is the area, t_{ox} is the oxide thickness, and D is the dose. Recombination of electron-hole pairs is the first significant process that follows charge generation. Two important recombination processes can be identified: (1) the probability that electron-hole pairs recombine immediately after generation (initial recombination), and (2) recombination that occurs as carriers travel to the gate and bulk, interacting with impurities or traps in the material.

Assuming (i) that the FG has a positive charge on it, (ii) that all electrons created by radiation and surviving initial recombination are successfully collected by the FG, and (iii) that no positive charges are trapped in the oxide or at the silicon interface, the collected charge, Q_{col}, will be proportional to the generated charge and can be approximated as:

$$Q_{\text{col}} = Q_{\text{gen}} \left(1 - R(\mathcal{E})\right), \tag{2.5}$$

Where R represents the recombination rate influenced by the electric field $\mathcal{E}$, which affects the proportion of charge carriers that avoid initial recombination [61]. Once the charge variation on the FG has been determined, the voltage variation (ΔV) as a function of the dose, can be calculated through the capacitor relationship:

$$\Delta V = \frac{Q_{\text{col}}}{C}, \tag{2.6}$$

where C, the capacitance of the capacitor, is expressed as:

$$C = \frac{\epsilon A}{t_{\text{ox}}}, \tag{2.7}$$

with ϵ being the permittivity of the dielectric ($\epsilon = \epsilon_r \cdot \epsilon_0$, where ϵ_r is the relative permittivity and ϵ_0 is the permittivity of free space).

By substituting and combining equations, the voltage variation as a function of the dose can be expressed as:

$$\Delta V = e\left(1 - R(\mathcal{E})\right) \frac{\rho_{\text{ox}} t_{\text{ox}}^2}{\epsilon W_{e-h}} D. \tag{2.8}$$

Looking at Equation 2.8, a proportional relationship between the dose and the voltage is expressed. However, this voltage variation depends on the dose but also on the charge yield, i.e. the amount of charge escaping the initial recombination, which is influenced by the electric field. Different particles give rise to different fractions of carriers surviving the initial recombination[14], as can be seen in Figure 2.18

Considering that the electric field in the insulator can be expressed as the ratio between the voltage across the capacitor and the oxide thickness, it can be expressed as:

$$\mathcal{E} = \frac{V_{\text{cap}}}{t_{\text{ox}}} = \frac{V_{\text{init}} - \Delta V}{t_{\text{ox}}}. \tag{2.9}$$

Hole Trapping and long term trapping

However, the above physics model does not take into account that the charge collection mechanism is unaffected by hole trapping in the silicon dioxide. As a first approximation, this assumption is reasonable, as the amount of trapped charge is negligible compared to the electrons collected at the FG. However, hole trapping is a cumulative effect that ultimately influences the sensitivity of the sensor[21]. Additionally, the model neglects the impact of different particle species and their associated energy on the creation of electron-hole pairs [57, 58]. For example, a 500 keV proton would interact differently in the material, producing a different number of electron-hole pairs than a 500 keV photon.

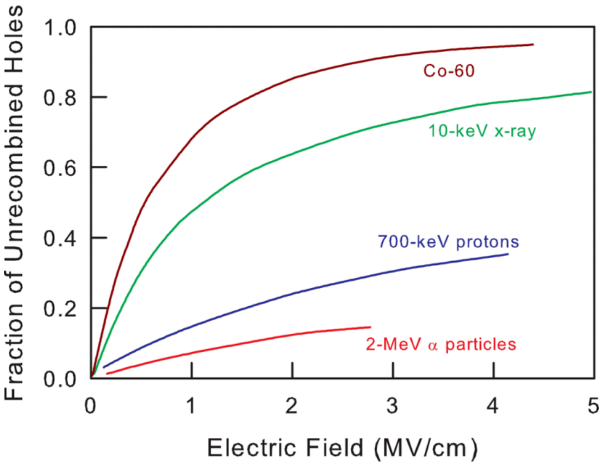

Figure 2.18: The fraction of holes that survive initial recombination as a function of the electric field for different ionizing species.[14]

Practical Measurement Techniques

The charge on the FG can be monitored by measuring the drain current of the transistor [62]. Alternatively, the FG potential can be compared to a reference transistor of identical size. In this method, both transistors are biased at the same drain-source potential and forced to conduct the same current, resulting in an equal gate potential[57, 63].

An important criterion for a dosimeter is that its reading should ideally be linearly proportional to the dosimetric quantity being measured [64]. The same principle applies here: a linear relationship between the absorbed dose and the output of the reading system is desirable. However, as shown in Equation 2.8, this behavior is not inherently linear, since the absorbed dose depends on the electric field, which itself varies with the voltage drop across the capacitor.

Additionally, the relationship between the drain current and the FG voltage remains linear only for small voltage variations. By constraining the capacitor discharge within a limited range, a linear response between the dose and the current of the reading transistor can be achieved. The implementation of this recharging process is illustrated in Figure 2.19.

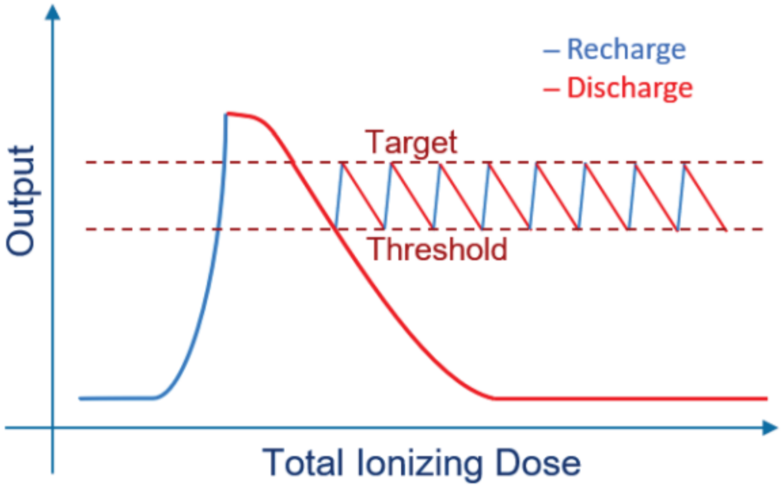

Figure 2.19: Linearization of the FGDOS sensor: The FG is charged to a specific value. When radiation interacts with the sensor, the FG begins to discharge. If it is not periodically recharged, the FG may exceed its linear operating range.[60]

2.5.2. Layout

For the Lunar Zebro radiation payload, The FGD-03F, seen in Figure 2.20, was used. This integrated circuit(IC) was designed for radiation detection with a resolution of 2500 µGy [65] and a maximum measurement capacity of 500 Gy[4]. It is housed in a compact QFN32 package (5.0 × 5.0 × 0.9 mm) and includes two independent sensors for redundancy. The sensor operates in two modes: low sensitivity (10 kHz/Gy) [4] and high sensitivity (70 kHz/Gy)[4]. It requires a 5 V supply voltage and includes an integrated temperature monitor with a resolution of 1 °C.

The sensor's internal components include a reference oscillator to counteract temperature effects (more in Appendix B), a charge pump for recharging post-irradiation, and internal counters for processing the frequency output. It uses SPI communication for interfacing with microcontrollers. In addition, it includes dedicated pins for power (analogue and digital), SPI signals (SCK, NCS, MOSI, and MISO), and (NSTBY) to reduce power consumption when not in use. Finally, an interrupt pin (NIRQ) indicates when new measurement data are available.

The sensor operates by converting the floating-gate current into a frequency signal, which is well-suited for transmission over PCBs or coaxial cables. An FSM manages the operational modes, with settings and registers accessible via SPI. Configurable parameters include the threshold and target values for recharging, manual control options for recharging and discharging, sensitivity and operational modes, and more.

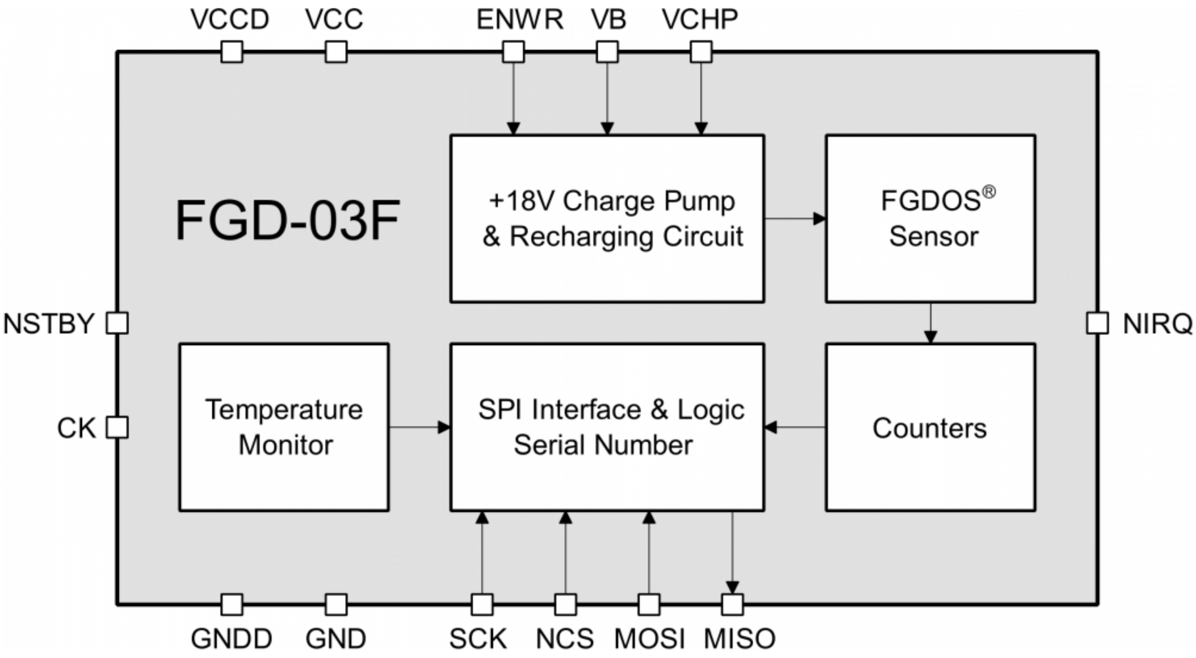

Figure 2.20: FGD-03F block diagram [65]

The drain current is converted into a frequency using a current-to-frequency converter, producing a square wave signal that varies with the absorbed radiation dose [57].

2.5.3. Operational Modes

The FGDOS device operates in three primary modes: *Active mode*, *Passive mode*, and *Autonomous mode*. These modes are designed to provide a versatile system for radiation dose monitoring.

Active Mode

In *Active mode*, the sensor relies on an external circuit for both readout and recharge. This setup can utilize components such as an FPGA[6] and an external power supply. During this mode, the sensor's frequency variation is continuously monitored throughout irradiation, enabling real-time data acquisition. Active mode is essential for live monitoring and data recording during experiments or operational activities.

Passive Mode

The *Passive mode* enables dose monitoring without requiring external biasing or wiring of the sensor. The dose is determined by comparing the output frequency before and after irradiation. This frequency variation can be converted into a dose using one of two approaches:

- Using the sensor sensitivity as a calibration factor.
- Exploiting the characterization curve as a calibration reference.

A limitation of the Passive mode is its restricted dose range, which is constrained by the single discharge of the FG capacitor.

Autonomous Mode

To address the limitations of Passive mode, the *Autonomous mode* extends the dose range to the entire lifetime of the sensor. This is achieved by integrating a recharging circuit within the FGDOS and enhancing the communication controller. Measurements in this mode involve periodic access to the sensor registers via a digital interface, allowing data readout and sensor configuration through a microcontroller(MCU).

In Autonomous mode, the sensor itself manages the recharge process. The absorbed dose is determined by monitoring the number of recharges and the output frequency at specific reading times. This makes the mode particularly effective for long-term and self-sustained monitoring applications.

Dose Determination in Active and Passive Modes

For both Active and Passive modes, the absorbed dose D can be calculated using the following equation [4]:

$$D = \frac{f_{\text{sens}}(t_2) - f_{\text{sens}}(t_1)}{S_r}, \tag{2.10}$$

where:

- $f_{\text{sens}}(t_1)$ and $f_{\text{sens}}(t_2)$ are the sensor frequencies at times t_1 and t_2, respectively.
- S_r represents the irradiation sensitivity of the sensor.

---

[6] A type of configurable integrated circuit that can be repeatedly programmed after manufacturing

2.5.4. Radiation and Temperature Sensitivity

A significant challenge in using the FGDOS sensor lies in the strong dependence of its drain current on temperature [57]. To mitigate this issue, the dosimeter system combines the FG sensor with signal conditioning electronics and a current-to-frequency converter. This setup allows sensitivity measurements in terms of Hz/Gy[7], rather than the conventional V/Gy, offering a distinct advantage [57].

In this section, we will first examine the minimum detectable dose rate, followed by an analysis of sensor degradation as a function of TID. Next, we will discuss the impact of temperature fluctuations, and finally, we will conclude with a review of relevant findings from the literature.

Relating FG Potential to Radiation-Generated Current

The voltage variation from Equation 2.8, caused by radiation, generates a current (I_r) that is directly linked to the FG potential (V_{FG}). This relationship can be expressed as [57]:

$$I_r = -C\frac{dV_{\text{FG}}}{dt}, \tag{2.11}$$

where C is the capacitance of the FG capacitor, and dV_{FG} is the voltage variation due to radiation exposure. By expanding this equation with the detailed expression for dV_{FG}, the current can be written as:

$$I_r = -C\cdot e(1-R(\epsilon))\rho_{\text{ox}}t_{\text{ox}}^2\frac{\mathcal{E}}{W_{e-h}}D. \tag{2.12}$$

Detection Limits

In authors of [57], using experimental data collected on the FG sensor, they could approximate the voltage (V_{FG}) as:

$$V_{\text{FG}} = V_r\left[\left(1+\frac{V_{\text{init}}}{V_r}\right)\exp\left(-\frac{D}{D_r}\right)-1\right], \tag{2.13}$$

where:

- V_r is the product of $\mathcal{E}_r$, a constant dependent on the type of ionizing particle, and the thickness of the oxide,
- V_{init} is the initial FG voltage before irradiation,
- D_r is a constant given by:

$$D_r = \frac{W_{e-h}C\mathcal{E}_r}{eA\rho_{\text{ox}}f_0}. \tag{2.14}$$

Then the sensor's sensitivity at zero dose ($D = 0$) can be defined as[57]:

$$S_{D=0} = \left.\frac{dV_{\text{FG}}}{dD}\right|_{D=0} = -\frac{V_r+V_0}{D_r}. \tag{2.15}$$

The minimum detectable dose (dD_{min}) is determined by the equivalent voltage noise (v_n) over the FG capacitor and the maximum sensitivity[57]:

$$\Delta D_{\text{min}} = \frac{v_n}{S_{D0}}. \tag{2.16}$$

From Equation 2.13, it appears that the decay in sensitivity follows an exponential trend as a function of the received dose. However, [3] observed that the sensitivity degrades linearly with the TID, with a noticeable bending point at 80 Gy, see Figure 2.21. These tests were conducted in a Co-60 facility at a dose rate of 3.06 Gy/h.

---

[7] A common dose unit seen in the literature is the ”rad”, where 1 rad = 0.01 Gy. But this thesis stays with Grays.

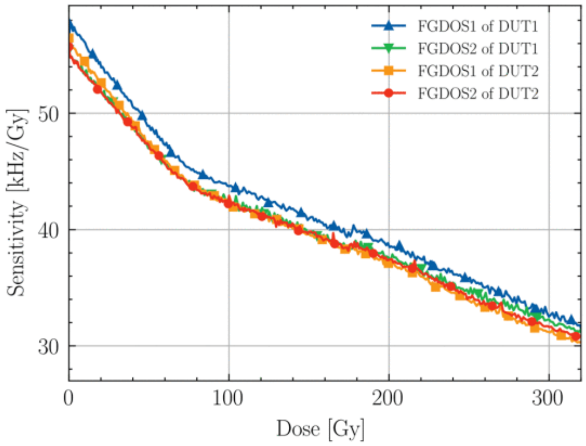

Figure 2.21: The FGDOS sensitivity degrades as a function of the TID while operating in passive mode.[3]

Temperature compensation

As discussed previously, the output signal of the FGDOS is influenced by temperature fluctuations and requires compensation. To achieve this, an identical NMOS transistor [60] is compared to the FG capacitor, is biased in similar conditions, and is integrated into the sensor. Using this, the generated signal will follow the same temperature fluctuations as the signal generated by the radiation-sensitive circuit but is immune to the ionizing dose.

Brucoli et al. [60] reported that the reference frequency is dose-independent, with a variation of less than 1% over a cumulative dose of 230 Gy. However, they highlighted a disagreement between the reference's response to temperature variations and the output frequency. This behaviour was characterized and is illustrated in Figure 2.22. In their setup, the FG was charged to different output frequencies within the linear range of the sensor, while maintaining a constant temperature of 20°C. Additionally, the twin transistor was fixed to a value corresponding to a reference frequency of 55 kHz at 20°C.

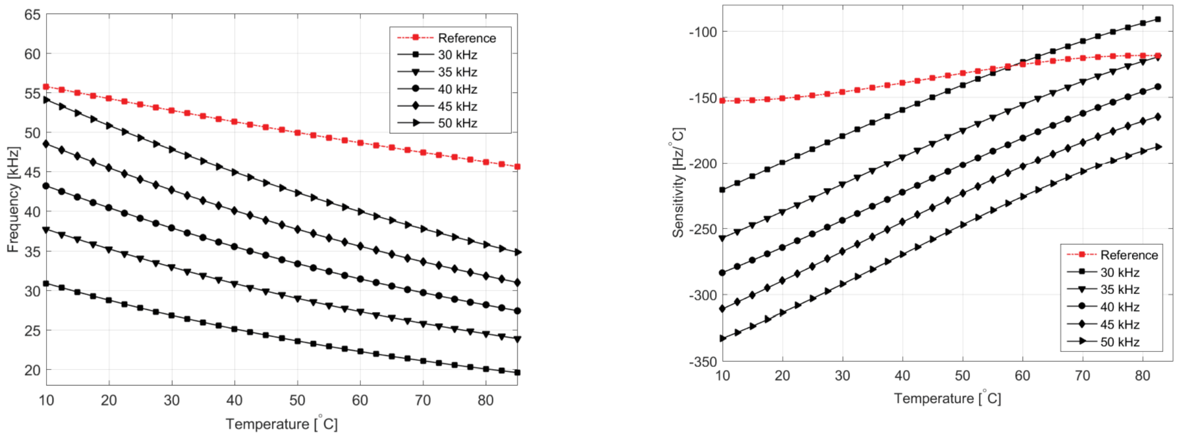

(a) Frequency as a function of temperature

(b) FGDOS temperature Sensitivity as a function of temperature for different working points

Figure 2.22: The frequency variation of floating-gate transistors for different amounts of charge stored in the floating gate (black) and the twin MOSFET (red) is shown as a function of temperature. The reported frequency values fall within the linear range of the sensor described in [60], which differs from the linear dynamic range of the FGDOS sensor characterised in this thesis.

If the assumption can be made that the relationship between the FG output signal and the reference signal is linear, the sensor's accuracy can be significantly improved [4]. To achieve this, the user should monitor the behavior of both outputs during temperature variations after the initial recharge. This process allows for determining a linear slope, which can then be used to compensate the FG output signal using the following equation:

$$f_{\text{sens, compensated}} = (f_{\text{ref, 0}} - f_{\text{ref}}) \cdot \text{slope} + f_{\text{sens}} \tag{2.17}$$

where $f_{\text{sens, compensated}}$ is the compensated sensor signal in Hz, $F_{\text{ref, 0}}$ is the reference signal at the beginning of the measurement (used as an offset for comparison), f_{ref} is the reference signal in Hz, f_{sens} is the uncompensated sensor signal in Hz.

Using this method, voltage variations and temperature-induced effects are removed from the sensor output, isolating its response to radiation alone.

Note Regarding MOSFET Damage

Typically, MOS technologies are only primarily sensitive to TID effects rather than DD, as ionizing radiation leads to charge buildup in the gate oxide, resulting in threshold voltage shifts, increased leakage currents, and degradation in device performance [25, 29].

2.5.5. Literature review on Floating gate dosimeter

Over the years, various research groups have investigated the floating-gate dosimeter for different applications. While multiple studies have provided valuable insights, discrepancies in the results have also been observed. Below is a brief overview of some of the most significant research and findings.

Publications

- in 2012, Garcia-Moreno et al. [57]: Initial design of the Floating gate dosimeter using a frequency as output was proposed. This was not the first time the concept of the floating gate as a radiation was proposed.
- in 2013, Garcia-Moreno et al. [66], developed an improved version of the 2012 version with experimental results shown.
- in 2013, Álvarez et al. [67], An initial characterization of the floating gate sensor, designed by iC-Málaga and currently named Sealicon, was conducted to evaluate its suitability for space missions. The results indicated that the sensor remains adequate for space applications up to at least 100 Gy(Si). Additionally, the study reported a sensitivity in high-sensitivity mode ranging from 26.5 to 30.0 kHz/Gy. It was also noted that the chip was fabricated using 0.8 µm commercial technology with an oxide thickness of 0.25 nm.
- in 2014, Cesari et al. [68], characterised the recharging cycles of a floating gate PMOS radiation sensor. Compared to the 2012 version, which was based on an N-MOS design, the PMOS variant exhibits lower 1/f noise than N-MOS devices, potentially increasing the sensor's lowest detectable dose.
- in 2014, Danzeca et al. [58], a prototype of the FGDOS has been characterized with a Co60 source and with protons. The dependency of the sensor sensitivity on the dose rate and accumulated Total Ionizing Dose (TID) are investigated. An analytical model of the sensor is presented in the paper and the theoretical sensitivity for the prototype of FGDOS is evaluated.
- in 2015, Cesari et al. [69] presented the results of two floating gate dosimeters by iC-Málaga, currently named Sealicon, onboard the 4M lunar flyby. They did temperature characterization before the mission from -20 to +50 °C, resulting in a look-up table. Using gamma irradiation, they had shown that the high sensitivity mode was equal to gamma radiated: 38.5 kHz/Gy. This article shows mostly that the concept of floating gates in space works, but the results have large uncertain caused by mission deadlines.
- in 2016, Brucoli et al. [70] did a comprehensive study and characterization of Floating Gate Dosimeter for the CERN environment.
- in 2017, Cesari et al. [71] This work aims to enhance FGDOS performance by improving noise and sensitivity, validating predictive models, and incorporating radiation-hardening techniques for better endurance and accuracy.
- in 2017, Brucoli et al. [72]: the suitability of a floating gate dosimeter as a total ionizing dose (TID) detector in mixed fields has been investigated. The FGDOS demonstrated high sensitivity, resolution, and linearity, with a maximum radiation response spread of 2.9% among sensors in the same batch and an error margin under 10% for TID measurements. It outperformed RadFETs in resolution, requiring significantly less time for dose stabilization, and achieved excellent linearity using the auto-recharge system. Temperature sensitivity characterization provided a method for correcting temperature effects, and the resolution achieved was 16 mrad(Si), much higher than the 6 rad(Si) of RadFETs.
- in 2021, Brucoli et al. [73] explores a technique to measure the charge yield using the floating gate measurement.
- in 2022, Rizzo et al. [74] investigate a new method for enhancing the sensitivity of the Floating Gate Dosimeter. By increasing the electric field in the silicon dioxide, by installing an external field over the sensor. Showed a sensitivity degradation improvement of up to 40% and sensitivity enhancements of up to 60%.

Master students

- in 2022, De Meyere et al. [1], integrated the Sealicon sensor chip with a Cube Sat testbed, enabling real-time radiation data collection. Proton beam tests confirmed detection but revealed lower-than-expected sensitivity and degradation with total ionizing dose. High electrical noise was identified, requiring filtering and further research to improve performance, especially at lower particle energies.
- in 2022, Shanbhag et al. [2] i) Radiation Payload design & development for the Lunar Zebro, (ii) Modelling and analysis of the radiation environment in the context of the science mission of Lunar Zebro and (iii) Extended characterisation and testing of the FGDOS for its application as the core detector of the Radiation Payload.
    - *Combined radiation and Temperature Stress Testing:* The payload was subjected to extreme temperature ranges (-15°C to 93°C) while exposed to 120 MeV protons at dose rates of 0.001 to 0.6 Gy/min. These tests aimed to simulate the combined thermal and radiation conditions of the lunar environment. The Results and Observations showed that:
        - The effect of radiation on sensor frequency was successfully decoupled from temperature-induced effects with high accuracy under moderate temperature gradients and monotonic variations.
        - For stronger temperature gradients and non-uniform thermal profiles, the decoupling process exhibited reduced accuracy, particularly when uniform heating across the FGDOS chip was not maintained.
- in 2023, Dijks et al. [75] focused on CERN’s Space RadMon-NG, a CubeSat payload designed to improve space radiation monitoring with a Floating Gate Dosimeter for Total Ionizing Dose and an SRAM sensor for high-energy hadron fluence. System-level tests at CERN’s CHARM facility and temperature characterization at a Cobalt-60 facility verified its performance, with deviations within 2.5% when proper compensation was applied. The payload demonstrated significant advancements over traditional sensors, offering better resolution, lower costs, and reliable performance in mixed-field environments. Challenges included communication issues and condensation during testing.

Reviews,

- Garcia-Inza, Carbonetto, and Faigon [76]: reviewing the main aspects of MOS dosimetry, as the devices have been used for the last 50 years.
- Gerardin and Paccagnella [77]: comprehensive discussion of total dose and single event effects result in a wide cross-section of non-volatile memories, including FG devices.

3

Low-Flux Gamma Irradiation Measurements

This chapter focuses on the gamma experiment conducted at RID. section 3.1 provides an overview of the facility, leading into section 3.2, which explains the setup, uncertainties, and procedures. This is followed by section 3.3, which presents and discusses the experimental results. Finally, section 3.4 concluded on the findings.

3.1. The facility: RID Calibration lab

In the basement of the Reactor Institute Delft (RID), there is a facility primarily used for the calibration of measurement devices, as shown in Figure 3.1. To achieve this, the facility contains seven radiation sources: four Cobalt-60 (Co-60) and three Cs-137 sources with different activities.

Since the intensity of the source follows the inverse-square law, different flux levels can be obtained by placing the measurement device at varying distances from the source. The bench on which the setup is mounted can be adjusted to positions ranging from 0.8 m to 5.5 m from the source. The sources, their activities, and the dose rate at a distance of 0.8 m are listed in Table 3.1.

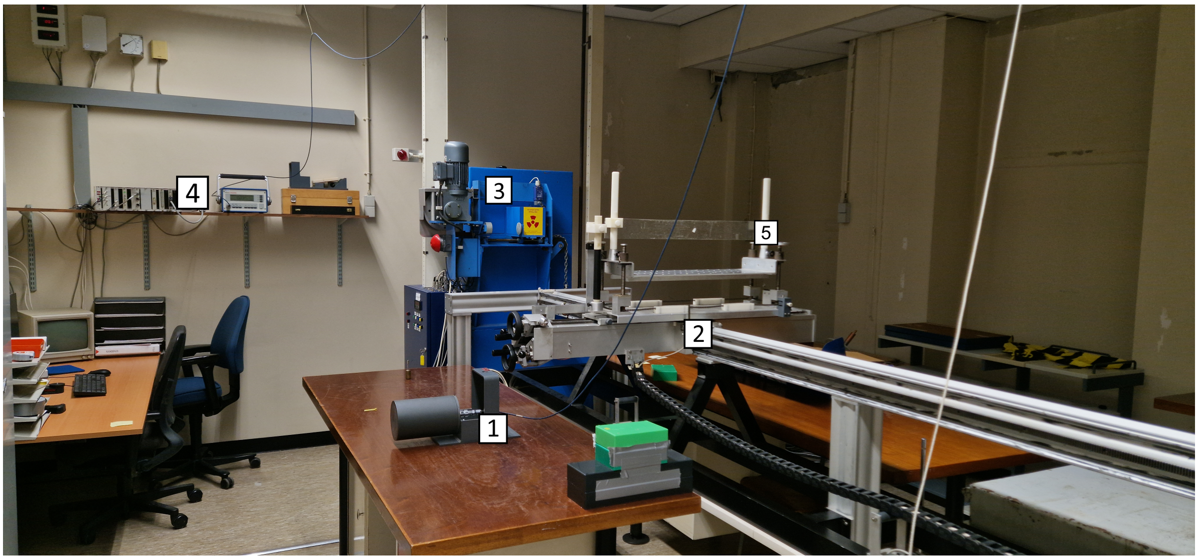

Figure 3.1: RID calibration lab. 1) PTW-Freiburg M2337 1000 CC -Ionisation Chamber. 2) Movable bench. 3) lead-shielded housing for radioactive sources. 4) PTW UNIDOS - Dosimetry monitor. 5) Custom setup, used for aligning and precise distance measurements.

Table 3.1: Reactor Institute Delft (RID) calibration lab. The source is contained within the blue lead container, as shown in Figure 3.1.

Container number	RID internal reference number	Type	Dose rate on 18 nov 2024, at 0.8 m from source. [uGy/h]	Activity source, 27 mei 2021 [MBq]
1	4270	Co-60	$2.12 \cdot 10^{0}$	$6.10 \cdot 10^{0}$
2	3259	Co-60	$8.60 \cdot 10^{0}$	$2.49 \cdot 10^{1}$
3	4271	Co-60	$7.02 \cdot 10^{2}$	$2.00 \cdot 10^{3}$
4	8290	Co-60	$7.45 \cdot 10^{3}$	$2.27 \cdot 10^{5}$
7	3264	Cs-137	$1.73 \cdot 10^{5}$	$1.37 \cdot 10^{6}$
8	3262	Cs-137	$1.79 \cdot 10^{2}$	$1.50 \cdot 10^{3}$
9	3263	Cs-137	$1.92 \cdot 10^{3}$	$1.53 \cdot 10^{5}$

Radiation production

The sources mentioned above both create gamma radiation. In Figure 3.2, the decay of Co-60 and Cs-137 are displayed. Both are widely utilized sources of gamma radiation, however, Co-60 has been the standard for simulation of ionization effects in silicon components in the past, but in recent years Cs-137 has gained increased acceptance, owning to 30 years half-life and less severe shielding requirements [64]. In addition, depending on the way the source is encapsulated, beta radiation can reach the measurement device. However, at this facility, the sources are in an RVS capsule, which blocks beta radiation, ensuring that only gamma radiation contributes to the radiation field.

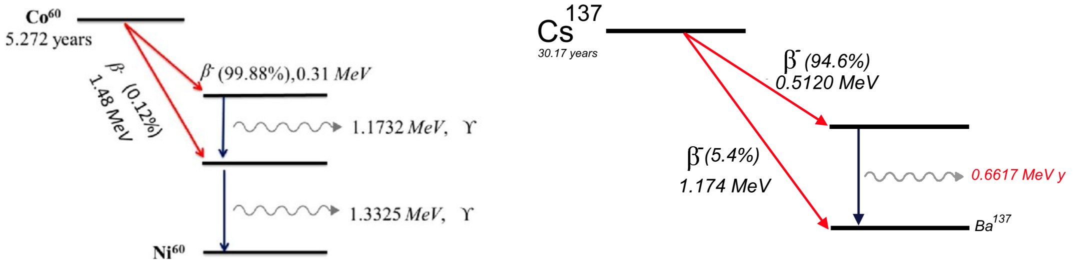

(a) Co-60 decay scheme [78]

(b) Cs-137 decay scheme. Info from [79, 80]

Figure 3.2: Decay scheme of Co-60 and Cs-137.

3.2. Methodology

There are a couple of standardized test procedures as mentioned by Ravotti et al. [64] for irradiation of electronic devices. This includes, for example, ESCC 22900 Iss.5 (2016) [81] and MIL-STD-883 TM 1019.9. To enable precise and accurate dosimetry measurement, the device under target (DUT) must ideally be characterized in terms of radiation energy, spectrum, and dose rate, to allow for reliable predictions for radiation hardness assurance and behaviour[64].

In this experiment, only Co-60 will be used, and thus the energy spectrum can be neglected. It is then only important to characterize the dose rate before placing the FGDOS in the beam. To do this, a calibrated 1000 CC ionization chamber is used. This requires temperature and pressure correction, to account for the change in the mass of air in the chamber caused by atmospheric variations [82]. The effect of humidity, on the other hand, is generally ignored with the provision that the relative humidity is within certain limits (typically 20% to 80%). Using the protocol from IAEA [83], the correction factor k_{TP} can be calculated using:

$$k_{TP} = \frac{(273.2 + T)}{(273.2 + T_0)} \frac{P_0}{P}, \tag{3.1}$$

where P and T represent the cavity air pressure and temperature at the time of measurements, and P_0 and T_0 are the reference values, typically 101.3 kPa and 20 °C, respectively.

3.2.1. Uncertainty

The accuracy of dosimetry measurements refers to how close their expected value is to the ”True” value of the measured quantity. Uncertainties in these measurements can be divided into two categories: Statistical (type A) and Systematic (type B). Statistical uncertainty u_A is obtained through the statistical analysis of repeated measurements, and reduced by increasing the number of measurements N.

$$u_A = \frac{\sigma}{\sqrt{N}}, \tag{3.2}$$

With σ being the standard deviation.

Systematic uncertainty is intelligent guesses or scientific judgments of non-statistical uncertainties. This includes environmental processes (e.g. temperature, pressure, humidity, etc.), calibration, etc.[64].

For the measurement of the sensitivity of theFGDOS at low dose rates, a series of uncertainties (see Table 3.2) must be considered. By identifying and optimizing each source of uncertainty, the overall measurement uncertainty can be reduced, bringing the result closer to the ”true” value.

Explanation	Symbol	How to minimize it?
Dose Rate Uncertainty		
Uncertainty and measuring error of the dose rate	σ_{read}	By allowing the ionization chamber to stabilize, the average value and standard deviation can be measured accurately.
Uncertainty in temperature	σ_T	Greisinger GFTB 200: read value after stabilization relative error: $\pm$0.5% of measured temperature absolute error: $\pm$ 0.1 °C[84]
Uncertainty in pressure	σ_P	Greisinger GFTB 200: read value after stabilization relative error: $\pm$1.5 mbar[84]
Uncertainty in distance from source	σ_r	By aligning the setup at the center of the bench, replication errors can be significantly reduced. However, due to potential drift in the alignment system and placement variations, an alignment error of approximately 0.2 m is assumed.
Uncertainty in device calibration	σ_{kal}	The device is calibrated annually at VSL, with reported values having a 3% uncertainty.
Device-Specific Uncertainty - FGDOS		
Variation in sensitivity as a function of charge on the floating gate (FG)	$\sigma_{Q,FG}$	*In LDR*: Sensitivity is considered constant. *Outside LDR*: If the change in sensor output is small, sensitivity is also considered constant.
Variation in temperature	$\sigma_{T,FG}$	As long as the temperature remains within a few degrees, temperature compensation can be applied with minimal additional error.
Variation in radiation source	$\sigma_{D,FG}$	Both sources have very long decay times. Over a $\pm$48-hour measurement period, the activity of cobalt-60 decreases by $\pm$0.0072%.
Variation caused by voltage	$\sigma_{V,FG}$	Delta Elektronika EST 150 - Triple DC power supply: In constant voltage (CV) mode, stability is 10^{-5}[85].

Table 3.2: An overview of uncertainties in sensitivity measurement and their minimisation

The sensitivity of the FGDOS is calculated using Equation 2.10. Assuming that both measured quantities have associated uncertainties and that there is no correlation between them, the uncertainty in sensitivity can be determined using the following equation:

$$\sigma_S = S\sqrt{(\frac{\sigma_R}{R})^2 + (\frac{\sigma_D}{\dot{D}})^2}, \tag{3.3}$$

where R represents the sensor response, with a linear fit applied to determine the average response and its associated uncertainty σ_R. The term $\dot{D}$ denotes the dose rate with associated uncertainty σ_D.

3.2.2. Setup

To characterise the behavior of the FGDOS under low dose rates, the daughterboard[1], as shown in Figure 2.14b, was used. The design allows for interfacing with the FGD-03F using minimal wiring and without unnecessary components compared to a breadboard setup, reducing complexity.

Using a custom-made cable, the daughterboard connects to an Arduino via the D-sub P15 interface. A schematic representation of this setup is shown in Figure A.1.

Further details on the engineering and operation of the setup are provided in Appendix A, while the sensor history and temperature compensation method are discussed in Appendix B.

3.2.3. Test plan

The objective of this experiment is to assess the feasibility of accurately detecting radiation on the lunar surface. As discussed in section 2.3, the LND measured a dose rate of 13.1 µGy/h during a solar minimum. This value serves as the order of magnitude required for radiation measurements on the lunar surface.

To achieve this, the experiment was conducted over four weekends. Table 3.3 provides an overview of the irradiation campaign, including any anomalies observed during each week.

Table 3.3: Overview of the low dose rate campaign

Date	Test purpose	Duration (s)	Dose rate (mGy/h)	Anomalies
6/09/24 - 10/09/24	**Trial run**, low irradiation test	235674 ± 15	6.2 ± 2.0	**Ionization chamber:** Too close to source, no homogeneity **Spyder unresponsive:** CSV files too large
15/11/24 - 18/11/24	**Run 1:** Aim: ± 0.6 mGy/h	236353 ± 15	1.78 ± 0.05	**Windows Update:** Caused a short timeout
22/11/24 - 25/11/24	**Run 2:** Aim: ± 0.06 mGy/h	230849 ± 15	0.250 ± 0.002	**Short circuit ->** sensor recharged beyond linear range -> not possible to discharge back
29/11/24 - 03/12/24	**Run 3:** Aim: ± 0.006 mGy/h	325519 ± 15	0.0013 ± 0.0003	Still outside linear range
03/12/24 - 04/12/24	**Run 4:** comparison with run 1, to obtain comparison between the two operation ranges	88109 ± 15	1.795 ± 0.02	Still outside linear range

During the experiment, several lessons were learned that are important to highlight.

Trial Run Issues

Firstly, during the trial run, an issue was encountered where Spyder [2] stopped responding after logging and printing data to the serial monitor, despite the data still appearing to be logged. The issue was resolved by creating a new CSV file every 6 hours.

Another issue involved the 1000 CC ionization chamber, which was placed at ±0.85 meters from the source. However, one of the key requirements for using an ionization chamber is that it must be placed in a uniform radiation field. When positioned too close to the source, the source can no longer be considered a point source, and scattering effects become more significant. A practical rule of thumb is to position the detector at least five times the detector's largest dimension from the source.

This explains the uncertainty observed in the dose rate measurements, with atmospheric corrections taken into account. On Friday, the 6th of September, a dose rate of 6.8 ± 0.1 mGy/h was measured,

---

[1] FGD-03F z1.1 192301

[2] Spyder is an open-source Python IDE included in the Anaconda distribution.

while on Monday, the 9th of September, a dose rate of 5.6 ± 0.1 mGy/h was recorded. Based on internal RID tables, the estimated dose rate was determined to be approximately 7.600 mGy/h. However, this value should be considered indicative only, as further verification may be required.

To ensure more accurate measurements in future experiments, the ionization chamber should be placed further from the source. However, if measurements closer to the source are necessary, a smaller ionization chamber should be used instead.

Sensor Malfunction

A major issue occurred on 22nd November during a baseline test of the setup to validate its functionality. It was observed that the second sensor was not being detected. After checking the cabling and power cycling of the system, it was found that a probable short circuit had caused the sensor to recharge to approximately 240 kHz.

Efforts to discharge the floating gate (FG) using both internal[3] and external[4] discharge methods were unsuccessful, as the frequency stagnated at 206 kHz.

As seen in Equation 2.5 and Equation 2.9, the additional charge on the FG increases the electric field in the oxide, which in turn reduces the initial recombination rate and increases the number of charge carriers reaching the FG. However, the situation is more complex.

As shown in Figure C.3b, an increase in charge on the floating gate leads to a decrease in the sensor's sensitivity. By rerunning the first experiment and applying the temperature correction method (outlined in Appendix B), a comparison can be made between runs inside and outside the linear range, allowing for correction of this offset.

Additionally, the other sensor on the IC exhibited the opposite effect: when attempting to discharge it from $\sim$150 kHz, it instead charged up to 206 kHz and then appeared to stabilize at that frequency. This highlights the need for a clearer characterization of the recharging and discharging mechanisms of the sensor in future experiments.

Finally, the timeout during Run 1 was due to a Windows update.

3.3. Results and Discussion

In Figure 3.3, the results of the low-dose-rate gamma irradiation for the second sensor are displayed. The results for the first sensor are provided in the appendix (see Figure F.1).

The top plot in Figure 3.3 presents the raw data, where a proportional correlation between the dose rate and the accumulated charge on the FG can be observed. However, as the dose rate decreases, temperature fluctuations become more dominant, making it visually appear as though the sensor is malfunctioning or measuring incorrect values. The effects of low-dose radiation only become noticeable over extended periods, but the precise extent of the decrease remains uncertain. This highlights the necessity of temperature correction for low-dose-rate measurements, as outlined in Appendix B.

The bottom plot in Figure 3.3 displays the results after temperature compensation, where a linear fit has been applied to the data to determine the slope of the measurement. Two key observations can be made:

Firstly, values inside and outside the sensor's Linear Dynamic Range (LDR) exhibit approximately the same behavior (Run 2 vs. Run 4). From the HollandPTC test (see Figure C.3b), it was established that operating outside the linear range leads to a decrease in sensitivity. To compensate for this effect, the following correction factor is applied:

$$k_{NLR} = 1 + \frac{Sensor\ response(outside\ LDR) - Sensor\ response(inside\ LDR)}{\Delta dose\ rate}, \tag{3.4}$$

where $k_N LR$ is the non-linear correction factor, resulting in values of 0.99 and 1.104 for Sensor 1 and Sensor 2, respectively. The assumption is made that the decrease in FG charge is sufficiently small,

---

[3] By setting SET(2:0) in the register map to 16.5 V.

[4] By applying 20 V to the VCAP pin.

allowing the sensitivity in the non-linear range to be considered constant.
Secondly, the values at 250µGy/h and 1.28 µGy/h indicate that obtaining dose rates of this order requires an extended measurement period to draw concrete conclusions about the dose rate.

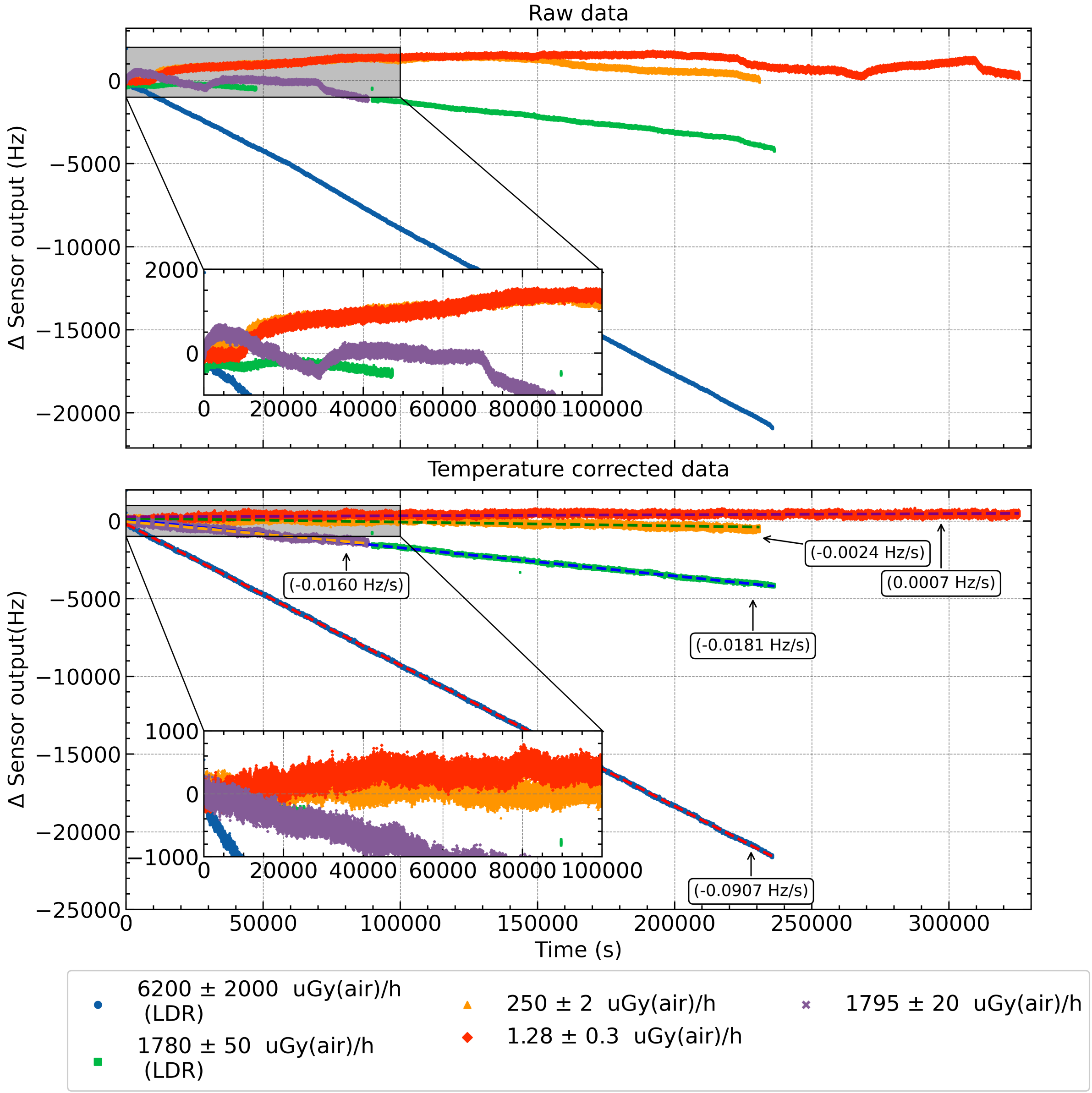

Figure 3.3: Low dose rate gamma measurement on the FGDOS. On the top, is the raw data. While on the bottom, temperature correction. For temperature correction values were 2.136 and 3.844 for inside and outside linear dynamic range (LDR) respectively. The internal temperature sensor registered a fluctuation of $\sim 3°C$

Comparison of Gamma and Proton Sensitivity

In Figure 3.4, the sensor response is plotted as a function of dose rate for both Co-60 gamma rays and 120 MeV protons, allowing a direct comparison between the two radiation sources. Since personal tests with protons have not been conducted using this specific sensor, the 120 MeV proton data is taken from Shanbhag et al. [2, see p.120], which includes data from Run 1.2 and Runs 1.4 to 1.6.

A linear fit was applied to both datasets to examine potential correlations between dose rates. Some dosimetry systems exhibit variations in response due to factors such as temperature, dose rate, angular dependence, and energy (e.g., silicon diode dosimetry systems [64]). The intercept was set at (0,0), as no sensor response should be observed in the absence of radiation.

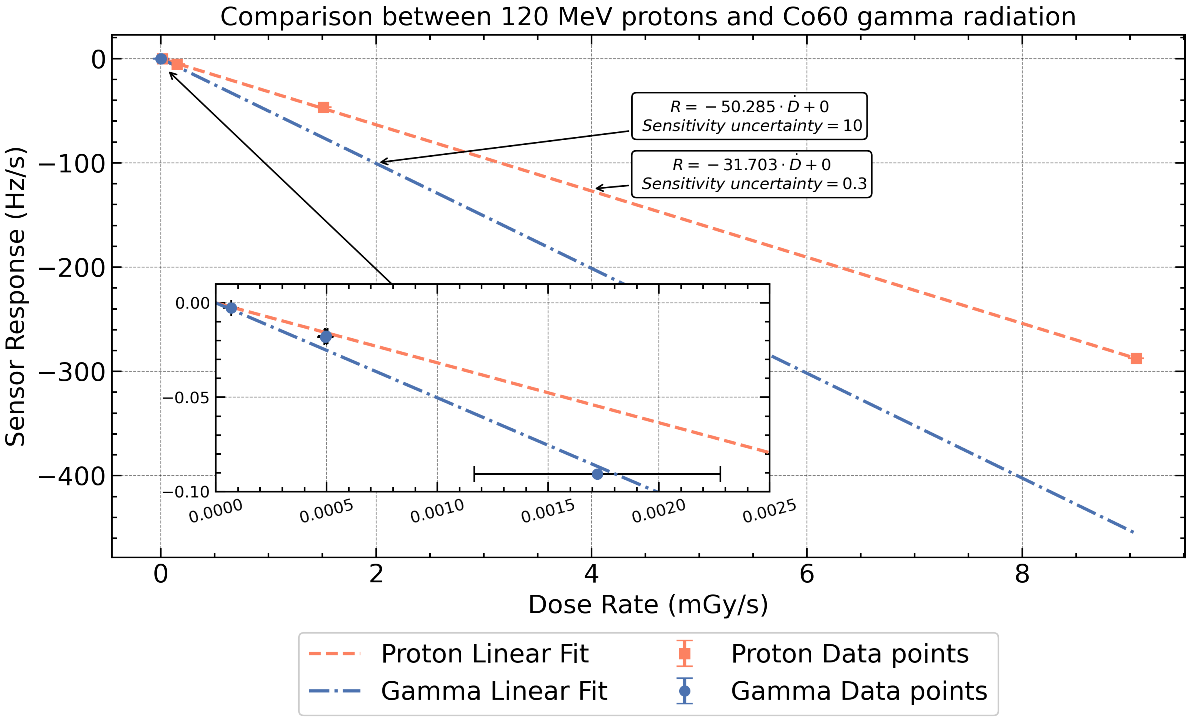

Figure 3.4: The FGDOS response plotted against different dose rates, both 120 MeV protons and Co-60 gammas. The dose rates are plotted in Silicon.

The gamma measurement at 1.28 µGy/h was excluded because it exhibited a positive sensor response, which was caused by efficient long measuring.

From this analysis, a proton sensitivity of 31.7 ± 0.3 kHz/Gy is obtained, while the gamma sensitivity for this particular sensor is found to be 50.3 ± 10.0 kHz/Gy.

Further, it is observed that the proton linear fit approximates the data quite well, including portions of the gamma dataset. However, when examining the zoomed-in view, it becomes evident that the trial run deviates from the other values. This deviation introduces high uncertainty in gamma sensitivity, as the data point appears to be an outlier.

The divergence may stem from an inaccurate dose rate during the trial run. Alternatively, it could suggest that the relationship between dose rate and sensor response is non-linear. For instance, Danzeca et al. [58] reported a decrease in sensitivity as the dose rate increased.

Of the two possibilities, it is most likely that the trial run is the outlier. When excluding this value, the gamma sensitivity drops to 36 ± 2.0 kHz/Gy, bringing it closer to the proton sensitivity. Still, this remains interesting. Firstly, the measurements are ±60 Gy apart in TID, and from Figure 2.21 (as well as Danzeca et al. [58]), it is known that the sensor exhibits degradation as a function of TID, suggesting that it may have partially recovered from the initial proton irradiation.

However, secondly, it is well established that the interactions of protons and photons with SiO$_2$ are fundamentally different (in additions their energies are different). The energy deposited by a single charged particle is typically expressed by LET. In contrast to charged particles, the energy deposited by photons cannot be described by LET. Instead, photons may either be absorbed in a single interaction or undergo scattering [86].

Measurement time on the lunar surface

Based on the results discussed earlier, a problem has been identified related to the Lunar Zebro mission. To estimate the required measurement time on the lunar surface, it is assumed that a new measurement would yield results similar to the LND measurement and that the sensor's sensitivity to radiation is independent of the dose rate (a valid assumption based on Figure C.4). Consequently, the charge depletion on the FG scales linearly with the dose rate.

According to the sensor data sheet, the noise level is 75 Hz, and for reliable detection, a signal-to-noise ratio (SNR) of 5 is assumed. Extrapolation from the available data estimates the sensor's response to a 15 µGy/h gamma flux at 0.00013 ± 0.0002 Hz/s, corresponding to a sensitivity of $\sim$ 31,000 ± 5,000 Hz/Gy. This is in agreement with general sensitivity values reported by Shanbhag et al. [2] and Danzeca et al. [58] for the FGDOS.

The required measurement time can be determined using the equation:

$$t = \frac{\text{SNR} \cdot n_{\text{sens}}}{S \cdot \dot{D}}, \tag{3.5}$$

where t is the time required to detect the observation in seconds, n_{sens} is the noise level of the sensor in Hz, S is the sensitivity of the sensor to radiation in Hz/Gy, $\dot{D}$ is the dose rate in Gy/s.

Applying this equation, detecting a signal with confidence at this low dose rate would require over 31 days, making it impractical for laboratory measurements.

For a lunar mission, additional challenges arise due to fluctuating dose rates and temperatures. Furthermore, the Lunar Zebro mission is currently planned to last only 14 Earth days, limiting the feasibility of obtaining meaningful results if this represents the typical lunar dose rate environment. Given the mission's goal of measuring dose rate variations behind different topographical features, the expected measurement duration significantly constrains the ability to draw conclusive insights.

3.4. Conclusion

During this campaign, multiple low-flux gamma measurements were conducted to investigate the behavior of the FGDOS under conditions comparable to those reported on the lunar surface [16, 47]. The findings indicate that, with its current characteristics, conducting relevant measurements on the lunar surface could take several days. However, discrepancies remain.

One key issue lies in the reported noise levels. The Sealicon datasheet[4] specifies a sensor noise of 75 Hz, while Brucoli et al. [60] applied filtering and moving average that reduced noise to 5 Hz. In contrast, De Meyere et al. [87] measured a noise level of 110 Hz, which they managed to lower to 90 Hz using a moving average. These inconsistencies highlight the need for further characterisation and noise mitigation strategies.

Another discrepancy concerns sensitivity. The measured sensitivity in this study is $\sim$ 31 kHz/Gy, which aligns with previous reports [1, 2, 58, 70]. However, this value remains significantly lower than the 70 kHz/Gy reported in the Sealicon datasheet[4] and the 54 kHz/Gy measured by Zimmaro et al. [3]. If the sensitivity were 70 kHz/Gy, the measurement time would be reduced to approximately 14 days.

Assuming this analysis is correct and that SNR, sensitivity, and noise levels remain fixed, one possible approach to improving measurement speed would be to increase the size of the FG, allowing for greater collection of radiation-induced carriers and enhancing discharge. However, this modification introduces several challenges. A larger FG could increase noise levels, complicate the recharging process, and introduce design and fabrication constraints. Furthermore, such a change might compromise the current payload design, particularly regarding COTS components and size limitations. While increasing the FG size could theoretically improve sensitivity, these engineering trade-offs must be carefully considered in future iterations.

In addition, future work should include further measurements with a Co-60 source, particularly at higher fluxes, such as those available at ESA ESTEC's Co-60 facility. This would provide an opportunity to compare and overlap the results obtained from low-flux gamma measurements with those from the HollandPTC campaigns. At ESA ESTEC, the Co-60 source provides dose rates ranging from 0.36 – 72 Gy(water)/h [88], while at RID, a dose rate of 0.05 to 7446 µGy(air)/h was available. For reference, the proton irradiation at HollandPTC at 120 MeV produced dose rates between 0.057 Gy(air)/h and 45.91 Gy(air)/h[89].

These tests should ideally be conducted using new boards and fresh FGD-03F sensors, ensuring that the measurements are free from any effects caused by prior irradiation. This would allow for a more precise characterisation of sensor behavior.

4

Irradiation campaign at CERN CHARM

In the world, there are not many facilities that can test electronic devices in a mixed-field environment. During the thesis, the opportunity to carry out an irradiation campaign at CERN was presented. In this chapter, this campaign will be presented. First, the CHARM facility will be introduced (see section 4.1). This will be followed by an overview of the test setup, the pre-test characterization, and the dry run at CERN, as detailed in sections 4.2 to 4.4. This is followed by a preliminary analysis of the irradiation weeks, which lasted two weeks (see section 4.5). Finally, the results are discussed in sections 4.6 and 4.8.

4.1. The CHARM facility

The CHARM facility is located in the East Hall area of PS (see Figure F.7). This facility was constructed to test electronic systems in a variety of representative radiation environments, including particle, space, and atmospheric applications [90].
The Proton Synchrotron(PS) beam is directed towards multiple physics experiments within the facility using various beamlines. The T8 beam line supplies the proton beam to both the CHARM and IRRAD facilities. Since the IRRAD facility is located upstream of CHARM, it can influence the beam intensity reaching CHARM after the beam passes through it [91].
Upon entering the CHARM facility, the proton beam strikes one of three possible targets: a perforated aluminum target, a solid aluminum target, or a solid copper target. This interaction generates a mixed-field radiation environment that covers approximately 70 m^3. The layout of the CHARM facility, including the entry point of the proton beam and the target area, is illustrated in Figure 4.1 [90, 92].
The proton beam delivered from PS is structured into ”pulses,” known as spills[1]. Each spill lasts 350 milliseconds, with intervals of 1.2 seconds, forming a ”supercycle” consisting of around 30 spills. These spills are distributed across the different extraction lines of the accelerator. On average, the CHARM facility receives approximately three spills per minute, each spill containing around 3.1×10^8 protons [92].

The CHARM facility features four movable shielding structures, two made of concrete and two of iron, that allow for adjustments to the radiation intensity at specific positions. The experimental equipment can be installed in different ways within the facility. Firstly, the rack positions can be organized into three categories: the grid position (G0), the lateral rack positions (R1 to R9), and the longitudinal rack positions (R9 to R13). In addition to the rack positions, the facility also has two overhead conveyor locations (G15 and G16, see Figure 4.1) [86, 93].

The radiation environment in CHARM is highly diverse, comprising a wide range of particles, including protons, electrons, neutrons, kaons, pions, muons, positrons, and photons. The energies of these particles span an enormous spectrum, ranging from meV to GeV. Depending on the facility configuration,

---

[1] extraction of one or more bunches of particles over a period of time, with ”bunch” referring to a tightly packed group of particles traveling together in a beam

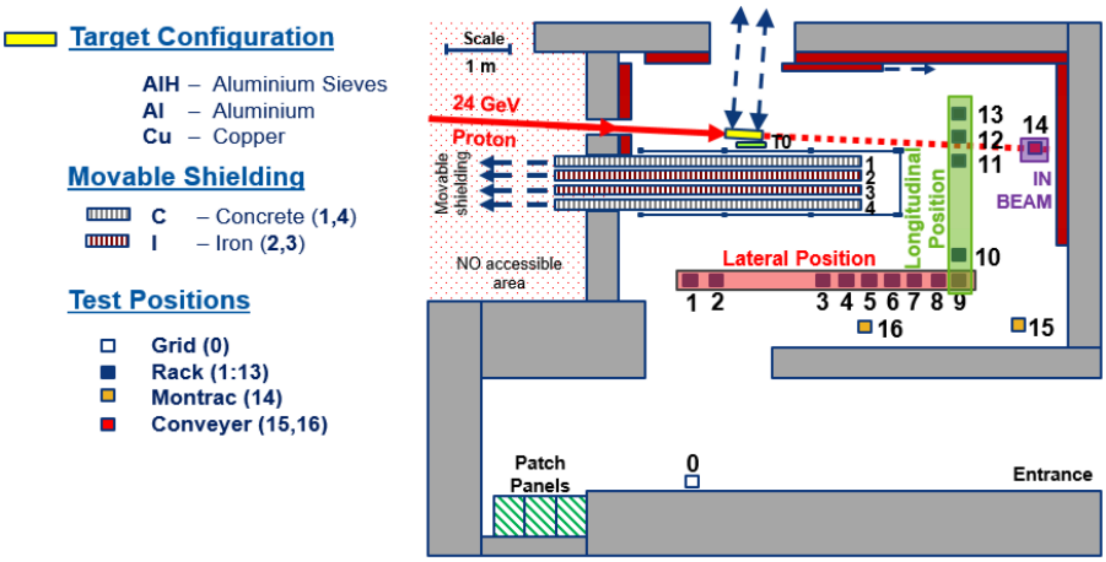

Figure 4.1: Layout of the CHARM facility, showing the 24 GeV proton beam impinging on a target. The colors of the Montrac and conveyor are inverted. During this test, the system was located at number 15, and no shielding was present. [86]

different spectra can be obtained. An example of the spectrum at R10, without shielding and a copper target, is shown in Figure 4.2.

During the irradiation, the users are provided with individual, time-based dosimetry. The system is called "RADMON" and provides TID, DD, (High-energy Hadrons) HEH, and thermal neutron fluences. The TID is directly measured using RADFETS [2].

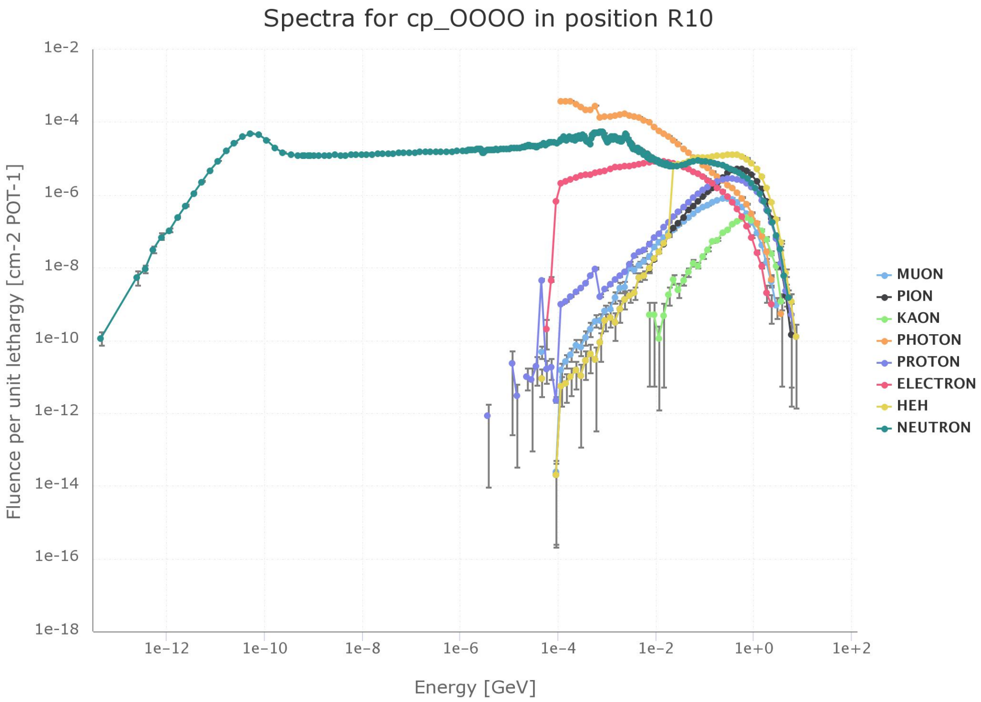

Figure 4.2: Mixed-field spectra inside CHARM for the configuration with Cu target and no shielding (CuOOOO) at position R10. Graphs where obtain by FLUKA Monte Carlo Modelling. [95]

---

[2] curious readers about RADFETS are pointed to: Holmes-Siedle et al. [94]

4.2. Experimental and scientific purpose

The objective of this experiment is to validate the current state of the radiation payload in a mixed-field environment. More specifically, this objective can be divided into three sub-objectives:

1. Verify the working of the radiation payload in a space-like environment.
2. Examine the difference in the characteristics of the daughterboard and mainboard in a mixed-field environment.
3. Assessing the feasibility of neutron detection with Floating Gate Dosimeters.

Below, the three objectives are discussed in more detail. Firstly, testing the setup in an environment that approximates the lunar conditions is crucial for understanding the mechanisms of radiation interaction with electronic materials. It helps evaluate how these effects contribute to device failure, characterize the device response, and determine the acceptability of production lots. Radiation tests are typically conducted in the laboratory to replicate the environment, where the most dominant effects of radiation are simulated. This is performed either using mono-energetic particle beams/sources with only one or few discrete energies[96]. However, in real-world applications, electronic systems are exposed to complex radiation fields composed of numerous particle types and energies. With the CHARM test, the radiation payload can be exposed to a mixed field, simultaneously inducing TID, SEEs, and DD, providing valuable insights into operational performance. The following system requirements can be tested, as outlined in Shanbhag et al. [2, Table 3.4]

RADPAY-PERF-1.1 The payload shall be able to measure TID up to [120] Gy.

RADPAY-RAMS-1.1 The payload shall be able to withstand TID up to [200] Gy in operation.

RADPAY-RAMS-1.9 The payload firmware shall be fault tolerant. [3]

RADPAY-RAMS-1.10 The payload shall be resistant to SEUs.

Secondly, in subsection 2.4.2 [4], it was outlined that the payload will be located at two different locations. One of the FGD-03F will be shielded by rover body [5]. It was reported by Shanbhag [2] that the shielding is expected to block most alpha and beta particles, while other radiation types may be altered based on their energy and type. Using the data received from this, the aim is to decompose the lunar mixed field and glean more information than a single FGDOS can. Testing this hypothesis provides insight into the quantity and feasibility of this design. However, this test will not be identical to the lunar environment, since the particles travel through several meters of air before reaching the detector, which acts as a shield for alpha particles and low-energy radiation. Nevertheless, depending on the results, the next iteration of the payload can be altered to increase the scientific yield.

Finally, as was mentioned in section 2.5, the FGDOS detect particles that create an electron-hole pair in the oxide. However, since neutrons carry no charge and therefore do not interact via the Coulomb force in matter, they can travel through many centimeters of material without any interaction, making them difficult to detect [19]. When a neutron does undergo an interaction, it is with a nucleus of the absorbing material. Resulting in the neutron being absorbed or producing secondary radiation. [19]. In a nutshell, the FGDOS has a low neutron sensitivity. A popular method for detecting neutrons is to add a conversion layer in close proximity to a conventional detector of charged particles, which transforms the incident neutron into secondary charged particles that can then be detected directly. The interaction changes dramatically with neutron energy and the type of conversion material. There are multiple materials commonly used as neutron converters, e.g., boron, cadmium, lithium, and ^{3}He, to name a few. For this experiment, cadmium and boron carbide (B^4C epdm 41%) were considered. Cadmium is a good thermal neutron filter, while boron carbide captures neutrons over a wider energy range (the plot can be found in Appendix H). By adding the conversion layer on top of a FGDOS, in theory, more gamma should reach the oxide, allowing the FGDOS to be used as a neutron detector. Due to the wide neutron spectrum at CHARM and the toxicity of cadmium, boron carbide was chosen for use.

---

[3] At the time of the project, The Lunar Zebro embedded software team was working on re-working the firmware. To minimize operation risk and streamline development.

[4] in particularFigure 2.15

[5] also known as the chassis

4.2.1. CHARM setup

To achieve the goals outlined in the previous section, two new radiation payloads were created, each containing a main board and a daughterboard. In total, four FGD-03F chips were used, each containing two sensors, resulting in a total of eight sensors. The De is shown in Figure 4.3.

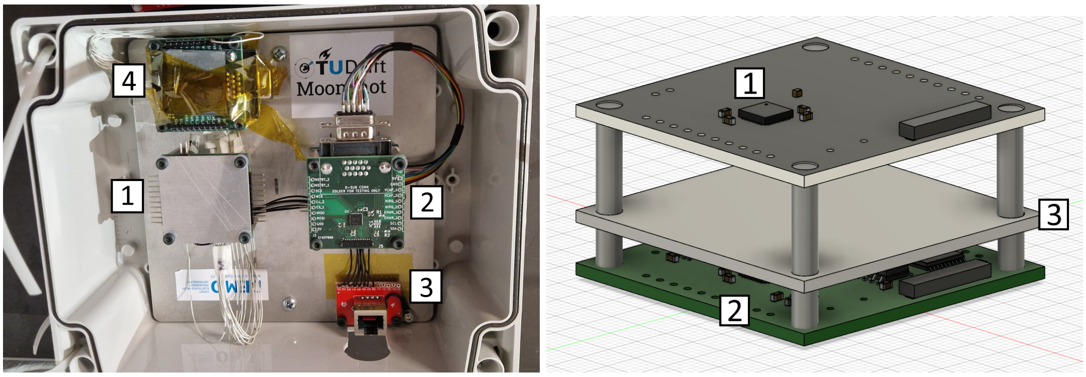

(a) View from the top. 1) Mainboard of setup 1, with sensor 1.1 and sensor 1.2.
2) Setup 2. 3) Ethernet input connector. 4) Daughterboard of setup 1 with boron carbide on top for neutron experiment. These are sensor 1.3 and sensor 1.4.

(b) An schematic side view of setup 2.
1) Sensor 2.3 & 2.4.
2) Mainboard with sensor 2.1 & 2.2.
3) 1.5 mm aluminium slab

Figure 4.3: The experimental device used at CHARM.

In designing the setups, redundancy was considered without adding unnecessary complexity.
The device begins in the lower right corner (see 3 in Figure 4.3a), where an Ethernet cable can be attracted. From the Ethernet cable, the wires are branched into two separate setups. Each setup bus contains four wires, namely the 5 V, RS485 A, RS485 B, and Ground. The setup on the left, named setup 1, has the mainboard and the daughterboard separate to not allow the neutron measurement to interfere with the measurement done by the main board (see 1 and 4 in Figure 4.3a). On the right, referred to as Setup 2 (see 2 in Figure 4.3a), the two boards are stacked on top of each other with 1.5 mm of aluminum sandwiched between them to simulate the shielding effect of the chassis. In the current rover design, this would be AL7075-T6[53], but for the experiment, another aluminum alloy was used [6]. In both setups, the aluminum was located ~5 mm above the mainboards and mounted with an M3x05 male/female stand-off.
The wires connecting the two boards were modified compared to the initial design. Due to a combination of transportation delays caused by internal factors and difficulties in remaking the intended cables, it was decided to solder the wires directly onto the board instead of using headers and wire housings for one of the setups. For the other setup, the previously created cables from setup 1 were used. These cables had never been exposed to an irradiation campaign but may have degraded over the past two years.

Risk analysis

Conducting tests at an external location carries certain risks, as the experiment cannot be easily repeated without incurring delays and additional financial costs. For this reason, the design includes some risk migration, mainly to prevent communication failures that could hinder the accomplishment of the experiment objective. A risk analysis was conducted, leading to two key decisions. Firstly, the two setups should operate independently to ensure that an issue in one does not affect the entire device. Secondly, in the event of a communication failure, the software should routinely write a data package to memory, ensuring data integrity and minimising potential losses. Each setup consists of an 8 Mbit FRAM, with data packets consisting of 41 bytes [7]. To save data within the memory limit, The total number of data packets is divided by the number of packets that fit in memory (rounded down). The

---

[6] from the 50xx or 6061 series

[7] A byte is 8 bit. One data packet consists of four sensor packets, each containing 3 bytes for sensor data, 3 bytes for reference data, 1 byte for temperature, 1 byte for the recharge counter, and 1 byte for the sensor ID. In addition, the data packets include 1 ODC byte (shared across all sensor packages) and 4 bytes for the time of saving, making the total size 41 bytes

result is then rounded up to determine how often each package should be saved. It was found that roughly every 23rd data packet should be saved when the sampling rate was set every 1.3 seconds.

Firmware

For the firmware, a modified version of code written by Shanbhag [2] was used, namely ”main v1.1”. The modification of the code includes additional functions for communication and saving to the data package. The rest of the code remained unchanged. In de subsection D.0.1, the pseudo-code of the used code can be found (see Table A.2).

Connection

To provide an overview of how the device is connected within the overall experiment, Figure 4.4 illustrates the connections for both the device in the CHARM facility and the corresponding connectors in the control room. Additionally, the custom cable created for the control side is illustrated in Figure 4.5.

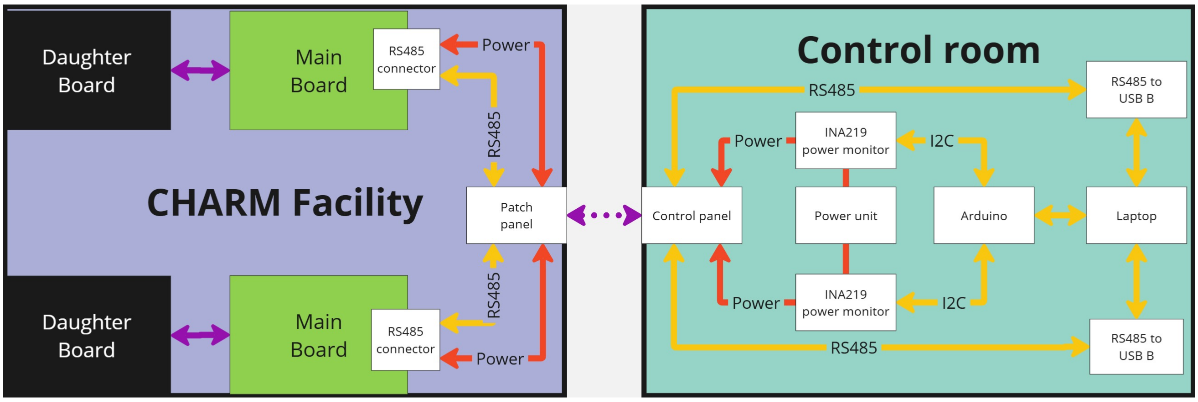

Figure 4.4: Illustration of the experimental setup that will be used for the testing at CHARM. Yellow lines represent communication lines, and red lines indicate power lines.

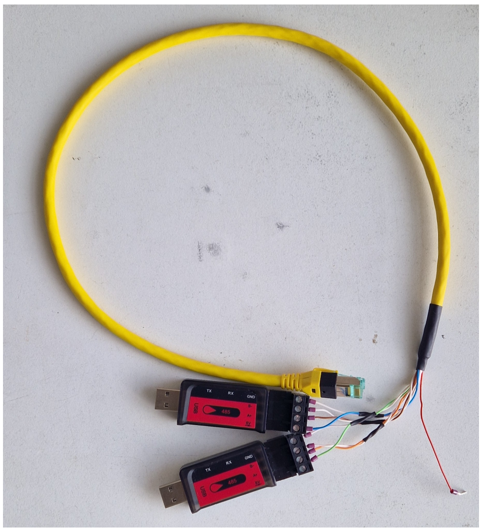

Figure 4.5: A custom cable is created to connect the monitoring system to the patch panel via an Ethernet cable. The two devices at the bottom are USB-B to RS-485 converters. Additionally, the red Ethernet wire serves as a dedicated ground (shield) for the setup. Orange - RS485 A for setup 1, brown - RS-485 A setup 2, green for setup 1 5 V, blue - setup 2 5 V. The white serves as the ground (GND) or the RS-485 B line, depending on the corresponding twisted pair color.

4.3. Pre-campaign characterization

Before going to the facility, the device needs to be characterized for temperature and irradiation sensitivity. Unfortunately, an extensive characterization campaign with the sensors was not possible due to truncated timelines resulting from delays in component delivery.

Temperature characterization

First, the temperature behavior of the sensors was characterized. This was done in the same way as outlined in Appendix B. In Figure 4.6, the raw data between the sensor and reference output is shown, while in Figure 4.1, the linear fit through the data is displaced.
From the data, it can be seen that the values are different for each sensor. This is to be expected, as each sensor has slight fabrication differences.

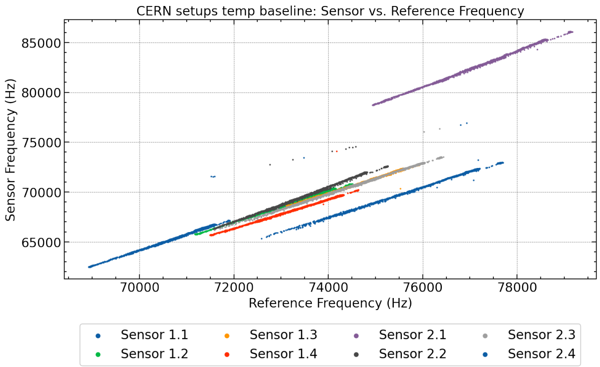

Figure 4.6: Raw data of sensor and reference output as a function of temperature.

Sensor	**Linear fit slope (± 1σ)**	**Filtered slope**
Sensor 1.1	1.626 ± 0.020	1.618
Sensor 1.2	1.595 ± 0.005	1.596
Sensor 1.3	1.538 ± 0.006	1.539
Sensor 1.4	1.462 ± 0.008	1.460
Sensor 2.1	1.813 ± 0.004	1.813
Sensor 2.2	1.775 ± 0.010	1.777
Sensor 2.3	1.552 ± 0.006	1.550
Sensor 2.4	1.534 ± 0.010	1.539

Table 4.1: Temperature correction coefficient for different sensors. The filter slope is the slope obtained by removing the outliers in Figure 4.6

Irradiation characterization

Next, the sensors were characterized using a Co-60 and Cs-137 sources. The same procedures and method described in chapter 3 are used. Between source switches, the setup remained in the same position and was not moved. In Table 4.3, the values obtained using this method are shown.

		Co60 $[4330 \pm 1000 \frac{\mu Gy}{h}]$		**Cs137** $[6472 \pm 1000 \frac{\mu Gy}{h}]$	
		Sensor response [Hz/s]	Sensitivity [kHz/Gy]	Sensor response [Hz/s]	Sensitivity [kHz/Gy]
Setup 1	Sensor 1	0.129 ± 0.005	29.8 ± 7.0	0.183 ± 0.003	28.3 ± 4.0
	Sensor 2	0.116 ± 0.005	26.8 ± 6.0	0.173 ± 0.003	26.7 ± 4.0
	Sensor 3	0.059 ± 0.004	13.6 ± 4.0	0.091 ± 0.003	14.1 ± 2.0
	Sensor 4	0.079 ± 0.004	18.2 ± 4.0	0.161 ± 0.003	24.9 ± 4.0
Setup 2	Sensor 1	0.111 ± 0.005	25.6 ± 6.0	0.138 ± 0.003	21.3 ± 3.0
	Sensor 2	0.121 ± 0.005	27.9 ± 7.0	0.155 ± 0.003	23.9 ± 4.0
	Sensor 3	0.090 ± 0.004	20.8 ± 5.0	0.189 ± 0.003	29.2 ± 5.0
	Sensor 4	0.119 ± 0.004	27.5 ± 7.0	0.190 ± 0.003	29.4 ± 4.6

Table 4.2: Temperature corrected sensors response rate (Hz/s) to different radiation sources at 0.85 m and the calculated sensitivity. For this, sources 4 and 7 were used. (see Table 3.1).

During the writing of this thesis, it was observed that the calibration was conducted very close to the radiation source, where the setup was not fully immersed in a homogeneous field (similar to what was observed in Table 3.3). As a result, the uncertainty was increased to account for this variation. Additionally, the dose rate decrease caused by slight differences in sensor positioning was not compensated for. This means that, for sensitivity calculations, it was assumed that all sensors experienced the same dose rate, which further contributes to the overall uncertainties.

Regardless, one key observation can be made about the results. Both Co-60 and Cs-137 exhibit the same sensitivity for all sensors except 1.4 and 2.3. The exact cause of this discrepancy is unclear, as aside from changing the source, the radiation field did not change significantly, and the setup was not moved. In particular, for sensor 1.4, determining sensitivity is challenging, as the measured values vary considerably across the IC, making it difficult to draw definitive conclusions at the moment.

Noise characterization

In Figure 4.7, a baseline measurement (no radiation) of setup 1 was conducted, where all sensor outputs were shifted back to zero. It can be observed that the data contains outliers. The data points above 4000 originate from the sensor reading the reference register map. The cause of the outliers closer to the mean is less clear. Regardless, as a first-order filter, most outliers can be removed using a moving average [8] on the data and discarding values that fall more than 1.5 standard deviations outside the mean.

Additionally, it is clear from the graph that all four sensors follow the same behavior. This fluctuation is caused by slight variations in temperature. At the beginning of the graph, all sensors show a rapid decrease, which is due to the initiation of the sensor. As a result, roughly the first minute of data acquisition should be taken with a grain of salt, as the clock speed (WCK) needs time to stabilize. However, since the reference exhibits the same behavior, this effect can be corrected by using the temperature compensation technique.

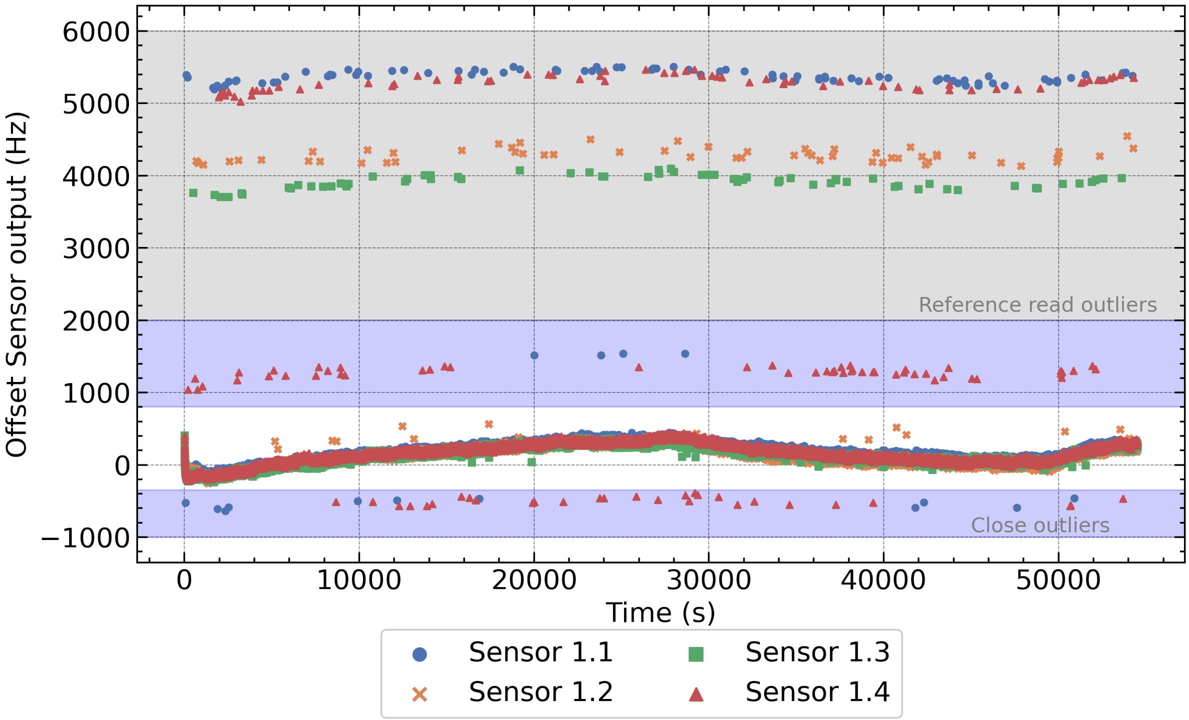

Figure 4.7: Raw data from Setup 1 during periods of no irradiation. The sensor data has been shifted to zero for easier comparison between the sensors. The highlighted region roughly marks two distinct types of observed outliers.

---

[8] For large outlier removal, a window size of 10 was used, whereas for smaller, close outliers, a window size of 15 was applied.

4.4. Dry-run testing at CHARM

Before the irradiation, users are required to install their system in a mock-up environment to verify its functionality, since significant modifications are no longer feasible once the system is in the facility.

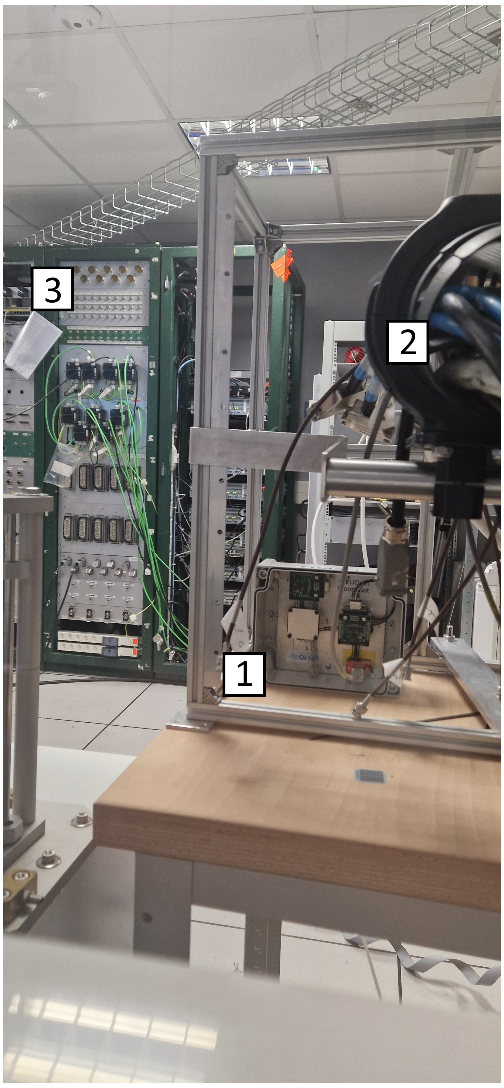

Figure 4.8: Overhead conveyor system in the mock-up room. 1) The device in the mock-up conveyor. 2) Provided cabling by CERN. 3) Patch panel on the control side to connect to the device under test.

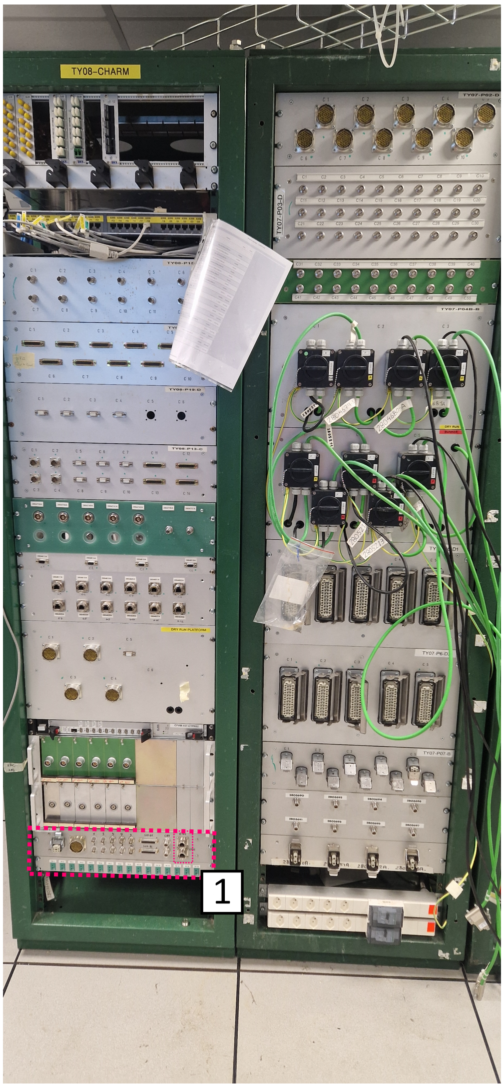

Figure 4.9: Patch panel in the mock-up room. 1) The connectors for the overhead conveyor, with on the right two Ethernet connectors.

The device was mounted onto the overhead conveyor in the mock-up environment using an Ethernet cable, as shown in Figure 4.8. This cable connects to a patch panel located on the opposite side of the room (Figure 4.9), with approximately 50 meters of cable in between. This setup allows the device to be connected to the monitoring system (laptop) in the control room. However, the long cable between the device and the control system leads to signal attenuation and a voltage drop. To mitigate these issues, RS485 communication was selected for the setups. This communication method was already used for rover communication and is well-suited for long-distance transmission.

The goals of the dry run were to:

- Evaluate the device functionality after transportation.
- Test the setup in a mock-up environment.
- Debug issues and implement additional code features.

- Complete safety training for the radiation-controlled area.

However, due to extensive flight delays to CERN, significant last-minute changes were made to the planning, resulting in less rigorous testing. Nevertheless, the conducted tests did not reveal any abnormalities, except for two anomalies. Firstly, the voltage drop across the mock-up system was:

- Setup 1 experienced a drop of approximately $1.1\,\mathrm{V}$ and had a power consumption of 220 mW.
- Setup 2 experienced a drop of approximately $0.3\,\mathrm{V}$ and had a power consumption of 80 mW.

The difference between the two systems is significant, and during the week, it was not possible to precisely determine the source of this high power difference. The voltage drop was corrected by increasing the input voltage, ensuring that the setup received a stable $5.0\mathrm{V}$.
Secondly, it was discovered that additional noise was present in Setup 1 when connected to the mock-up environment, as shown in Figure 4.10. The noise was only observed in the reference output of Setup 1, increasing in frequency with the sensor number. In even long-duration measurements, it was observed that the noise would occasionally stop without returning, with no notable change in the system. Various tests ruled out personal Ethernet cables, mock-up cables, and communication glitches. However, increasing the voltage appeared to mitigate the issue somewhat.

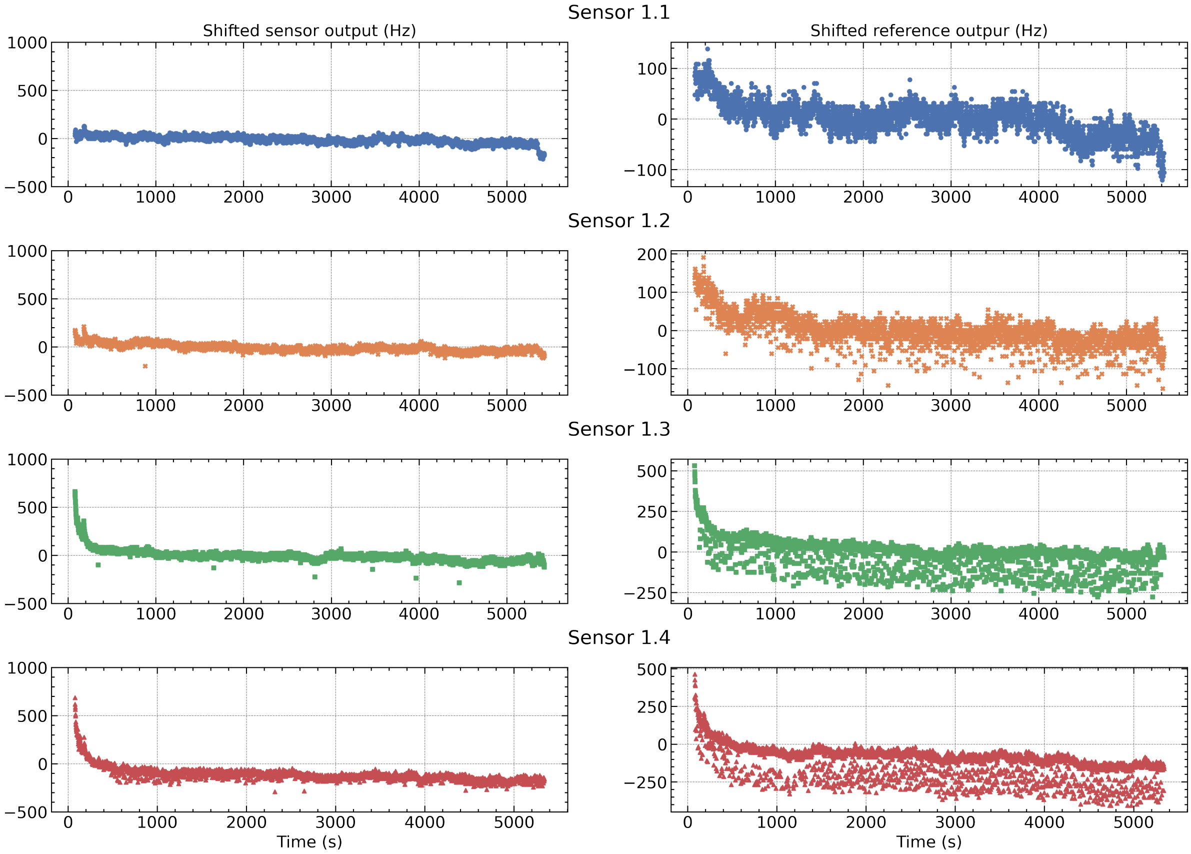

Figure 4.10: Noise Observation in Setup 1 as a function of time. On the left, the output of the four sensors is plotted, while on the right, the corresponding reference output is shown. It can be observed that after each increment, the noise level in the reference increases.

In conclusion, the mock-up environment provided valuable insights into the performance of the setups under conditions similar to those in the facility but without irradiation. Voltage drops and power discrepancies between setups were identified, and the use of RS-485 ensured reliable communication over long distances. However, without access to specialist equipment, resolving these discrepancies proved challenging.

4.5. CHARM Irradiation campaign

Following a week of dry runs, the device was ready for deployment within the facility. The setup was securely mounted to the overhead conveyor system using zip ties, as shown in Figure F.3. Throughout the weeks, the system was positioned at location 15, as illustrated in Figure 4.1. After verifying that the power levels were sufficient following the cable connections, the system was deemed ready for operation. The monitoring setup in the control room is shown in Figure 4.4, and an overview of the two irradiation weeks is presented in Table 4.3 (and Table 4.4).

Table 4.3: An overview of the two weeks of irradiation campaign.

Week	Beam on (CET)	Beam off (CET)	Noticible events
Week 1 (16-10 t/m 23-10)	16-10 13:23:20 18-10 15:52:41	17-10 17:30:24 18-10 16:37:35	- Sensors not recharging - Facility power outage and technical issues.
Week 2 (23-10 t/m 30-10)	23-10 21:03:21	29-10 01:09:31	- Setup 1 stop communicating (25-10 at 15:31:12)

4.5.1. Week one discussion

As shown in Table 4.3, the irradiation campaign spans a period of two weeks. This was initially planned to be a single week, as communication with the facility indicated that the first would be the last week of operation before heavy ion runs are conducted at CERN. During the week, the irradiation week was cut short due to a power outage [9] followed by the discovery of a water leak within the facility. This meant that the device accumulated only 47.6 Gy during this week. After discussion with the facility, an extension of the campaign was possible.

Additionally, despite thorough preparations, an unexpected issue hit the device. After confirming that the system was working correctly during the first 30 minutes of operation and then taking a lunch break, it was discovered upon return that all sensors had discharged to nearly zero without triggering an automatic recharge.

An examination of the code revealed that a commented-out section from a prior iteration, by Shanbhag [2], had inadvertently disabled the automatic recharging mechanism. Even though recharging was observed in the Appendix C test, this bug remained undetected during radiation tests of the device due to the compressed timeline. Further testing on a separate payload indicated that the system ignored the upper threshold and continued recharging indefinitely, which led to the original decision by Shanbhag [2] to disable the feature during proton testing at HollandPTC.

Efforts to utilize the backup communication system for the device were unsuccessful due to another bug that prevented the proper receiving of the command. As a result, the device was left running to collect as much data as possible.

During operation, it was observed that the system occasionally stopped communicating several times a day, requiring a manual power cycle to restore operation. Additionally, during the first night, sensor 1.3 (designated for neutron testing) experienced a SEEs that resulted in continuous recharging until a power cycle was performed. The effect is shown Figure F.6.

4.5.2. Week two discussion

Following the challenges of the first week, a second week of experimentation was made possible. Before the start of this week, issues related to communication and recharging were debugged and resolved. To address the issue of recharging, a trigger mechanism was implemented where the MCU would initiate a manual recharge. This was achieved by monitoring a moving average of 20 sensor readings, and if the value fell below a predefined threshold, the MCU would trigger a manual recharge lasting two MCU wake cycles. After this period, the recharging would stop automatically. The second issue related to communication was fixed by extending the listing time on the RS485. This resulted in setups that sampled every 1.906 seconds instead of every 1.337 seconds.

---

[9] During this time, power to the PS and CHARM was both off.

Furthermore, the logging laptop was replaced, switching from a MacBook to a personal Windows PC. The MacBook had been causing communication disruption errors and struggled to interface with all peripheral devices simultaneously. On the Windows PC, the ”RealVNC Viewer” was installed to enable remote access and real-time monitoring.

Preliminary Observations and Actions

When updating the firmware, the sensors were recharged beyond the linear range (see Figure F.4) as the recharge characteristics of each sensor were unknown. Consequently, the trigger threshold was set differently to migrate potential risk: Setup 1 was set at 42 kHz, while Setup 2 was set at 32 kHz. After radiation exposure, the sensors discharged back into the linear range. Once the sensor values dropped below the defined threshold, manual recharging was successfully triggered.

However, after approximately two days, it was observed that the recharging speed decreased as the TID increased. As a result, the sensors gradually recharged only partially, requiring recharging at shorter intervals. To mitigate this, communication-based recharging was used more frequently, effectively extending the interval between recharge cycles.

Setup 1 communication failure

On Friday, 25 October 2024, at 15:31:12, setup 1 stopped communicating entirely. After multiple power cycles, where only a single print statement[10] was transmitted back to the control room, but the signal never returned. Initial diagnostics revealed that the RS485 B-line voltage had dropped to 0.4 V instead of its usual level of approximately 2.2 V, suggesting a failure in the RS485 component. The exact cause of this issue is still unknown and will require a post-campaign diagnosis.

---

[10] This print statement was ”———”, Indicating the location where new data begins after a power cycle

4.6. Results

During the experiment, a ton of data points were collected. To avoid overwhelming the reader, a subset of the results will be presented. First, subsection 4.6.1 will display the data provided by the facility. Next, subsection 4.6.2 will discuss the functionality of the setup during testing to evaluate its performance. With an understanding of the individual components, the focus shifts to addressing the research question outlined earlier. Finally, subsection 4.6.4 will present a selection of interesting anomalies identified during the experiment. In addition, a visualization of the raw data, along with supplementary graphs, can be found in Appendix F

4.6.1. CHARM facility irradiation data

In this subsection, the values provided by the facility are displayed. First, let's examine the number of protons hitting the target per unit time, as shown in Figure 4.11. As seen in the data, the number of protons hitting the target is irregular, with significant differences between consecutive points. This variation is caused by the "super-cycle" mentioned in section 4.1. In the highlight section, slight variations between cycles can be observed. As a result, the device is not exposed to a singular dose rate but rather a mixture of dose rates, which closely resembles the expected condition on the lunar surface. Table 4.4 provides an overview of the details supplied by the facility, each contributing to characterize the radiation environment. For the remainder of the chapter, only the TID, POT, and sampling rate are considered relevant.

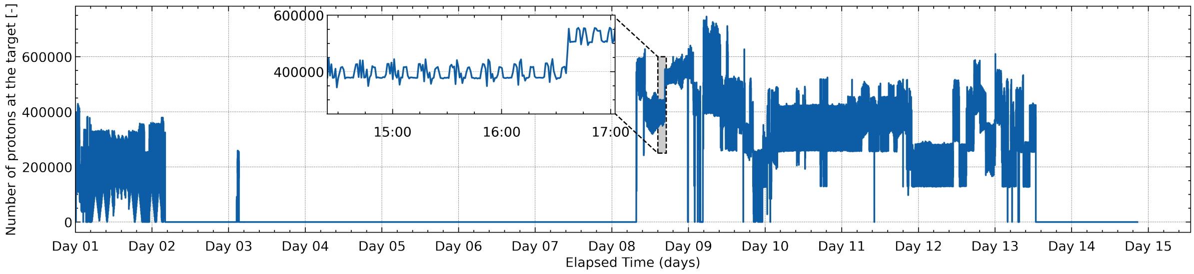

Figure 4.11: The number of protons reaching the copper target as a function of time during the two weeks of irradiation. It can be observed that the numbers fluctuate significantly.

Table 4.4: Summary of the irradiation campaign at CHARM, provided by the facility. TID = Total ionizing doses, HeH = High energy hadrons, N1MeV = Neutron at 1 MeV, Thn = Thermal neutron, POT = Protons On Target, DD/TID = Displacement Damage per TID, Rfactor = the fluence of thermal neutrons to HEH and, the sampling bin refers to the intervals at which data is provided during a given week.

	TID [Gy]	**HeH** $\cdot 10^{11}$ $[cm^{-2}]$	**N1MeV** $\cdot 10^{11}$ $[cm^{-2}]$	**ThN** $\cdot 10^{11}$ $[cm^{-2}]$	**POT** $\cdot 10^{9}$ [#]	**DD/TID** $\cdot 10^{10}$ $[cm^{-2}Gy^{-1}]$	**Rfactor** [-]	**Sampling Bin** [s]
Week 1	47.6	2.08	5.90	1.62	1.02	1.24	0.779343	19.24422
Week 2	95.6	4.19	1.37	3.27	3.27	1.43	0.779343	45.05961
Final value	143.5	6.28	1.96	4.89	4.67	1.33	0.779343	-

4.6.2. Functionality of the radiation payload

The device consists of multiple components that must function properly to ensure reliable and accurate data. To understand the broader picture, it is first necessary to examine the individual components. Below, the data is analyzed from a macro point of view before focusing on the FGDOS.

Micro controller

The MCU is the hearth of both setups. Figure 4.12 presents a snapshot of various observables over time, with different characterizations separated. Let's examine subplot 3, which illustrates the time difference between consecutive data packets arriving at the monitoring system. From this, distinct operational modes of the MCU can be identified, lining up with expectations based on the firmware

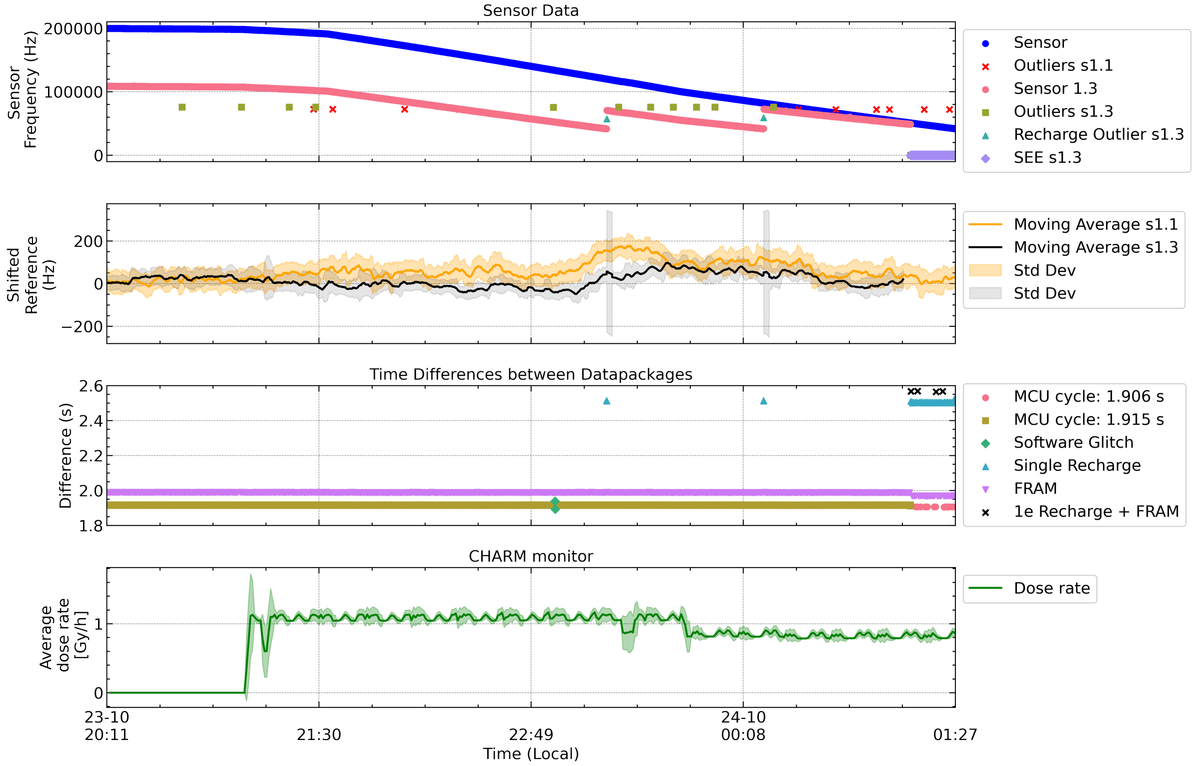

Figure 4.12: Snapshot of the setup 1 during week 2 of irradiation. In the first graph, the raw sensor output data of sensors 1.1 and 1.3 are displayed. In the second graph, the reference data for those sensors are plotted with an offset relative to the starting position solely for comparison purposes. In the third graph, the time difference between the arrival of data packets at the PC is displayed, highlighting the different operating modes of the MCU. Finally, the reported dose rate has been plotted. A moving average of 3, along with one standard deviation, is applied to the data to highlight trends.

(seesubsection D.0.1). Under normal conditions, the MCU transmits data every 1.906 s. Every 15 cycles, the current data packet is stored in FRAM, resulting in an additional 0.070 ± 0.006 s to the cycle duration.

Beyond routine operation, when one of the sensors in the system goes below a certain threshold, a recharge is triggered. This adds an additional 0.59 ± 0.03 s to the cycle. A superposition of those modes can occur, such as when multiple sensors require simultaneous recharging or when a recharge event coincides with a data-saving operation. Other functional states include command execution, system initialization after the power cycle, and power cycling itself, each operating with a predefined duration.

Deviations from these predefined modes may indicate the occurrence of SEEs or firmware glitch. As shown in Figure 4.12, multiple operation states and disruptions are observed. Firstly, at the end of the graph, an SEEs likely toggled the NSTBY of sensor 1.3 from an active high to low, forcing it into standby and causing it to return only zero values. The MCU interpreted this state as requiring recharging and persistently attempted to initiate a recharging cycle. However, by the time a power cycle reset the system on 24-10 at 07:12, the damage was already done, and the sensor reading had drifted to 292k. Secondly, the figure also shows a firmware glitch, where probably a high-energy particle interaction within the MCU caused a temporary deviation from the expected cycle (for two cycles). The exact mechanism and cause are not of primary concern. Rather, the key observation is that those glitches do occur.
With this understanding, the analysis can be expanded to the full dataset from the second week, providing insight into the various operational states. During this period, the system experienced instances where it failed to communicate with the external environment. These disruptions were caused either by an MCU failure or the transmission failure institute by the RS-485 transceiver. Moreover, even when no timeout occurred, anomalous data points were still observed, such as:

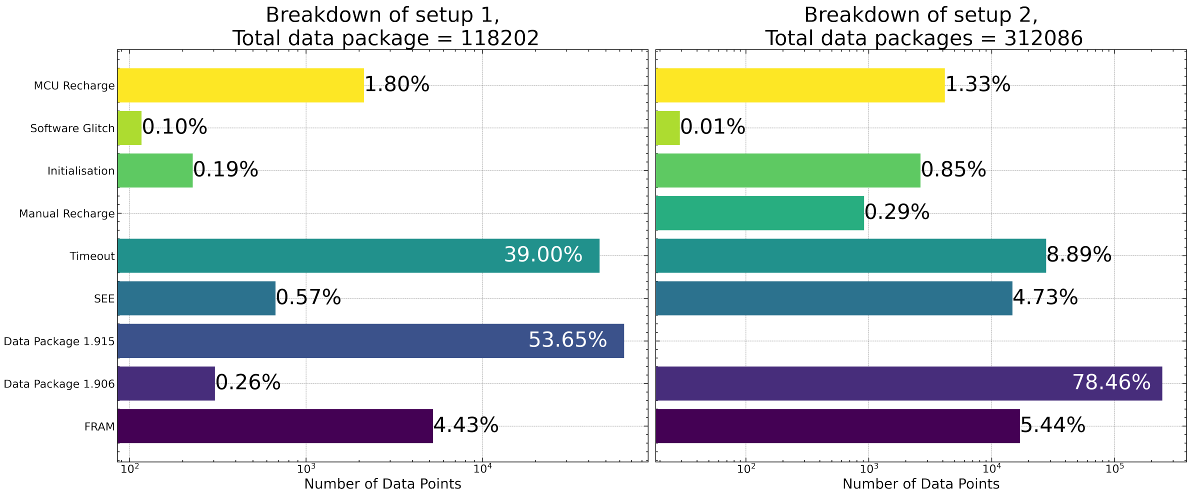

Figure 4.13: MCU operational mode for Setup 1 and Setup 2 during the second irradiation week. Setup 1 lost approximately two-thirds of the data due to a communication issue, while Setup 2 remained fully operational.

- Failure in decoding of communication protocol.
  - Incorrect combination of separate data bits within a data packet
  - Insertion of extra characters and/or numbers, e.g., the addition of random zeros
  - Loss of portions of the data packet.
- System receiving unauthorized commands, e.g., '1ere0,' which did not trigger any response.

Using this knowledge, Figure 4.13 can be constructed. This figure illustrates the occurrence of different operational modes throughout the total duration. SEEs and timeout events are categorized separately, depending on whether the data exhibited an offset or if no data was recorded during that period.
From Figure 4.13, it is observed that the system operates as intended overall. A notable consideration is that the timeouts and SEEs could be further reduced by implementing a firmware-based mechanism to automatically trigger a power cycle when necessary. Towards the end of the week, a mechanism was introduced to initiate a power cycle whenever a data packet was not received within two minutes. This led to an increase in initialization time but resulted in a reduction in both timeouts and SEEs duration. Finally, no measurable slowdown in system operation was observed during radiation exposure.

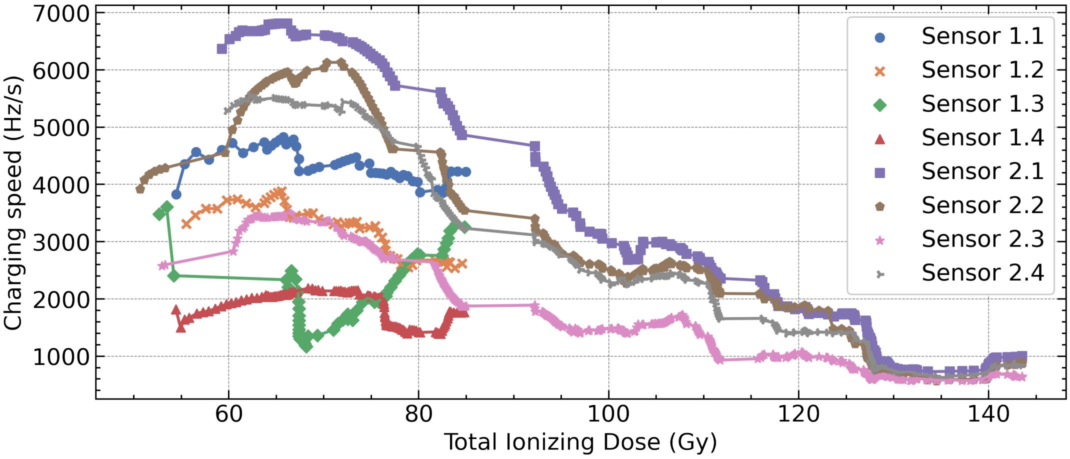

Figure 4.14: The average recharging speed of different sensors as a function of TID. A centered moving average with a rolling window of 30 was applied, ensuring that at least one data point was included per window. This helps highlight the overall trend, as abnormalities and high-flux radiation cause fluctuations in the recharging speed.

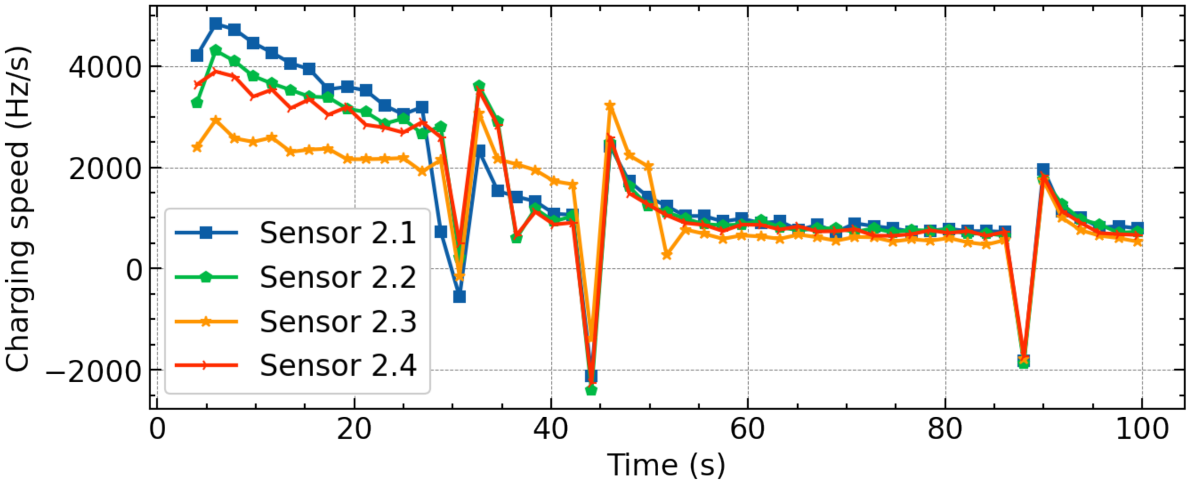

Figure 4.15: Sensor recharging speed as a function of time. This is a command-based recharging event at 140.1 Gy. The global decreases below zero indicate the arrival of high-flux radiation. Sensors started at approximately 34 kHz ± 2 kHz and stopped at around 110 kHz ± 10 kHz.

Recharging FGDOS

During the second week, a decline in sensor recharging speed was observed. Figure 4.14 illustrates the charging speed of each sensor as a function of TID. The first notable observation is the variation in the starting position. Without the historical data from the initial $\sim$ 50 Gy of exposure, it is impossible to determine whether this difference originates from inherent sensor characteristics or if an upset event during irradiation has altered the recharge behavior. For instance, sensor 1.3 experienced a SEE event, as described in subsection 4.6.2, resulting in frequent recharge triggers. After a power cycle, a noticeable drop in recharging speed was observed. Combined with SEEs that occurred during the first week, this explains the deviation of sensor 1.3 from the other seven sensors. Secondly, a correlation appears to exist within each setup. Sensors within the same setup exhibit similar characteristics, while differences are more pronounced between them. This variation may arise from multiple factors, including the setup voltage, setup current, and the operational speed of the MCU. Finally, it was observed that the recharging speed was not constant. Figure 4.15 illustrates a command-based recharge at 140.1 Gy. The recharging speed[11] decreases as more charge accumulates in the FG. A drop below zero indicates the arrival of high-flux radiation at the sensors. This suggests a non-linear relationship between charge accumulation and recharging speed, possibly due to circuit limitations, internal resistance, or voltage regulation effects.

Current monitoring

To monitor the voltage and current consumption of the setup, a current sensor[12] was connected in series. Due to device issues with the MacBook (as discussed in subsection 4.5.2), current monitoring was only successfully installed on day 8 of the radiation campaign. Figure 4.16 illustrates the power consumption of setup 2 during the second week. Now, let's break down the graph. The highlighted region represents nominal system operation. Every time the setup transmits data back, it is accompanied by a power spike. Due to these high power fluctuations during normal operation, a rolling average of 75 points is applied to smooth the data out. This reveals a noticeable increase in power consumption, rising from 105 mW to 240 mW when the beam was shut off. In the following hours, annealing was observed, resulting in a decrease to 235 mW by the end of the measurement.

Additionally, anomalies such as timeouts, SEEs, and power cycles are superimposed on the graph. Each of these anomalies has its distinct characteristics. For example, timeouts and power cycles generally appear as downward spikes, while SEEs and other glitches are observed as increases in power. Below, an overview of various events that led to a power increase is discussed.

---

[11] The SET registry map bit was at 16.5 V

[12] Adafruit INA219

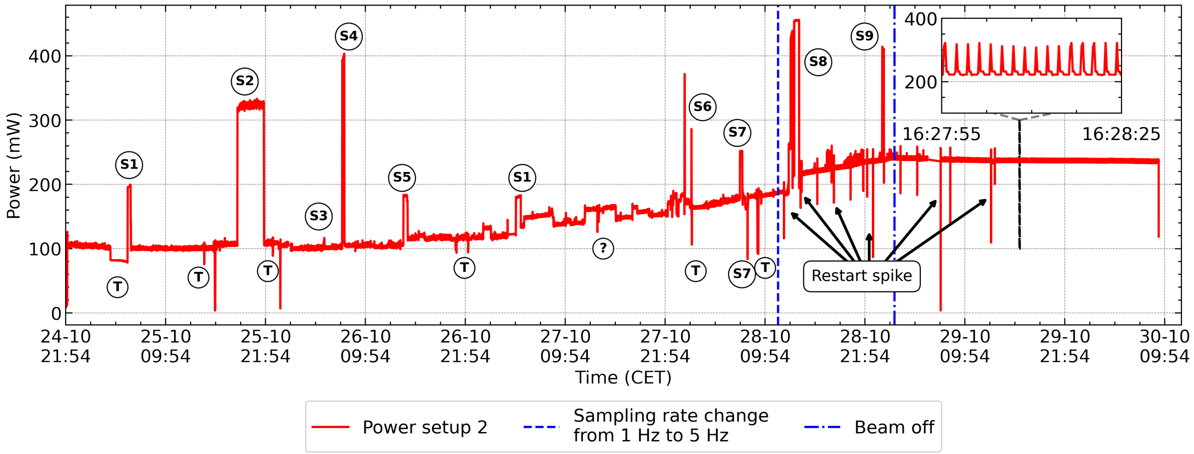

Figure 4.16: Power consumption during the second week of operation for setup 2. The highlighted section displays a small segment of the raw power consumption, while the overall graph shows a rolling average of 75 to smooth out normal operational power variations. Various features can be observed in the graph: timeouts are marked with (T), SEEs with (S), and unknown events with (?). The data spans a TID from 71.1 Gy to 143.5 Gy.

- S1: After possible manually returning from a timeout, all FGDOS sensor values had discharged to zero. A firmware bug related to manual recharging below 10,000 caused the MCU to glitch. A power cycle resolved the issue.
- S2: A power spike caused a 2 kHz jump in sensor and reference values. During this, the voltage dropped from 5.05 V to 4.87 V, while the current increased from 20 mA to 65.1 mA. Despite nominal data values, the recharge speed was lower. A power cycle resolved the issue.
- S3: All sensors reported only zeros for reference, sensor, and temperature values. A power cycle resolved the issue.
- S4: A current increase caused an offset of 5k in sensor 2.1, while other sensors remained unaffected. A power cycle resolved the issue.
- S5: Sensor values fluctuated between zero and nominal for ± 50 seconds, followed by a timeout with abnormal data points every ± 527 seconds. A power increase from 104 mW to 116 mW was noted.
- S6: Two events: First, periodic additions and removals of extra numbers led to a power spike. Second, there is a sudden drop to near zero in all reference outputs. Both were resolved by a power cycle.
- S7: Sensor 2.2 reported incorrect values (~704 kHz, exceeding the sensor limit of 430 kHz). Later, it dropped to 300 Hz, triggering the S1 bug. After a power cycle, it worked fine until sensor 2.2 was pulled low, causing only zeros to be recorded, which led to a small timeout. This issue was resolved by a subsequent power cycle.
- S8: All sensors and reference values dropped by 2.7 kHz, with new data points logged every 67 seconds. A power cycle temporarily reset the system, but a timeout and another power increase followed.
- S9: A current increase was observed alongside discontinuous jumps in sensor and reference outputs. A power cycle resolved the issue.

4.6.3. Irradiation Sensitivity

Having understood the global picture, the focus now shifts to FGDOS, beginning with observation from the first week of the experiment. During this period, a SEEs event caused the sensor to trigger a continuous full recharge, and following a power cycle, it underwent a complete discharge, as shown in Figure F.6. Throughout this discharge, the average dose rate remained approximately constant, making it possible to derive a sensitivity curve over the FG range. The data was binned every 215 points to ensure a sufficient number of data points per interval, resulting in 15 facility points. Afterward, sensitivity was calculated within this range. For the uncertainty, a first-order approximation assumed that there were two constant dose rate[13] during this period, allowing facility-related uncertainties to be ignored and considering only the uncertainty in the sensor response. However, this assumption is not entirely valid, as can be seen in Figure F.6. Nevertheless, under this assumption, the sensitivity as a function of charges accumulated on the FG can be plotted, as illustrated in Figure 4.17. Additionally, it was assumed that sensitivity as a function of TID remains unchanged. However, previous research has shown that this is not the case (see Figure 2.21).

The graph illustrates that the highest sensitivity is achieved when the sensors operate within the linear range [50–90 kHz]. For practical applications, this region could be extended to cover a broader range, provided that corrections are applied afterward to account for variations in sensitivity. Such an extended operational range could be particularly useful during SPE.

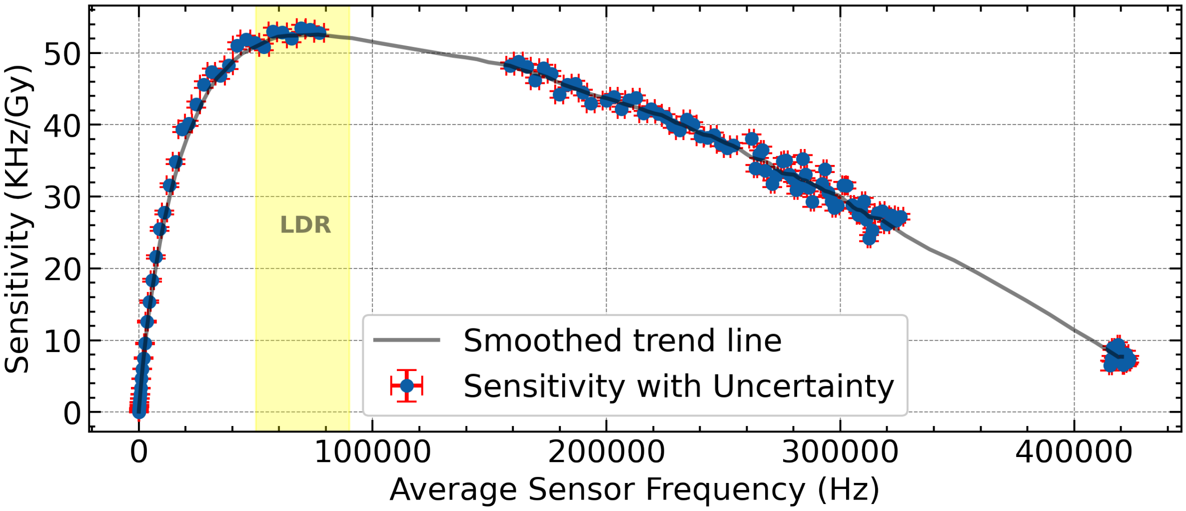

Figure 4.17: Sensor 1.3 sensitivity as a function of the charge amount on the FG. The measurement covers a TID range of 29.4 Gy to 44.6 Gy. The sensor experienced two timeouts, which are visible in the graph. However, due to the nature of the floating-gate sensor, discharge still occurred. The uncertainty in the dose rate was not taken into account in the analysis. LDR = Linear Dynamic Range, as reported in the datasheet.

Sensitivity as a function of TID

To address the impact of shielding and the addition of boron carbide, the data is divided into two segments: week 1 and 2. Figure 4.18 illustrates the sensitivity of the different sensors in the device during the initial irradiation in CHARM, with the sensitivity calculated using Equation 2.10.

The first observation is that each FGDOS IC are segmented closely related, with sensors 1.1 and 1.2 appearing as outliers, sandwiching the other values. This is unexpected, as the control IC (sensors 2.3 and 2.4) was anticipated to be the most sensitive, having been exposed to the whole mixed field. In contrast, the IC with 1.5 mm Al shielding, followed by the IC with 1.5 mm Al and PCB shielding, was expected to exhibit lower sensitivity. The FGDOS with born was expected to be positioned between or above these values, depending on the effectiveness of neutron conversion. When the sensor values within a single FGDOS IC are averaged, the outlier effect diminishes, resulting in a sensitivity value

---

[13] In the frequency range of 262.07 to 312.91 kHz, a dose rate of 1.0700 Gy/h was used, while for the remaining range, a dose rate of 1.8417 Gy/h was applied.

of 65.3 kHz/Gy. This suggests that the addition of boron carbide to the floating gate increases the sensitivity, while both types of shielding reduce the sensitivity.

Another key observation is that the initial sensitivity aligns closely with previously reported values from the Sealicon data sheet [4]. If a complete uncertainty calculation were performed, the fluctuations in proton delivery would result in a large standard deviation and, consequently, a significant 1σ uncertainty in the sensitivity. For the data point at 0.05 Gy, the estimated sensitivity uncertainty would be ±6.1 kHz/Gy, while for the second point, it would be ±13.6 kHz/Gy. However, since data points at the same TID are exposed to the same dose rate,[14], the uncertainty would only introduce an offset. For this reason, only the uncertainty in the sensor is included.

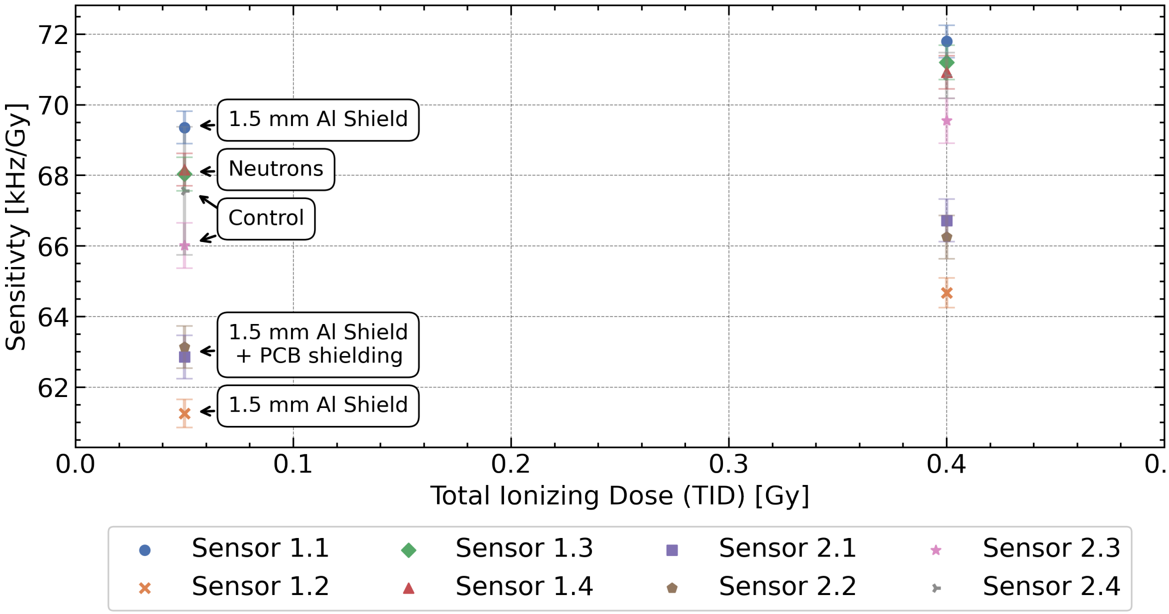

Figure 4.18: Sensitivity of the FGDOS during the first few Grays in CHARM. At TID = 0.05 Gy, the dose rate was 1.35 ± 0.1 Gy/h, while at TID = 0.4 Gy, the dose rate was 2.31 ± 0.7 Gy/h. Only the uncertainty related to the sensor response is displayed, as uncertainty in the dose would introduce a uniform offset across all values. All uncertainties are reported at the 3σ level.

Next, this analysis can be extended to the data obtained during the second week. However, due to the number of fluctuating parameters - dose rate, voltage-current characteristics, temperature, sensitivity as a function of TID, sensitivity as a function of operation range, and the history of the sensor, it was not yet possible to derive a quantitative conclusion from the results. This does not imply that the sensor data are invalid, but rather that the current analysis is undercooked. For this reason, the analysis has been moved to Appendix J. The key takeaway was that, in addition to further study, the experiment could be replicated in the future under a more stable mixed-field environment with a higher facility sampling rate to reduce measurement uncertainties.

---

[14] The creation of secondary radiation occurs as a function of θ and ϕ, resulting in minor dose rate differences at each sensor. Additionally, wires in the line of sight may have slightly modified the dose rate at different sensors. However, these effects are considered negligible, and it is therefore assumed that all sensors are exposed to the same dose rate.

4.6.4. Unexpected observations

During the experiment, some unexpected results were observed. Notably, the sensors exhibited a recovery time after a specific dose, and their response after beam shutdown showed intriguing behavior. Each of these observations is briefly discussed below.

Recovery phenomena

Unlike other facilities, where sensors experience a continuous radiation stream, CHARM, the radiation exposure occurs in high-intensity bursts when the 24-Gev proton hits the target. These bursts are followed by short periods during which the sensor primarily detects lingering radiation resulting from the activation of surrounding materials.

As the sensors were subjected to increasing TID, their response to radiation burst exhibited a progressively steeper drop, followed by a recovery period. This effect is illustrated in Figure 4.19 for sensor 2.1, though similar behavior was observed across other sensors. Notably, sensor 1.3 began exhibiting this behavior significantly earlier than the others.

An initial analysis of this recovery behavior indicates that an exponential saturation model fit provides a good fit, particularly in later stages:

$$\text{Sensor output} = A \ \cdot (1 - e^{-(t-t_0)/\tau}) + C \tag{4.1}$$

where t_0 represents the time at which the drop has occurred, τ is the recovery rate, C is a vertical offset, and A is the amplitude of the response. Due to time constraints within this thesis, a fully quantifiable model of the recovery behavior as a function of TID could not be created. However, a several key observation can still be made.

Firstly, the recovery behavior appears to be influenced by the dose rate, with higher dose rates leading to steeper drops, as observed in the graph.

Secondly, the timing of the observed drops does not consistently align with the reported bursts of irradiation. While the facility provided updates every 45.0 seconds during the second week, the nature of the supercycle caused bursts to occur at varying intervals. Personal observations indicated that bursts occurred every 10 seconds at times, while at other times, they occurred every 30 seconds. This, coupled with slight noise in the data, makes pinpointing the exact moments where the bursts occur challenging. A sliding window approach was tested to detect the onset of drops in the data, but the results were mixed. The phenomenon was likely caused by degradation in the readout circuitry.

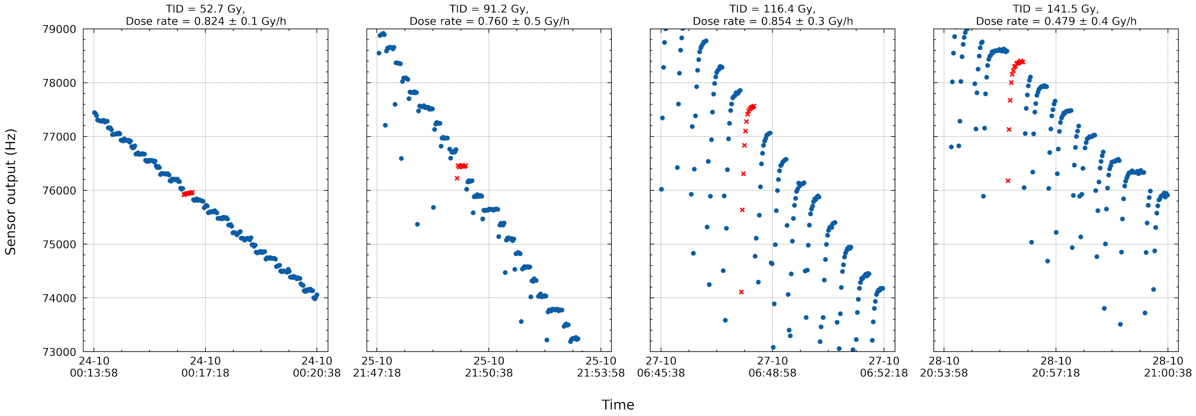

Figure 4.19: In blue (o), the raw sensor 2.1 data at different TID levels is shown, while in red (x), a highlighted segment represents the data between consecutive radiation bursts. All uncertainties are reported at the 3σ level.

Post-irradiation characteristics

On 29-10 at 01:09:31, the beam was stopped, leaving the sensor exposed only to residual radiation resulting from the activation of surrounding materials. As observed in Figure C.5, it is interesting to monitor the behavior of the sensors after the beam is shut off. This is illustrated in Figure 4.20, where the temperature-corrected values are plotted. The initial post-irradiation data is excluded but can be seen in Figure F.2, as the system was operating around 33 kHz, which falls within its non-linear range. From Figure 4.20, it is evident that the sensor response continues to decline even after the beam is stopped. However, compared to known nuclear laws, the response does not follow an exponential trend. The sensor response appears to fluctuate between different dose rates, alternating between acceleration and deceleration. The following observations are made. Firstly, the complete facility and device post-irradiation is highly radio-active. Measurements indicate that the activation on Wednesday morning was approximately 100 µSv/h at the rack connection point[97]. Due to the presence of high-energy neutrons (see Figure 4.2), neutron capture and spallation processes can occur, leading to the formation of a wide range of radioactive isotopes. Various elements are expected to become activated, including:

- Silicon and oxidation layers (e.g., in FGDOS),
- Copper (e.g., in wiring and PCB)
- Tin, lead, and bismuth (e.g., in soldering materials),
- and nickel, silver, and gold (e.g., in PCB coatings).

Most of the mentioned elements have half-lives ranging from a few minutes to a few hours. However, some isotopes present will undergo radioactive decay over significantly longer periods, lasting months or even years. This is observed in the gamma spectroscopy, illustrated in Appendix E. After 85 days, 21 nuclides remain radioactive, contributing to an ambient dose rate of 0.079 µSv/h.
Secondly, comparing the different signals, indicates that this is more of a global effect rather than a sensor-individual effect. If an individual effect, such as annealing, were dominant, the slopes would exhibit significantly different. This does not imply that annealing is absent but rather that it is not the primary contributing factor. Finally, four power cycle spikes can be observed in the graph. Even though temperature compensation has been applied, these spikes remain visible for sensors 2.3 and 2.4, while they are absent for 2.1 and 2.2. This may indicate that the compensation coefficient has shifted. A post-irradiation can confirm this shift.

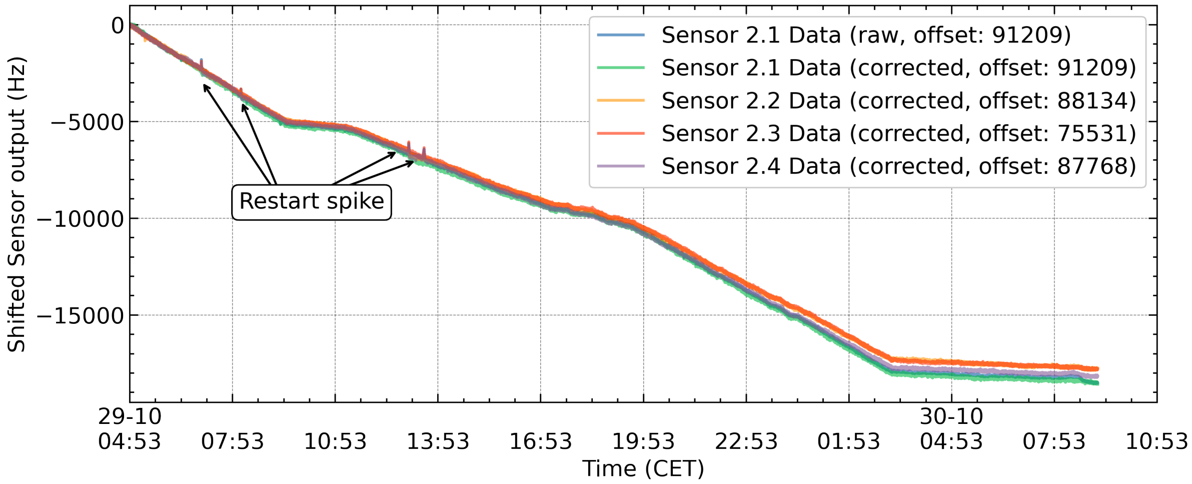

Figure 4.20: Post-irradiation sensor response as a function of time. The sensor output is shifted to zero to allow for comparison. The data only shows the values that are in the linear range of the sensor.

4.7. Post-irradiation investigation

The final tests for the device, conducted after the CERN campaign, aimed to study its characteristics in a more controlled environment. However, due to external factors, the timeline of experiments with the device was delayed beyond the scope of this thesis. A spectrum of the radioactive isotope was recorded on 22 January 2025, and the results are presented in Appendix E. These results indicate that the device was safe for transport to RID. Despite time constraints, the following investigations were initially planned.

Firstly, an electronic investigation was necessary. One of the setups stopped communicating midway through the experiment. The primary assumption is that the RS-485 transceiver component caused this failure, but further investigation is required to confirm the exact cause. Additionally, setup 1 exhibited high power consumption (before and during), which is suspected to be due to either main-to-daughterboard cabling issues or a faulty component on the board.

Secondly, a recalibration investigation of the setups was planned, including both temperature correction and gamma calibration, as outlined in section 4.3.

Finally, an extension of system characterization with protons was proposed using the HollandPTC facility. The test plan involves an initial exposure to 120 MeV protons at a low dose rate (approximately 0.39 Gy/h) over an extended period of time. Subsequently, the dose rate and energy can be gradually increased to approximate the conditions at CHARM. These tests aim to extend system exposure up to 200 Gy, allowing for the validation of a system requirement and the investigation of shielding effects and potential indications of recovery behaviour.

4.8. Conclusion and recommendations

In this chapter, the CERN irradiation campaign was discussed. As outlined in section 4.2, the experiment aimed to investigate the behavior of the Floating gate in a mixed-field environment to validate the current design and to inform design decisions for the future. Below, the different sub-goals are shortly discussed:

- (1) Verify the working of the radiation payload in a space-like environment.

Depending on how you look at it, the four system requirement tests were not passed. One of the setups stopped communicating after 85.0 Gy, indicating that the system is not entirely resistant to the radiation environment. In contrast, the other setup continued to operate until the end (143.5 Gy). Without complete post-irradiation characterization, it is difficult to determine whether the issue is a fundamental design flaw or a specific system problem. Due to facility-related challenges and operational issues, the target of 200 Gy was never reached, and therefore, the second requirement could not be tested. The firmware was not the whole focus of the experiment, as the Lunar Zebro embedded system is currently working on updating firmware for operation. Regardless, the issue of automatically recharging not working is a critical issue. However, with the implementation of a manual recharge trigger (e.g., at 43 kHz), the operational risk can be reduced. This is if all edge cases are correctly considered. Finally, several timeouts and single events were observed during the testing process. All could be reduced by implementing the watchdog and firmware that could detect errors and enable a power cycle.

- (2) Examining the differences in characteristics between the daughterboard and mainboard in a mixed-field environment, and (3) assessing the feasibility of neutron detection using floating gate dosimeters.

As shown in Figure 4.18, a slight increase in sensitivity to neutron detection was observed compared to the control, while the two shielded sensors exhibited a slight decrease. In this case, assuming that all sensors experienced the same initial particle composition before being modified by the shielding material, the differences in detection provide an indication of the ratio of certain particle types within the mixed-field environment.

By using Monte Carlo simulation software, more quantitative results could be obtained, providing deeper insights into the radiation environment and helping to address the mission objectives. However, the conclusive measurements were limited and contained several uncertainties. For instance, the significant difference in sensitivity between sensors 1.1 and 1.2 during the first week, along with the challenges in obtaining reliable sensitivity measurements during the second week, indicate unresolved issues. Addressing these limitations through future work will be essential to get more robust and interpretable results.

Recommendations for future experiment

As this may not be the last time parts of the Lunar Zebro rover were tested in a mixed field radiation environment[15], this subsection provides a concise overview of key lessons that I would take into account if starting over from scratch.

- Firstly, I would consider increasing the size of the PCB for testing purposes, allowing for the use of more standardised headers to simplify connections. In the current configuration, creating custom cables for the Hirose DF-13 connector proved challenging, requiring experience with a specialised crimping tool. Although this header is necessary for the mission, a more development-friendly board could be designed specifically for testing.

  Expanding the PCB would also allow for the integration of additional sensor components[16]. This would enable more extensive testing of different operational modes and facilitate greater data transmission to the control room.

  However, while modifications for testing purposes would provide more flexibility, the design should still closely resemble the original functionality. It is crucial to balance additional features with system reliability, as increased complexity introduces more potential failure points.
- I would expend the timeline with specific tests that need to be conducted before a go-no-go moment. This timeline would present a list of critical functionality, and it would make sure that those are tested. For example, the issue with recharging could have been flagged earlier in the process if the planned extended pre-campaign calibration had been conducted.
- I would investigate the possibility of adding an extra redundancy line to ensure that data can still be transmitted to the control room in case the RS485 transceiver fails, similar to what happened during the loss of communication in Setup 1 during the experiment. In this case, a simple solution would be to add an additional RS485 receiver to the UART lines, providing an alternative communication path.
- I would investigate a method for remotely updating the firmware from the control room, even though this would likely be challenging, as firmware updates require Spy-by-Wire communication protocol, which would be significantly attenuated over the extended transmission distance. However, in the worst-case scenario, having this capability would be crucial for continuing the experiment.
- I would aim to establish a more robust infrastructure for live monitoring and post-processing during the experiment, enabling rapid adjustments when necessary. This would include additional firmware-related triggers to help identify key relationships and detect critical events in real time.

  To facilitate broader accessibility and collaboration, this system could potentially be integrated into a web-based interface, allowing multiple team members to monitor results simultaneously. This approach would reduce reliance on an on-site observer for validation, thereby improving the reliability in detecting and responding to issues as they arise.

---

[15] For example, there are plans to validate the complete rover in CHARM before its first mission.

[16] For example, in the CHARM experiment, a high-precision temperature sensor would have been highly beneficial for thermal monitoring. Furthermore, placing a current-voltage sensor in closer proximity to the setup could have been used to monitor various signals on the mainboard, such as the four standby lines, which would help trace the origins of different SEEs. In addition, those sensors would also allow for monitoring of power consumption before it is attenuated over the transmission lines.

5

Conclusion

This thesis set out to evaluate the state-of-the-art radiation payload of the Lunar Zebro to determine its readiness for the first lunar mission. To achieve this, three radiation campaigns were conducted alongside a series of functionality tests.

Proton Experiment at HollandPTC

The initial experiment aimed to validate previous findings and familiarize with the sensor's behaviour. The results indicated a lower sensitivity than reported by Sealicon[4], but they aligned with prior research by Meyere et al.[1] and Shanbhag et al. [2]. Additionally, a high level of outliers (shifts and jumps) was observed during the operation. By applying both selective and numerical filtering, it was possible to extract a sensitivity curve and independent correlation between the proton flux and sensor sensitivity.

Gamma Irradiation at Reactor Institute Delft

A second campaign was conducted at RID using a very low flux gamma source to simulate the dose rate reported by the LND (13.1 $\mu Gy/h$). The results showed that temperature compensation is crucial for accurate dose rate estimations. Additionally, due to the observed low sensitivity of the sensor, long-duration measurements are required to achieve statistical significance. Given the intended mission goal of measuring radiation at different lunar topographical features (e.g., inside caves, behind rocks), the low dose rate and sensor sensitivity pose a challenge. Combined with potential voltage and temperature fluctuations during the mission, these factors introduce additional uncertainties that must be carefully accounted for.

Mixed-Field Experiment at CERN CHARM

The third campaign tested the radiation payload in a mixed-field environment, providing valuable insights before system-level testing with both the payload and the rover. Initial exposure results showed sensor sensitivity values consistent with Zimmaro et al. [3] and Sealicon datasheet[4]. In addition, a sensitivity curve across the full FG range was possible to be established for one of the sensors. However, due to significant fluctuations in various observables, it was not possible to conclusively determine the maximum sensitivity as a function of the total ionizing dose for the remainder of the dataset. For this, additional data processing is required to obtain conclusive results in this regime.

A major issue observed during this experiment was that none of the FGDOS sensors automatically recharged as expected. Further investigation revealed a firmware bug that caused continuous recharging beyond the target point. Discussions with the manufacturer confirmed that the settings were correctly configured, but the root cause of the issue remains unidentified. Additionally, they suggested that the sensors may require a manual "kickstart" to initiate the recharging process for the first few times. This, coupled with a SEE (Single Event Effect) event that triggered an unexpected recharge, raises concerns. If left unattended, the firmware's inability to react appropriately could cause the sensor to operate outside its linear dynamic range, potentially compromising the mission. Furthermore, when combined with manual discharge tests, which showed the sensor stalling after approximately 30 kHz, this could result in an undesirable operational scenario for the scientific mission.

The CHARM experiment also revealed higher-than-expected power consumption compared to Shanbhag [2]. Notably, Setup 1 exhibited an unusually high power draw from the start of the experiment and ultimately lost communication at 85.0 Gy. Without a post-mortem analysis of the system, it is impossible to determine the root cause or its implications for future radiation payload designs.

6

Recommendations for Future work

While this study has provided insight into the operation of the Floating Gate Dosimeter and evaluated its suitability for a lunar environment, several areas require further investigation. As the following recommendations span multiple disciplines, they are presented separately, with a focus on those that can be pursued within TU Delft. Firstly, the discussion will focus on improvements to the floating gate technology. Secondly, recommendations for enhancements to the radiation payload will be presented. Finally, potential long-term research avenues related to the Timepix detector will be explored.

6.0.1. R&D on the floating gate dosimeter

It was observed that the Floating Gate Dosimeter (FGDOS) is capable of detecting radiation in various environments. However, these sensors are not individually capable of decomposing a mixed radiation field. This, coupled with the reported sensitivity degradation [3] and our observations of the response to low fluxes (see chapter 3), limits the potential of the FGDOS to yield significant scientific results.

Research has been conducted to address these limitations. For example, Rizzo et al. [74] applied an external field to enhance the electric field in the silicon dioxide, thereby increasing the device's sensitivity and reducing the sensitivity degradation. Similarly, Brucoli et al. [73] explored a modified FGDOS that allows for measuring the charge yield of different ions and assessing the impact of impinging particles with varying LETs in a mixed radiation field environment.

Nevertheless, from a university research perspective, it may be valuable to move beyond purely investigating commercial of the shelf (COTS) devices and engage in R&D efforts on the FGDOS. Three potential research avenues are proposed: scaling, material addition, and stacking. These concepts are illustrated in Figure 6.1.

Firstly, as observed in chapter 3, if the same dose rate outlined by the LND is to be measured while distinguishing relevant observations within a single Lunar day, the sensitivity must be increased to reduce the required measurement time for a particular event. Referring to the equation in section 2.5, the most straightforward approach is to increase the sensor's surface area, allowing more particles to generate carriers that reach the floating gate (FG).

Secondly, an alternative method involves incorporating a material with a high neutron cross-section, which would enable neutron capture and conversion into secondary particles (e.g., gamma rays or alpha particles) that, in turn, create electron-hole pairs in the oxide. This material should be positioned as close as possible to the oxide to maximize charge carrier generation while minimizing absorption in other materials. This technique could be particularly useful for planetary exploration, as neutrons - due to their 15-minute lifetime [98, 99]- are absent in cosmic rays or solar winds. Any neutron found near a planetary body has been produced by cosmic-ray spallation of planetary matter and thereby carries signatures of its birthplace. A properly designed detector could distinguish between thermal and epithermal neutrons.[1] Such a capability is particularly relevant for human lunar exploration, as the

---

[1] Possibly achieved using two different sensors, one more optimised for thermal neutrons and the other for epithermal neutrons

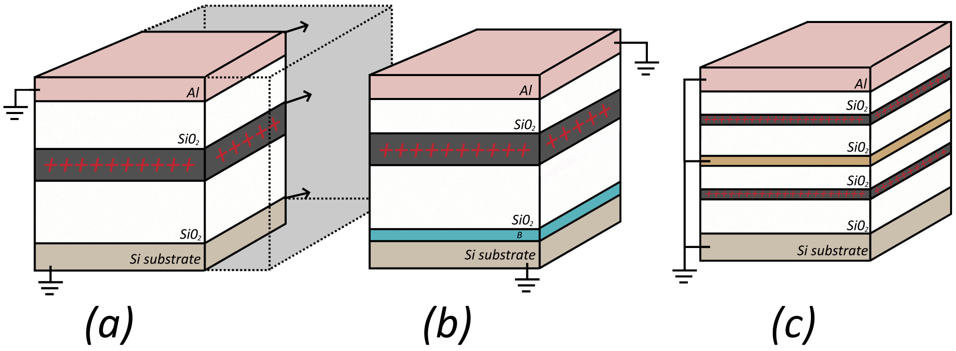

Figure 6.1: Three schematic representations of the Floating Gate Dosimeter, each illustrating a potential research avenue: (A) Increasing the sensor area to allow for the detection of a greater number of particles. (B) Incorporating materials with a high neutron cross-section, such as boron, to enhance neutron sensitivity. (C) Implementing multiple floating gates to enable monitoring of the Linear Energy Transfer (LET) of different particle species.

presence of epithermal-to-thermal neutron ratios serves as a strong indicator of nearby water deposits—a crucial resource for sustaining long-term lunar missions[48, 100, 101, 102].

The third technique follows the similar principles used in multi-junction solar cells[103] and $\Delta E - E$ detectors[19, 104, 105]. Both rely on the fact that a given type of particle with specific energy exhibits a certain energy loss as it traverses a material. By exploiting this principle and stacking multiple floating gates on top of each other, it may be possible to infer the linear energy transfer (LET) of particles and/or determine the fraction of a mixed field associated with different particle types.

However, all the above-mentioned techniques may be challenging to implement due to limitations inherent to CMOS technology. Additionally, unintended effects such as increased noise, dose rate dependency, directionality sensitivity, and energy dependence may arise, which could be undesirable depending on the design constraints.

6.0.2. Lunar Zebro radiation payload

The current design of the radiation payload has been primarily tested for radiation exposure, and its characteristics have been demonstrated. However, before it is flight-ready, environmental testing in combination with the rover must be conducted. Below a brief overview of different test for the current state-of-the-art payload are mentioned.

Radiation Hardness Assurance testing with the lunar rover

> The payload has already undergone several tests, but integrating it with the rover for testing in the CHARM facility would provide valuable system-level validation. This would allow for the assessment of interactions between the payload and the rover's subsystems, and ensure that the combined system can operate reliably in a mixed-field radiation environment. However, if this is not possible, tests conducted in a Cobalt-60 facility would still provide valuable data.

Mechanical loads: Vibration and Shock Testing

> To verify that the payload can withstand structural loads caused by launch, operation, and deployment, testing will likely be conducted at the system level at Royal NLR.

Thermal-Vacuum (TVAC) Test

> The payload should undergo testing for vacuum exposure to ensure functionality in space-like conditions. Additionally, its integrity under extreme temperatures and thermal cycling should be further characterised to evaluate its performance and reliability in varying thermal environments. This would expand upon the tests previously conducted by Shanbhag et al. [2, see Chapter 5.3 & 5.7.3].

A Radiation Payload Operations Manual

A manual needs to be drafted that documents and communicates the design and behavior of the Radiation Payload.

Future development on the Radiation payload

Exploring the addition of an SRAM to the payload, similar to what has been implemented in CERN's Space RadMon-NG payload for the CELESTA CubeSat [106], could provide valuable insights into characterizing the radiation environment. SRAM is a volatile memory bank that loses its stored data when unpowered, making it useful for radiation characterization by detecting single-event upsets (SEU) and single-event latchups (SEL). Research in this field is extensive, as outlined by Coronetti et al. [106]. Additionally, studies have investigated the thermal neutron sensitivity of SRAM-based detectors [107], highlighting their potential for thermal neutron monitoring in space environments. A detailed explanation of SRAM implementation for radiation measurements can also be found in Dijks et al. [75].

In addition, when future engineering and development boards are created, the recommendations outlined in section 4.8 could be implemented. Furthermore, if size restrictions allow, the addition of LEDs on the PCB would be extremely useful for debugging the system. Even though LEDs may not be functional in space, their benefits during development and testing remain significant. Secondly, the current board layout includes traces close to the mounting holes (e.g., near C16 on the mainboard), which could potentially cause a short circuit. Addressing this issue would improve reliability. Additionally, a review of the capacitor placement could be beneficial, as DEMO [2] has recommended replacing large capacitors with multiple smaller capacitors placed in parallel for improved performance.

Finally, the recommendations from Shanbhag et al. [2, see Chapter 7.1] could also be incorporated into future iterations of the design.

Data processing

The CHARM experiment proved to be a valuable trial run for the eventual mission. For example, during the second radiation week, Setup 2 transmitted approximately 274,000 data packets, each containing information from the four sensors. This excludes any diagnostic triggers sent during the experiment. During this thesis, data files were saved in ”Comma Separated Values” (CSV) format every X hours. Afterward, the data was filtered and processed into a single CSV data file ($\sim$40 MB) along with a logbook file. Further data treatment was then applied to obtain the results presented in section 4.6. For future iterations, it may be advisable to explore the use of HDF5 file formatting instead of CSV. This would allow data to be organized into structured groups, with each group containing relevant metadata, improving data accessibility and post-processing efficiency.

Manually discharge the FGDOS

During testing of the FGDOS, it was found that manual discharging of the floating gate would stagnate after around 30 kHz. For this reason, it would be beneficial to extend these tests and include the findings in the operation manual to improve understanding and future use.

Firmware

The current firmware is developed using the Energia IDE[3] for the MSP430 microcontroller. The firmware version used in this thesis is an R&D version, which is not user-friendly, same for the Energia IDE. Personal experience showed that using Visual Studio Code significantly improved workflow. The firmware could benefit from increased flexibility and modularity, as well as improvements in readability and organization. At the time of writing, the Lunar Zebro embedded systems team was working on implementing improvements in this area but had not yet made significant progress.

CHARM setup post-CHARM diagnostic

---

[2] https://www.tudelft.nl/demo

[3] Energia IDE is an open-source development environment based on the Wiring and Arduino IDE, designed for Texas Instruments (TI) microcontrollers[108]

As outlined in section 4.7, the current thesis timeline did not allow for a comprehensive post-analysis of the CHARM setup or further investigation into what was referred to as ”recovery time” in section 4.6, as well as the sensitivity calculations during the second week in Appendix J. All these aspects need to be further examined before making additional recommendations for future iterations of the payload.

Future irradiation on the FGDOS

As outlined in section 3.4, further investigation is needed to overlap the results obtained from the low-flux gamma experiments at Reactor Institute Delft (RID), HollandPTC and CHARM CERN. For this, experiments at ESA ESTEC could be conducted to establish a direct comparison. Although RID has high-flux gamma sources, they are not housed in a facility optimised for this type of radiation testing.

- Additionally, dedicated neutron irradiation would be valuable, particularly to support the findings in Figure 4.18, which suggest an increase in sensitivity due to neutron exposure. For this, the Neutron Depth Profiler (NDP) at RID could be used to further investigate this effect.

6.0.3. Space Radiation Environment Simulations

Previous simulation work by Shanbhag et al. [2][4] provided initial findings using SPENVIS and Geant4 for the Lunar Zebro mission. However, a comprehensive investigation of the radiation environment is needed to fully understand the surroundings and prepare for future system-level testing.

6.0.4. Timepix as a future payload detector

The search for more powerful scientific instruments for the Lunar Zebro rover is an ongoing endeavor. The current radiation payload design is constrained by the rover system limitations, preventing the integration of more advanced detectors such as Timepix. In the near future, these constraints are unlikely to change. However, in the long term, this may be different, as a swarm of rovers operating on the lunar surface and other extraterrestrial environments is envisioned. In such a scenario, a more powerful rover could maybe support the necessary infrastructure to accommodate the Timepix detector.

An introduction to this detector is provided in Appendix G; however, several open questions remain regarding the underlying constraints of integrating this detector into a nano-rover like Lunar Zebro. These questions and challenges are also outlined in this appendix.

6.0.5. Final thoughts and Next steps

The outlined recommendations present multiple paths forward, containing both short-term objectives and long-term developments. Priority should be given to immediate goals, such as investigating modifications to the FGDOS to enhance its neutron sensitivity. In parallel, conducting more experiments on the FGDOS will provide essential insights and validation. Finally, simulating the space radiation environment is essential to better understand its characteristics and impact, further reducing uncertainties and guiding future developments.

---

[4] See Chapter 4, Section 6.2, and Section 7.2 for further details.

References

[1] W.M.H De Meyere. *Characterisation of a Floating Gate Dosimeter for Space Applications*. Tudelft.nl, 2022. URL: https://repository.tudelft.nl/record/uuid:1fe2f17a-a6e6-48e5-bcf5-af0b32b7471e#files (visited on 12/17/2024).

[2] Abhimanyu Shanbhag. “REDMOON: Radiation Environment and Dose Monitoring On-board a Nano-Rover”. PhD thesis. Nov. 2022. URL: https://repository.tudelft.nl/islandora/object/uuid%3Ad1814d56-3e59-4cea-bbf3-fd150a093ee2.

[3] Alessandro Zimmaro et al. “Testing and validation methodology for a radiation monitoring system for electronics in particle accelerators”. In: *IEEE Transactions on Nuclear Science* 69.7 (2022), pp. 1642–1650. DOI: 10.1109/TNS.2022.3158527.

[4] Sealicon Micro. *FGD-03F Floating Gate Dosimeter (FGDOS ®)*. Sealiconmicro, May 2020. URL: https://www.sealiconmicro.com/products/pdf/datasheet-fgd-03f-3-47455.pdf (visited on 12/08/2024).

[5] NASA. *NASA’s Plan for Sustained Lunar Exploration and Development NASA’s Plan for Sustained Lunar Exploration and Development*. URL: https://www.nasa.gov/wp-content/uploads/2020/08/a_sustained_lunar_presence_nspc_report4220final.pdf (visited on 02/15/2025).

[6] NASA. *NASA’s Lunar Exploration Program Overview*. 2020. URL: https://www.nasa.gov/wp-content/uploads/2020/12/artemis_plan-20200921.pdf (visited on 02/18/2025).

[7] Jeffery Chancellor, Graham Scott, and Jeffrey Sutton. “Space Radiation: the Number One Risk to Astronaut Health beyond Low Earth Orbit”. In: *Life* 4 (Sept. 2014), pp. 491–510. DOI: 10.3390/life4030491. URL: https://www.mdpi.com/2075-1729/4/3/491/htm (visited on 11/25/2019).

[8] Anna Fogtman et al. “Towards sustainable human space exploration—priorities for radiation research to quantify and mitigate radiation risks”. In: *npj Microgravity* 9 (2023), p. 8. DOI: 10.1038/s41526023002627. URL: https://doi.org/10.1038/s41526023002627.

[9] Bilal Bomani. *CubeSat Technology past and Present: Current State-of-the-Art Survey*. 2021. URL: https://ntrs.nasa.gov/api/citations/20210000201/downloads/TP-20210000201.pdf (visited on 12/06/2024).

[10] Evgenya L Shkolnik. “On the verge of an astronomy CubeSat revolution”. In: *Nature Astronomy* 2 (2018), pp. 374–378. DOI: 10.1038/s4155001804388. URL: https://doi.org/10.1038/s4155001804388.

[11] NASA. *Commercial CubeRover Test Shows How NASA Investments Mature Space Tech - NASA*. NASA.gov, Dec. 2020. URL: https://www.nasa.gov/missions/artemis/clps/commercial-cuberover-test-shows-how-nasa-investments-mature-space-tech/.

[12] *Lunar Zebro | Nano Rover TU Delft*. Zebro.space, 2024. URL: https://zebro.space/.

[13] Asri El Ghali and Zheng H Zhu. “An introductory review of swarm technology for spacecraft on-orbit servicing”. In: *International Journal of Mechanical System Dynamics* 4.1 (2024), pp. 3–21. DOI: https://doi.org/10.1002/msd2.12098. URL: https://onlinelibrary.wiley.com/doi/abs/10.1002/msd2.12098.

[14] James R Schwank et al. “Radiation effects in MOS oxides”. In: *IEEE Transactions on Nuclear Science* 55.4 (2008), pp. 1833–1853. DOI: 10.1109/TNS.2008.2001040.

[15] T.P. Dachev et al. “An overview of RADOM results for earth and moon radiation environment on Chandrayaan-1 satellite”. In: *Advances in Space Research* 48.5 (2011), pp. 779–791. DOI: https://doi.org/10.1016/j.asr.2011.05.009. URL: https://www.sciencedirect.com/science/article/pii/S0273117711003218.

[16] Shenyi Zhang et al. “First measurements of the radiation dose on the lunar surface”. In: *Science Advances* 6.39 (2020), eaaz1334. DOI: 10.1126/sciadv.aaz1334. URL: https://www.science.org/doi/abs/10.1126/sciadv.aaz1334.

[17] Mazur J E et al. “New measurements of total ionizing dose in the lunar environment”. In: *Space Weather* 9.7 (2011). DOI: https://doi.org/10.1029/2010SW000641. URL: https://agupubs.onlinelibrary.wiley.com/doi/abs/10.1029/2010SW000641.

[18] Harlan E Spence et al. “Relative Contributions of Galactic Cosmic Rays and Lunar Proton “albedo” to Dose and Dose Rates near the Moon”. In: *Space Weather* 11.11 (Nov. 2013), pp. 643–650. DOI: 10.1002/2013SW000995.

[19] Glenn F Knoll. *Radiation detection and measurement*. 4th ed. Wiley, 2010.

[20] Lars P van Roobol. *Practical radiation protection*. Fourth, completely revised edition. Syntax Media, 2018.

[21] Andrew Holmes-Siedle and Len Adams. *Handbook of radiation effects*. Oxford University Press, Jan. 2002. DOI: 10.1093/oso/9780198507338.001.0001. URL: https://doi.org/10.1093/oso/9780198507338.001.0001.

[22] Richard Jung. “Radiation qualification of the cologne chip GateMate A1 FPGA”. PhD thesis. 2023, p. 118. DOI: 10.26205/opus-3364.

[23] Ygor Q. de Aguiar et al. *Single-Event Effects, from Space to Accelerator Environments : Analysis, Prediction and Hardening by Design*. Springer International Publishing, 2025, pp. 29–47. DOI: 10.1007/978-3-031-71723-9 . URL: https://doi.org/10.1007/978-3-031-71723-9%E2%82%82 (visited on 02/01/2025).

[24] ESA-ESTEC Requirements Standards Division ECSS Secretariat. *ECSS-Q-ST-60-15C – Radiation hardness assurance – EEE components (1 October 2012) | European Cooperation for Space Standardization*. Ecss.nl, Oct. 2012. URL: https://ecss.nl/standard/ecss-q-st-60-15c-radiation-hardness-assurance-eee-components-1-october-2012/ (visited on 12/17/2024).

[25] ESA Requirements ECSS and Standards Division. *ECSS-E-ST-10-12C – Methods for the calculation of radiation received and its effects, and a policy for design margins (15 November 2008) +Corr.1 (22Feb2017) | European Cooperation for Space Standardization*. ecss.nl, Nov. 2008. URL: https://ecss.nl/standard/ecss-e-st-10-12c-methods-for-the-calculation-of-radiation-received-and-its-effects-and-a-policy-for-design-margins/ (visited on 05/28/2024).

[26] Muhammad Sajid et al. “Analysis of total ionizing dose effects for highly scaled CMOS devices in low earth orbit”. In: *Nuclear Instruments and Methods in Physics Research Section B: Beam Interactions with Materials and Atoms* 428 (2018), pp. 30–37. DOI: https://doi.org/10.1016/j.nimb.2018.05.014. URL: https://www.sciencedirect.com/science/article/pii/S0168583X18303215.

[27] R Baumann. “Soft Errors in Commercial Integrated Circuits”. In: *International Journal of High Speed Electronics and Systems* 14 (Nov. 2011). DOI: 10.1142/S0129156404002363.

[28] R.C Baumann. “Radiation-induced Soft Errors in Advanced Semiconductor Technologies”. In: *IEEE Transactions on Device and Materials Reliability* 5.3 (2005), pp. 305–316. DOI: 10.1109/TDMR.2005.853449.

[29] J R Srour and J W Palko. “Displacement Damage Effects in Irradiated Semiconductor Devices”. In: *IEEE Transactions on Nuclear Science* 60 (July 2013), pp. 1740–1766. DOI: 10.1109/TNS.2013.2261316.

[30] C. Inguimbert and S Messenger. “Equivalent Displacement Damage Dose for OnOrbit Space Applications”. In: *IEEE Transactions on Nuclear Science* 59 (Dec. 2012), pp. 3117–3125. DOI: 10.1109/TNS.2012.2221477.

[31] James W Cronin. “Cosmic rays: the most energetic particles in the universe”. In: *Rev. Mod. Phys.* 71 (1999), S165–S172. DOI: 10.1103/RevModPhys.71.S165. URL: https://link.aps.org/doi/10.1103/RevModPhys.71.S165.

[32] Markus J Aschwanden. *New millennium solar physics*. 2019. DOI: 10.1007/978303013. URL: https://search.ebscohost.com/login.aspx?direct=true&scope=site&db=nlebk&db=nlabk&AN=2143394.

[33] Marco Durante and Francis A Cucinotta. “Physical basis of radiation protection in space travel”. In: *Rev. Mod. Phys.* 83 (2011), pp. 1245–1281. DOI: 10.1103/RevModPhys.83.1245. URL: https://link.aps.org/doi/10.1103/RevModPhys.83.1245.

[34] National Oceanic and Atmospheric Administration (NOAA). *Solar Cycle Progression | NOAA / NWS Space Weather Prediction Center*. www.swpc.noaa.gov. URL: https://www.swpc.noaa.gov/products/solar-cycle-progression (visited on 03/01/2025).

[35] J Feynman et al. “Solar proton events during solar cycles 19, 20, and 21”. In: *Solar Physics* 126 (1990), pp. 385–401. DOI: 10.1007/BF00153058. URL: https://doi.org/10.1007/BF00153058.

[36] William Lowrie and Andreas Fichtner. “The Earth’s Magnetic Field”. In: 3rd ed. Fundamentals of Geophysics. Cambridge University Press, 2020, p. 317355. DOI: DOI:10.1017/9781108685917.012. URL: https://www.cambridge.org/core/product/8DFE921472B6739F1701DF0EEF58FBF3.

[37] J.A van Allen et al. “Observation of High Intensity Radiation by Satellites 1958 Alpha and Gamma | Journal of Jet Propulsion”. In: *Journal of Jet Propulsion* (2024). DOI: 10.2514/jjp.1958.28.issue-9;wgroup:string:AIAA. URL: https://arc.aiaa.org/doi/10.2514/8.7396 (visited on 12/20/2024).

[38] YuXuan Li et al. “Dynamics of the inner electron radiation belt: A review”. In: *Earth and Planetary Physics* 7 (Nov. 2022), pp. 109–118. DOI: 10.26464/epp2023009. (Visited on 12/20/2024).

[39] Vincent L Pisacane. *The space environment and its effects on space systems*. American Institute of Aeronautics and Astronautics ; [Eurospan [distributor], 2008.

[40] Riccardo Campana. “In-orbit Background for x-ray Detectors”. In: ed. by Cosimo Bambi and Andrea Santangelo. Handbook of X-ray and Gamma-ray Astrophysics. Springer Nature Singapore, 2024, pp. 919–945. DOI: 10.1007/978-981-19-6960-7 8. URL: https://doi.org/10.1007/978-981-19-6960-7%E2%82%828 (visited on 12/06/2024).

[41] I A Grenier, J H Black, and A W Strong. “The Nine Lives of Cosmic Rays in Galaxies”. In: *the Annual Review of Astronomy and Astrophysics* 53 (Aug. 2015), pp. 199–246. DOI: 10.1146/annurev-astro-082214-122457.

[42] Guenther Reitz. “Characteristic of the radiation field in low earth orbit and in deep space”. In: *Zeitschrift für Medizinische Physik* 18.4 (2008), pp. 233–243. DOI: https://doi.org/10.1016/j.zemedi.2008.06.015. URL: https://www.sciencedirect.com/science/article/pii/S0939388908000792.

[43] S. Navas et al. “Review of particle physics”. In: *Phys. Rev. D* 110.3 (2024), p. 030001. DOI: 10.1103/PhysRevD.110.030001.

[44] Mikhail I Dobynde and Jingnan Guo. “Radiation Environment at the Surface and Subsurface of the Moon: Model Development and Validation”. In: *Journal of Geophysical Research: Planets* 126 (Nov. 2021). DOI: 10.1029/2021je006930.

[45] Schwadron N A et al. “Lunar radiation environment and space weathering from the Cosmic Ray Telescope for the Effects of Radiation (CRaTER)”. In: *Journal of Geophysical Research: Planets* 117.E12 (2012). DOI: https://doi.org/10.1029/2011JE003978. URL: https://agupubs.onlinelibrary.wiley.com/doi/abs/10.1029/2011JE003978.

[46] Richard Vondrak et al. “Lunar Reconnaissance Orbiter (LRO): Observations for Lunar Exploration and Science”. In: *Space Science Reviews* 150 (2010), pp. 7–22. DOI: 10.1007/s1121401096315. URL: https://doi.org/10.1007/s1121401096315.

[47] Mazur J E et al. “Update on radiation dose from galactic and solar protons at the moon using the LRO/CRaTER microdosimeter”. In: *Space Weather* 13.6 (2015), pp. 363–364. DOI: https://doi.org/10.1002/2015SW001175. URL: https://agupubs.onlinelibrary.wiley.com/doi/abs/10.1002/2015SW001175.

[48] Robert F WimmerSchweingruber et al. “The Lunar Lander Neutron and Dosimetry (LND) Experiment on Chang’E 4”. In: *Space Science Reviews* 216 (2020), p. 104. DOI: 10.1007/s11214020007253. URL: https://doi.org/10.1007/s11214020007253.

[49] Daniel Matthiä and Thomas Berger. “The Radiation Environment on the Surface of Mars – Numerical Calculations of the Galactic Component with GEANT4/PLANETOCOSMICS”. In: *Life Sciences in Space Research* 14 (2017), pp. 57–63. DOI: https://doi.org/10.1016/j.lssr.2017.03.005. URL: https://www.sciencedirect.com/science/article/pii/S2214552417300081.

[50] M. D. Looper et al. “The radiation environment near the lunar surface: CRaTER observations and Geant4 simulations”. In: *Space Weather* 11 (Apr. 2013), pp. 142–152. DOI: 10.1002/swe.20034.

[51] K.V Sharma. *Adaptation Study of Zebro as Nano Rover for Lunar Exploration and Demonstration of Locomotion on Simulated Lunar Surface*. Tudelft.nl, 2018. URL: https://repository.tudelft.nl/record/uuid%3A46e4b4c9-c2c0-47cb-8ef5-c206844a7f83 (visited on 12/06/2024).

[52] *Moon Mission | Lunar Zebro*. Lunar zebro, 2019. URL: https://zebro.space/missions/moon_mission/ (visited on 04/24/2024).

[53] Jason James. *Detailed design document*. Feb. 2021.

[54] Muñoz Tejeda et al. *Environmental analysis of nanorovers in a swarm for lunar scientific missions*. TU Delft Research Portal, 2019. URL: https://research.tudelft.nl/en/publications/environmental-analysis-of-nanorovers-in-a-swarm-for-lunar-scienti (visited on 12/06/2024).

[55] Danny Gasman. *Payload Concept Design*. July 2019.

[56] Danny Gasman. *Phase B: Payload (5600)*. 2021.

[57] E Garcia-Moreno et al. “Floating gate CMOS dosimeter with frequency output”. In: *IEEE Transactions on Nuclear Science* 59.2 (2012), pp. 373–378. DOI: 10.1109/TNS.2012.2184301.

[58] S Danzeca et al. “Characterization and modeling of a floating gate dosimeter with gamma and protons at various energies”. In: *IEEE Transactions on Nuclear Science* 61.6 (2014), pp. 3451–3457. DOI: 10.1109/TNS.2014.2364274.

[59] Youngbin Jin, Ben Lee, and Ali R Hurson. “Chapter One: a Comprehensive Survey of Issues in Solid State Drives”. In: vol. 114. Advances in Computers. Elsevier, 2019, pp. 1–69. DOI: https://doi.org/10.1016/bs.adcom.2019.02.001. URL: https://www.sciencedirect.com/science/article/pii/S0065245819300117.

[60] Matteo Brucoli. “Total Ionizing Dose Monitoring for Mixed Field Environments”. In: *Hal.science* (Nov. 2018). DOI: https://theses.hal.science/tel-02155482. URL: https://theses.hal.science/tel-02155482 (visited on 12/23/2024).

[61] M.R Shaneyfelt et al. “Charge Yield for cobalt-60 and 10-keV X-ray Irradiations of MOS Devices”. In: *IEEE Transactions on Nuclear Science* 38.6 (1991), pp. 1187–1194. DOI: 10.1109/23.124092.

[62] M.N Martin et al. “FGMOS dosimetry: design and implementation”. In: *IEEE Transactions on Nuclear Science* 48.6 (2001), pp. 2050–2055. DOI: 10.1109/23.983171.

[63] N.G Tarr et al. “A sensitive, temperature-compensated, zero-bias Floating Gate MOSFET Dosimeter”. In: *IEEE Transactions on Nuclear Science* 51.3 (2004), pp. 1277–1282. DOI: 10.1109/TNS.2004.829372.

[64] Federico Ravotti. “Dosimetry Techniques and Radiation Test Facilities for Total Ionizing Dose Testing”. In: *IEEE Transactions on Nuclear Science* 65.8 (2018), pp. 1440–1464. DOI: 10.1109/TNS.2018.2829864.

[65] Sealicon. *Radiation products*. Sealicon microsystems, 2024. URL: https://www.sealiconmicro.com/sealicon-products-5/radiation (visited on 12/23/2024).

[66] E Garcia-Moreno et al. “Temperature Compensated Floating Gate MOS Radiation Sensor with Current Output”. In: *IEEE Transactions on Nuclear Science* 60.5 (2013), pp. 4026–4030. DOI: 10.1109/TNS.2013.2277605.

[67] Maite Álvarez et al. “Total ionizing dose characterization of a prototype floating gate MOSFET dosimeter for space applications”. In: *IEEE Transactions on Nuclear Science* 60.6 (2013), pp. 4281–4288. DOI: 10.1109/TNS.2013.2288573.

[68] *Floating Gate p-mos Radiation Sensor Charging Cycles Characterization*. 2014 IEEE Radiation Effects Data Workshop (REDW). IEEE, 2014, pp. 1–4. DOI: 10.1109/REDW.2014.7004572.

[69] *Floating gate dosimeter measurements at 4M lunar flyby mission*. 2015, pp. 1–4. DOI: 10.1109/REDW.2015.7336710.

[70] *A Complete Qualification of Floating Gate Dosimeter for CERN Applications*. RADECS 16th. 2016, pp. 1–4. DOI: 10.1109/RADECS.2016.8093162.

[71] *Study of Floating Gate MOS Structures to Improve the Noise and Sensitivity as Radiation Dosimeter*. Radecs 2017. 2017, pp. 1–4. DOI: 10.1109/RADECS.2017.8696254.

[72] M Brucoli et al. “Floating Gate Dosimeter Suitability for accelerator-like Environments”. In: *IEEE Transactions on Nuclear Science* 64.8 (2017), pp. 2054–2060. DOI: 10.1109/TNS.2017.2681651.

[73] *Heavy-ion charge yield measurement by floating gate dosimeters*. 2021, pp. 1–4. DOI: 10.1109/RADECS53308.2021.9954559.

[74] Marta Rizzo et al. “An enhanced sensitivity operation mode for floating gate dosimeters”. In: *IEEE Transactions on Nuclear Science* 69.8 (2022), pp. 1876–1883. DOI: 10.1109/TNS.2022.3185397.

[75] J.H.C Dijks. *Precise LEO Space Radiation Monitoring Using the Space RadMon-NG Payload*. Tudelft.nl, 2023. URL: https://repository.tudelft.nl/record/uuid:70bdbfdc-28be-40b5-864e-92798b910449 (visited on 08/26/2024).

[76] *MOS devices and integrated circuits for ionizing radiation dosimetry: a review*. 2020 Argentine Conference on Electronics (CAE). 2020, pp. 31–40. DOI: 10.1109/CAE48787.2020.9046369.

[77] Simone Gerardin and Alessandro Paccagnella. “Present and future non-volatile memories for space”. In: *IEEE Transactions on Nuclear Science* 57.6 (2010), pp. 3016–3039. DOI: 10.1109/TNS.2010.2084101.

[78] Sajid Ahmad, Raheel Hammad, and Seemin Rubab. “Gamma RadiationInduced Synthesis of PolyanilineBased Nanoparticles/Nanocomposites”. In: *Journal of Electronic Materials* 51 (2022), pp. 5550–5567. DOI: 10.1007/s11664022098230. URL: https://doi.org/10.1007/s11664022098230.

[79] Kevin B Lavelle et al. “A reference material for evaluation of 137Cs radiochronometric measurements”. In: *Journal of Radioanalytical and Nuclear Chemistry* 318 (2018), pp. 195–208. DOI: 10.1007/s1096701860614. URL: https://doi.org/10.1007/s1096701860614.

[80] NIST. *Radionuclide Half-Life Measurements*. NIST, July 2009. URL: https://www.nist.gov/pml/radiation-physics/radioactivity/radionuclide-half-life-measurements.

[81] ECSS. *Specification (22900) Total Dose Steady-State Irradiation Test Method*. Spacecomponents.org, 2016. URL: https://spacecomponents.org/specification/view?id=3413 (visited on 09/26/2024).

[82] Malcolm R. McEwen and Jaswinder Taank. “Examining the Influence of Humidity on Reference Ionization Chamber Performance”. In: *Medical Physics* 44 (Jan. 2017), pp. 694–702. DOI: 10.1002/mp.12057. (Visited on 11/22/2022).

[83] IAEA. *Absorbed Dose Determination in External Beam Radiotherapy*. TRS-398. 398 (Rev. 1). INTERNATIONAL ATOMIC ENERGY AGENCY, Dec. 2000. URL: https://www.iaea.org/publications/15048/absorbed-dose-determination-in-external-beam-radiotherapy (visited on 11/21/2024).

[84] GREISINGER electronic GmbH. *GFTB 200 Operating Manual Precision Hygro-/Thermo-/Barometer with Alarm Function*. URL: https://asset.conrad.com/media10/add/160267/c1/-/en/000649961ML03/gebruiksaanwijzingen-en-veiligheidsinformatie-649961-greisinger-gftb-200-luchtvochtigheidsmeter-hygrometer-0-hrel-100-hrel-dauwpuntschimmel-waarschuwingsweergave.pdf (visited on 12/05/2025).

[85] DELTA ELEKTRONIKA B.V. *EST 150 -Series 150W Triple Output DC POWER SUPPLIES*. URL: https://www.delta-elektronika.nl/sites/default/files/2025-01/EST150_DTS_V202501.pdf (visited on 12/01/2024).

[86] Rudy Ferraro. "Development of test methods for the qualification of electronic components and systems adapted to high-energy accelerator radiation environments". PhD thesis. Dec. 2019. URL: https://theses.hal.science/tel-02879667.

[87] William De Meyere, Abhimanyu Shanbhag, and Alessandra Menicucci. "Floating gate dosimeter characterization for space applications". In: *IEEE Transactions on Nuclear Science* (2024), pp. 1–1. DOI: 10.1109/TNS.2024.3373748.

[88] European Space components coordination (ESCC). *Co-60 Info | ESCIES (European Space Components Information Exchange System)*. Escies.org, 2021. URL: https://escies.org/webdocument/showArticle?id=251&groupid=6 (visited on 02/05/2025).

[89] Thomas Toets. *Personal Communication about HollandPTC Dose Rate*. Jan. 2025.

[90] Julien Mekki et al. "CHARM: A Mixed Field Facility at CERN for Radiation Tests in Ground, Atmospheric, Space and Accelerator Representative Environments". In: *IEEE Transactions on Nuclear Science* 63 (Aug. 2016), pp. 2106–2114. DOI: 10.1109/tns.2016.2528289. (Visited on 10/10/2023).

[91] Johannes Bernhard et al. "CERN Proton Synchrotron East Area Facility Upgrades and renovation during Long Shutdown 2 Editors". In: 4 (Dec. 2021). DOI: 10.23731/CYRM-2021-004. URL: https://cds.cern.ch/record/2792490/files/145-137-PB.pdf.

[92] *The CERN high energy accelerator mixed field (CHARM) facility in the CERN PS east experimental area*. 2015, pp. 14–25.

[93] A Thornton. *CHARM Facility Test Area Radiation Field Description*. 2016. URL: https://cds.cern.ch/record/2149417/files/CHARM%20Facility%20Test%20Area%20Radiation%20Field%20Description.pdf.

[94] Andrew Holmes-Siedle and Leonard Adams. "RADFET: A review of the use of metal-oxide-silicon devices as integrating dosimeters". In: *International Journal of Radiation Applications and Instrumentation. Part C. Radiation Physics and Chemistry* 28.2 (1986), pp. 235–244. DOI: https://doi.org/10.1016/1359-0197(86)90134-7. URL: https://www.sciencedirect.com/science/article/pii/1359019786901347.

[95] *CHARM | r2e.web.cern.ch*. Cern.ch, 2018. URL: https://r2e.web.cern.ch/about-radiation/test-facilities/charm (visited on 12/09/2024).

[96] R.L. Pease, A.H. Johnston, and J.L. Azarewicz. "Radiation testing of semiconductor devices for space electronics". In: *Proceedings of the IEEE* 76 (1988), pp. 1510–1526. DOI: 10.1109/5.90110. (Visited on 01/31/2020).

[97] Salvatore Fiore. *CHARM Radiation Test Facility Highlights from 2024 Operations*. indico.cern, Jan. 2025. URL: https://indico.cern.ch/event/1500025/contributions/6316425/attachments/3004966/5297164/2025_01_29-Fiore-CHARM2024highlightsC.pdf (visited on 02/03/2025).

[98] Andrzej Czarnecki, William J Marciano, and Alberto Sirlin. "Neutron lifetime and axial coupling connection". In: *Phys. Rev. Lett.* 120 (2018), p. 202002. DOI: 10.1103/PhysRevLett.120.202002. URL: https://link.aps.org/doi/10.1103/PhysRevLett.120.202002.

[99] F. M Gonzalez et al. "Improved Neutron Lifetime Measurement with UCNτ". In: *Phys. Rev. Lett.* 127 (Oct. 2021), pp. 162501–. DOI: 10.1103/PhysRevLett.127.162501. URL: https://link.aps.org/doi/10.1103/PhysRevLett.127.162501 (visited on 03/03/2025).

[100] Charles W Clark. *DOWSER: Detecting Objects' Water from Spatial Epithermal-neutron Response*. Nasa.gov, 2025. URL: https://techport.nasa.gov/projects/95815 (visited on 02/22/2025).

[101] W C Feldman et al. "Fluxes of fast and epithermal neutrons from lunar prospector: Evidence for water ice at the lunar poles". In: *Science* 281.5382 (1998), pp. 1496–1500. DOI: 10.1126/science.281.5382.1496. URL: https://www.science.org/doi/abs/10.1126/science.281.5382.1496 (visited on 03/01/2025).

[102] W C Feldman et al. "Major Compositional Units of the moon: Lunar Prospector Thermal and Fast Neutrons". In: *Science* 281.5382 (1998), pp. 1489–1493. DOI: 10.1126/science.281.5382.1489. URL: https://www.science.org/doi/abs/10.1126/science.281.5382.1489 (visited on 03/01/2025).

[103] Arno Smets et al. *Solar Energy: The physics and engineering of photovoltaic conversion, technologies and systems*. English. UIT Cambridge Limited, 2016. ISBN: 978-1-906860-32-5.

[104] *The next Generation Radiation monitor- NGRM*. 2013 IEEE Nuclear Science Symposium and Medical Imaging Conference. IEEE, 2013, pp. 1–6. DOI: 10.1109/NSSMIC.2013.6829497. URL: https://ieeexplore.ieee.org/document/6829497 (visited on 03/01/2025).

[105] hamamatsu. *Characteristics Si Detectors for Scintillator Coupling Si Direct Detectors 4. New Approaches Applications Si Detectors for High Energy Particles 1*. URL: https://www.hamamatsu.com/content/dam/hamamatsu-photonics/sites/documents/99_SALES_LIBRARY/ssd/high_energy_kspd9002e.pdf (visited on 03/01/2025).

[106] Andrea Coronetti et al. "The CELESTA CubeSat in-flight Radiation Measurements and Their Comparison with Ground Facilities Predictions". In: *IEEE Transactions on Nuclear Science* 71.8 (2024), pp. 1623–1630. DOI: 10.1109/TNS.2024.3376749.

[107] C Cangialosi et al. "Thermal neutron SRAM detector characterization at the CERN mixed-field facility, CHARM". In: *IEEE Transactions on Nuclear Science* 65.8 (2018), pp. 1887–1893. DOI: 10.1109/TNS.2018.2829631.

[108] *What Is Energia and How Did It Get Started*. Energia.nu. URL: https://energia.nu/contact/ (visited on 03/06/2025).

[109] M Rovituso et al. "Characterisation of the HollandPTC RD Proton Beamline for Physics and Radiobiology Studies". In: *Physica Medica* 130 (2025), p. 104883. DOI: https://doi.org/10.1016/j.ejmp.2024.104883. URL: https://www.sciencedirect.com/science/article/pii/S1120179724013516.

[110] *Pre-clinical and clinical facilities - HollandPTC*. HollandPTC, Sept. 2023. URL: https://www.hollandptc.nl/research/pre-clinical-and-clinical-research-facilities/ (visited on 07/20/2024).

[111] S.M. Seltzer and P.M. Bergstrom. *Stopping-Power Range Tables for Electrons, Protons, and Helium Ions*. NIST, Oct. 2009. URL: https://www.nist.gov/pml/stopping-power-range-tables-electrons-protons-and-helium-ions.

[112] ptwdosimetry. *PTW 34045, Advanced Markus Electron Chamber - Radiation Products Design, Inc.* Rpdinc.com, 2025. URL: https://www.rpdinc.com/ptw-34045-advanced-markus-electron-chamber-966.html (visited on 02/27/2025).

[113] CERN. *medipix.web.cern.ch*. Cern.ch, 2016. URL: https://medipix.web.cern.ch/our-story (visited on 12/18/2024).

[114] R Ballabriga, M Campbell, and X Llopart. "An introduction to the Medipix family ASICs". In: *Radiation Measurements* 136 (2020), p. 106271. DOI: https://doi.org/10.1016/j.radmeas.2020.106271. URL: https://www.sciencedirect.com/science/article/pii/S1350448720300354.

[115] Rafael Ballabriga, Michael Campbell, and Xavier Llopart. "Asic developments for radiation imaging applications: The medipix and timepix family". In: *Nuclear Instruments and Methods in Physics Research Section A: Accelerators, Spectrometers, Detectors and Associated Equipment* 878 (2018), pp. 10–23. DOI: https://doi.org/10.1016/j.nima.2017.07.029. URL: https://www.sciencedirect.com/science/article/pii/S0168900217307714.

[116] W.S Wong et al. “Introducing Timepix2, a frame-based pixel detector readout ASIC measuring energy deposition and arrival time”. In: *Radiation Measurements* 131 (2020), p. 106230. DOI: `https://doi.org/10.1016/j.radmeas.2019.106230`. URL: `https://www.sciencedirect.com/science/article/pii/S1350448719305165`.

[117] *MiniPIX SPRINTER - Compact Radiation Detection Solution*. Advacam, 2024. URL: `https://advacam.com/camera/minipix-sprinter/` (visited on 11/25/2024).

[118] Andrea Šagátová et al. “Conversion of fast neutrons for neutron radiography with TPX2 detector”. In: *Nukleonika* 69.2 (2024), pp. 135–140. DOI: `10.2478/nuka-2024-0020`. URL: `https://doi.org/10.2478/nuka-2024-0020`.

[119] Martin Urban et al. “Timepix3: Compensation of thermal distortion of energy measurement”. In: *Sensors* 23.6 (2023). DOI: `10.3390/s23063362`. URL: `https://www.mdpi.com/1424-8220/23/6/3362`.

[120] N J Carron. *An Introduction to the Passage of Energetic Particles through Matter*. 1st ed. CRC Press., Nov. 2006. DOI: `10.1201/9781420012378`. (Visited on 12/18/2024).

[121] Sajith Thottathil Abdulrahman et al. “Chapter 1 - Introduction to neutron-shielding materials”. In: ed. by Sajith Thottathil Abdulrahman, Sabu Thomas, and Zakiah Ahmad. Woodhead Publishing, 2020, pp. 1–23. DOI: `https://doi.org/10.1016/B978-0-12-819459-1.00001-5`. URL: `https://www.sciencedirect.com/science/article/pii/B9780128194591000015`.

[122] W.E Burcham. *Elements of nuclear physics*. Longman Group Limited, 1979. URL: `https://books.google.nl/books?id=VmtbngEACAAJ`.

[123] Nuclear Energy Agency (NEA). *JANIS Books*. Nuclear Energy Agency (NEA), 2025. URL: `https://www.oecd-nea.org/jcms/pl_44624/janis-books` (visited on 01/11/2025).

A

Setup details and sensor settings

To conduct radiation measurements using the FGDOS, it is essential not only to understand the underlying physics but also to be familiar with its operation and the engineering aspects of the hardware. The measurement instrument, referred to hereafter as ”the payload”, is assembled in-house at TU Delft, with individual components ordered separately, resulting in a custom-built device.

For this reason, this appendix provides a baseline for the various facets of the experimental setup used in this thesis.

Firstly, an overview of the experimental setup is presented, followed by a discussion of the internal settings of the floating gate sensor and the microcontroller (MCU).

Schematic setup

To control the floating gate dosimeter (FGDOS), as described in subsection 2.5.2, a microcontroller (MCU) is required[1].

During this thesis, two different MCUs were used: the Arduino Uno R3 and the MSP430FR5969IRGZR. The latter is integrated into the mainboard of the payload (see Figure 2.14a) and was used for the CERN experiments.

However, for this example, the Arduino Uno R3 is used to simplify the setup and facilitate prototyping. A schematic representation of the setup is provided in Figure A.1, while Figure A.2 offers a visual representation of the assembled system. The connection shown in Figure A.1 is a simplified representation. In practice, the daughterboard contains resistors and capacitors that ensure proper system functionality. For readers interested in a more detailed view, a schematic of the daughterboard can be found in Shanbhag [2, page 181].

Firmware

To control this system, firmware is required. For this purpose, the Arduino is flashed with code provided by Shanbhag [2], available at: ”Payload-Daughterboard-PERF_TEST-Radiation_Thermal”[2]. Additionally, a modified version of ”FGD_03F_read_save_simple-Payload_PCB.py”[3]

is used to monitor the serial output and log the data into a CSV file with timestamps marking the time of creation. The modifications made to this script allow for greater control over file saving and the automatic generation of a new CSV file every X hours.

Below, the pseudo-code for both scripts is presented.

---

[1] A microcontroller is essentially a small computer integrated into a single (IC)

[2] https://github.com/Abhi-2049/REDMOON/tree/main/TESTING%20CODE/Payload-Daughterboard-PERF_TEST-Radiation_Thermal and it is important to note that the firmware contains a specific code segment that resets the recharge count to zero when it reaches 16.

[3] https://github.com/Abhi-2049/REDMOON/tree/main/TESTING%20CODE/Functional%20Testing%20DAQ%20scripts

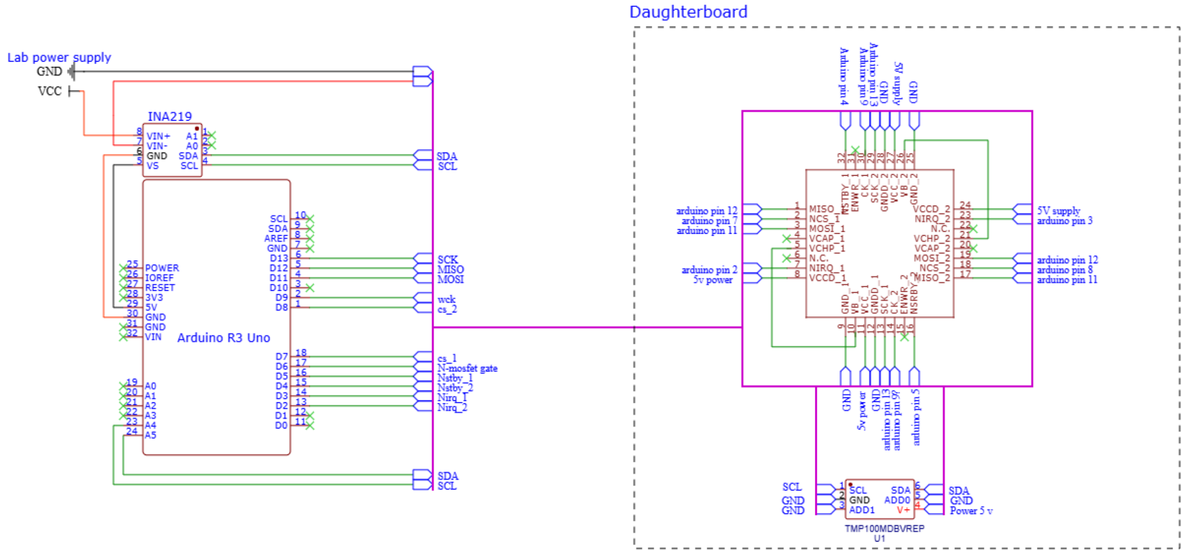

Figure A.1: A schematic of the electronic connections between the daughterboard and the Arduino Uno R3. The I2C connections originate from A4 and A5, linking both the current sensor (INA219) and the external temperature sensor (TMP100). Apart from these, there is a one-to-one connection between the two devices when using the Sub-D connector.

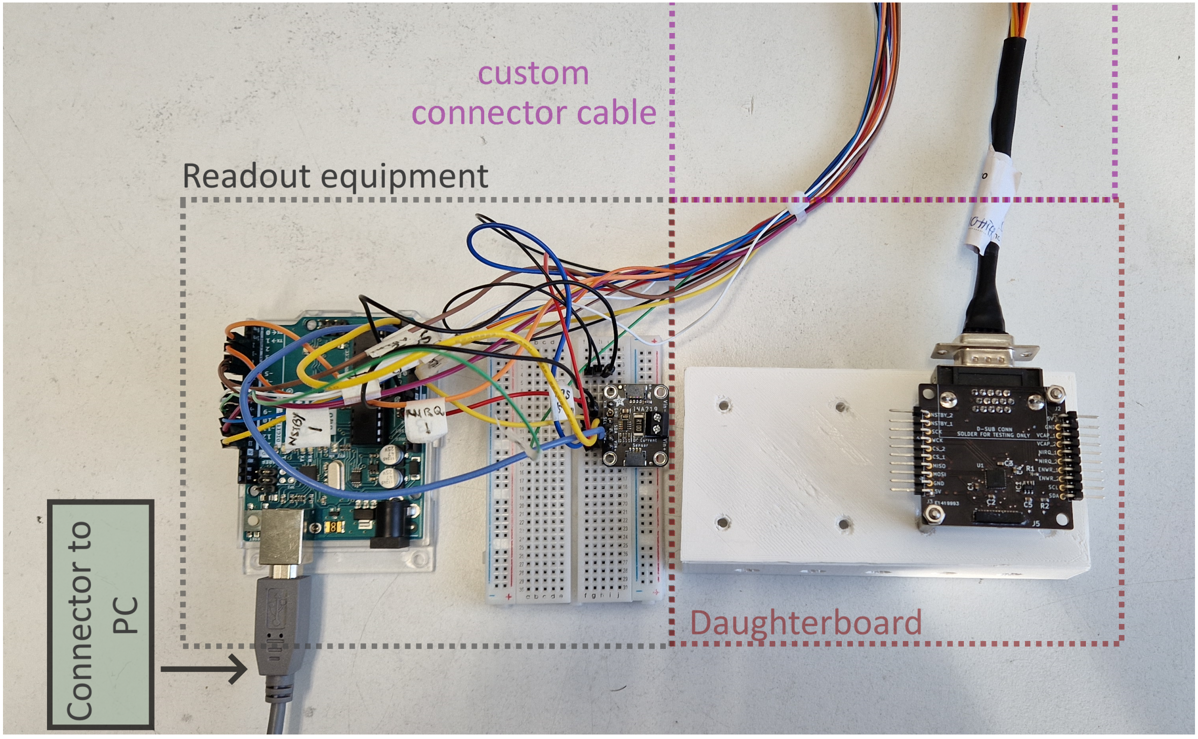

Figure A.2: Illustration of the connections used for HollandPTC and gamma measurements. Note that the power supply is not connected for simplicity. Wire color formatting: red - 5 V line, black - ground, yellow - SCL or SCK, light blue - SDA or MOSI, Orange - NIRQ, brown - NSTBY, white - NCS, green - WCK, purple - MISO. Arduino to PC connector is a USB-A to USB-B cable.

Arduino - pseudo code

```
Initialize Arduino :
    Load Libraries ;
        * SPI.h ;
        * Wire.h
        * adafruit_INA219.h;
        * FGD_03F_extended.h
    Initialize variables ;
    Initialize flags ;
    Declare FGDOS function;
    % Declare Peltier Function (UNUSED)

Void setup() :
    Initialize serial connection with pc
    Initialize INA219 ;
    % Initialize peltier control pin (UNUSED)
    % Initiialize Relay control pin (UNUSED)
    Configure NSTBY pins;
    Initialize Clock module ;
    Initialize payload internal SPI comms ;
    Wait 1 second;

    For each sensor (1 to 2);
        Initialize Sensor;
            Set FGDOS sensitivity mode ;
            Set FGDOS recharging mode ;
            Set FGDOS measurement window ;
            Set FGDOS recharging mode ;
            Set FGDOS recharging source to internal charge pump ;
            Disconnect recharging system ;
            Wait 4 measurement windows;
            Set recharge target and threshold ;
            Set recharge voltage  and Enable recharging system ;
            Wait 2.1 measurement windows;
    Set NIRQ pins to input_pullup;
    Set sensor to open collector (only low);
    Read all FGDOS registers ;

Void loop():
    Read INA219 sensor data;
    Read TMP100 sensor data;
    % if peltier flag true;
    %    update peltier function
    For each sensor;
        If not recharging;
            Read sensor data
            Store sensor data
            print FGDOS, INA219, TMP100 sensor data
        Else if;
            Read sensor data
            Store sensor data
            print FGDOS, INA219, TMP100 sensor data
            print("Measurement loop running")
    Wait 2.1 measurement windows;


    If command was send;
        Execute relevant command;
```

Python - monitoring code- pseudo

```
Load library;
DEFINE path_to_save, folder, filename, com_port, and baud rate;

FUNCTION serial_command(serial_connection);
    LOOP FOREVER;
        READ user input as command;
        SEND command to serial_connection;

FUNCTION main();
    CREATE folder path to save data;
    IF folder does not exist;
        CREATE the folder;

    GENERATE datafile name using current date and time;
    CONNECT to serial port using com_port and baud rate;
    PRINT connection confirmation;

    START a separate thread to handle serial_command with the serial connection;

    OPEN datafile for appending;
    SET t_stamp to current time in nanoseconds;

    TRY
        LOOP FOREVER;
            WAIT for serial data with a timeout;
            IF timeout occurs;
                PRINT timeout message;
                CONTINUE;

            WHILE there is data in serial buffer;
                TRY;
                    READ a line from serial and decode it;
                CATCH decoding error;
                    PRINT error message;
                    BREAK;

                GET current time (t);
                CALCULATE elapsed time since t_stamp in microseconds;
                CREATE datastring with elapsed time and serial data;
                PRINT datastring;
                WRITE datastring to file;

                IF elapsed time since t_stamp exceeds x Hours;
                    CLOSE the current file;
                    GENERATE a new datafile name;
                    OPEN new datafile for appending;
                    RESET t_stamp to current time;
    CATCH KeyboardInterrupt;
        EXIT gracefully;

CALL main();
```

A.1. Settings

The settings of the devices are just as important as the results they reveal. Below, two tables are presented to highlight these configurations.

Firstly, the settings used to control the FGD-03F sensors are shown. This is achieved by modifying the register map via the SPI[4] communication protocol. A complete list of register settings can be found in Micro [4, pages 19–22 of A0.11].

Register Map Addr.	Value	Important Bits
0x09	$0x0B_h$	**TARGET**: Target frequency bit
0x0A	$0x06_h$	**Threshold**: Threshold frequency bit
0x0B	$0xCD_h$	**EAWR**: Enable automatic recharging mode (ECH must be 1) **EVBCHP**: Internal pump charge from VB pin **NCHP**: Internal or external pump source **ENDCH**: Floating gate user-controlled discharge **WINDOW**: Window length select bit **TVID**: X/8 divider for TARGET and Threshold Register value
0x0C	$0x79_h$	**FCH**: Force recharge bit (When ECH and FCH = 1, recharge happens if VB is high voltage) **SENS**: Sensitivity configuration bit
0x0D	$0x44_h$	**ENMC**: Enable external compensation mode **ECH**: Recharge global enable (affects all recharge methods) **EPWR**: Enable pin-controlled recharging (When EPWR, ECH, EWWR = 1, and VB pin is high) **NEASN**: Enable automatic sensor/reference alternate measurement **E2V**: Reference voltage selection for measurement **SET**: Internal charge pump voltage [14.5 -18 V]
0x0E	$0x06_h$	**LOWN**: FSM Timebase oscillator control during measurements **EDIRT**: Measurements during SPI enable bit **NIRQOC**: Interrupt output bit [open collector] **ENGATE**: Measurement window by counts or grating at ck pin

Table A.1: Register map configuration for testing with the daughterboard. The “h” in the Value column indicates hexadecimal notation.

Attribute	Value
Lab power Supply	5V
Readout interface	SPI through Arduino
Sensor Mode	Active
Sensitivity Modes	HI SENS
Window Clock Frequency (WCK)	31250 Hz
Window Pulses	4096
Recharge Mode	Auto recharge from internal pump
Recharge Voltage	16.5 V
SPI Frequency	5 MHz
Baud rate	250000
Recharge Target Frequency - HI SENS	90000 Hz (85937.5)
Recharge Threshold Frequency - HI SENS	50000 Hz (46875)

Table A.2: FGDOS configuration details

---

[4] Serial Peripheral Interface

Practical tips

- Figure A.1 does not include a relay module. The purpose of a relay module would be to enable power cycling via external commands, which is particularly necessary in harsh radiation environments where SEEs may occur. To achieve this, every electronic line carrying more than 1.5 V is connected in series with a separate relay module, allowing the power to be switched off when needed. In most cases, switching the power line in combination with the SPI lines (MOSI, MISO, NCS, SCK) is sufficient to restore functionality. The reason for including the communication lines in the relay module is that power leakage can occur through the system, potentially keeping parts of the circuit active even when the main power line (5V) is disconnected.
- Previous experiments included a Peltier element attached to the back of the PCB. This was done to simultaneously vary both temperature and radiation exposure.

B

Temperature compensation

As mentioned in subsection 2.5.1, the drain current is temperature sensitive. To account for this, an identical MOSFET is included in the circuit to compensate for this behavior. This appendix presents how temperature affects the sensor output, explains how to compensate for it (as outlined in Micro [4]), shows the compensated results, and finally illustrates the non-linear behavior under extreme temperature variations.

For this example, the sensor used by Shanbhag [2] to investigate the simulation behavior of radiation and temperature was used. This sensor was exposed to approximately 61 Gy(Si) [87] (with the facility reporting 66.79 Gy(air) [2]) the temperatures were cooled using a freezing spray to -15 °C, then allowed to return to ambient temperatures through natural convection. The experiment took place on 24-08-2022, where this temperature measurement was conducted on 06-09-2024. Before proceeding, it is important to mention that it was reported by Brucoli et al. 2017 [72] that a small variation in the properties of the sensors from different batches, in addition to intra-batch variations, is to be expected.

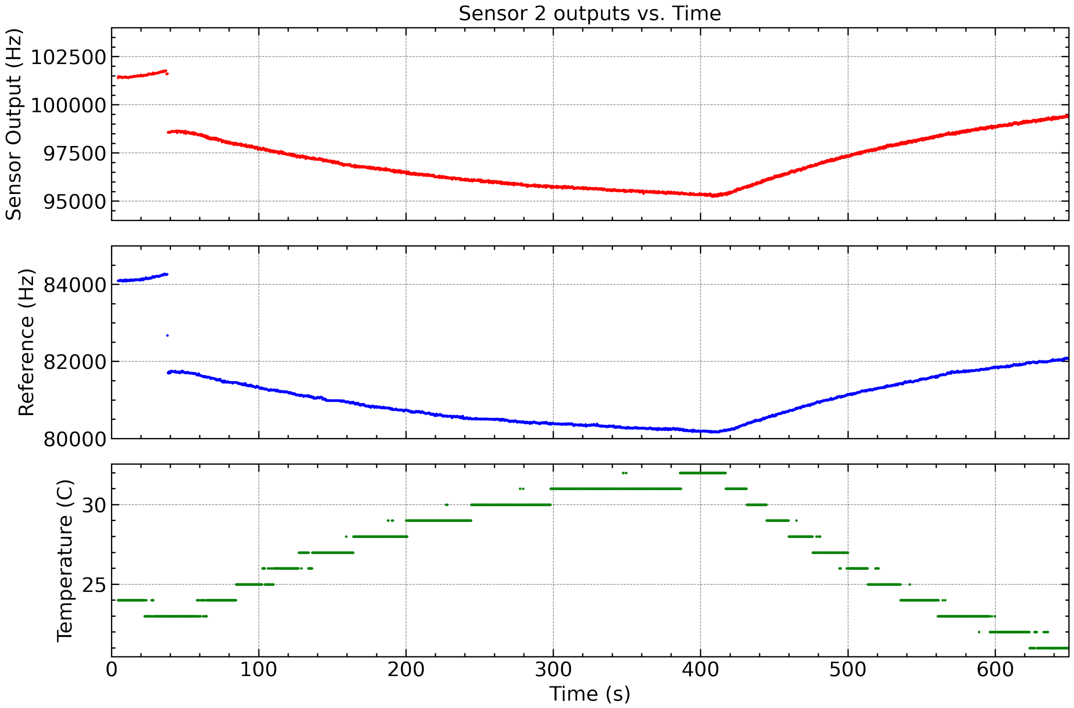

Figure B.1: Sensor output, reference output and calibrated internal temperature sensor as a function of time. The jump observed at approximately ± 40 seconds is caused by a slight, unintentional change in voltage when enabling the power to the Peltier element.

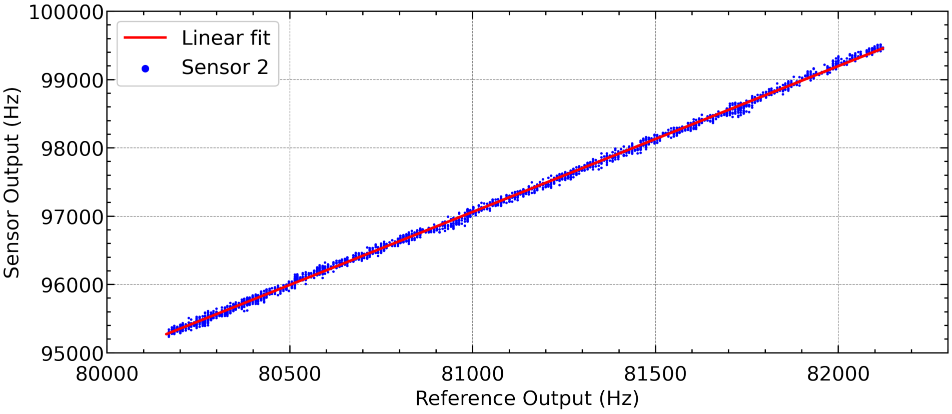

Figure B.2: Sensor output as function as reference output.

To heat the sensor, the floating gate dosimeter (FGD-03F Z1.1, serial number: 192301) mounted on a daughterboard (see Figure 2.14b) is gradually heated using a single-stage Peltier element[1], which is attached to the back of the PCB. Below, only the results of the second sensor (Sensor ID: 65645) on the IC are presented, as the results from the other sensor on the IC were nearly identical. Once the desired temperature is reached ($\pm$ 15 °C above ambient temperature), the inverse process can take place, monitoring the behavior of the sensor as it cools naturally to ambient temperature through convection.

From Figure B.1, it can be observed that there is a correlation between the reference and sensor outputs as a function of temperature fluctuations. Based on the datasheet [4], it can be assumed that this behaviour is linear. Using this assumption, the sensor output as a function of the reference output can be plotted, as shown in Figure B.2. In Figure B.2, it can be observed that this behavior is indeed linear. If we then apply a linear fit through the data (e.g. in Python using Sklearn, LinearRegression function), a slope is obtained. In this case, that corresponds to 2.136 ± 0.002 with R^2 of 0.9988. Using Equation 2.17, the behavior of temperature can be compensated for, as seen in Figure B.3. Note that the error of 0.002 has a minuscule effect on the compensation and cannot be observed in the graph.

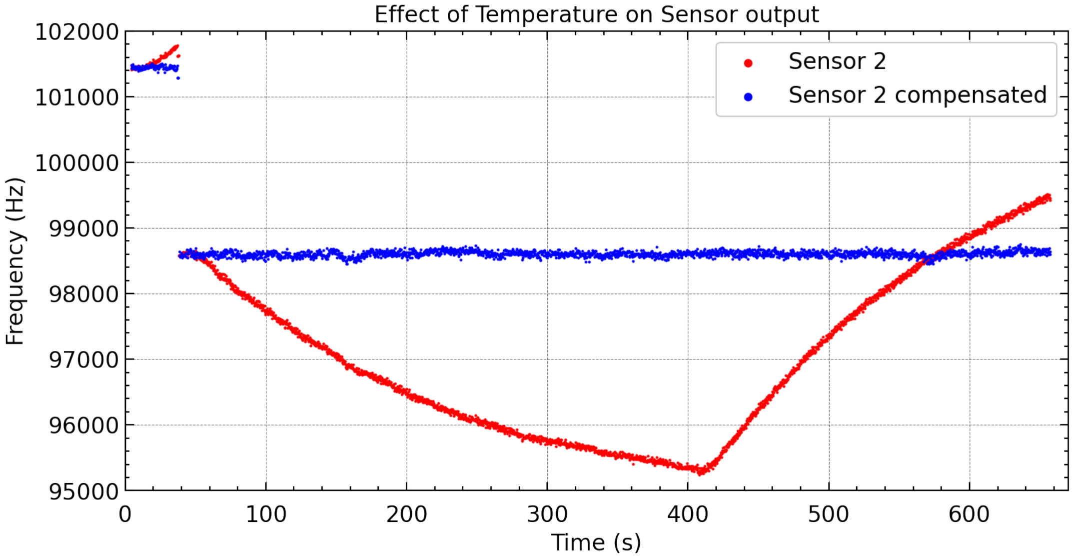

Figure B.3: Raw sensor output and temperature corrected sensor output as a function of time. The jump observed at the beginning was caused by voltage chance.

---

[1] A Peltier element is an electronic component that transfers heat from the colder side to the warmer side using the Peltier effect by consuming electrical energy.

Non-linear behaviour

To allow for this compensation, the assumption was made that the sensor output and the reference output follow a linear correlation. However, it can be observed that when the temperature is increased extensively, the behavior becomes non-linear, as shown in Figure B.4. The correlation differs when the device is heated using a Peltier element compared to when it is cooled afterward through natural convection. This highlights the need to keep the device within its linear operating range. A brief remark about this test: The device was heated in multiple stages up to 90°C and cooled in two stages. The data was acquired following the same procedure as described earlier and in Appendix A, with the total experiment lasting 760 seconds.

The tested device was an FGD-03F Z1.1 [2], mounted on a daughterboard. Prior to this test, the sensor had been exposed to simultaneous proton irradiation and varying temperature profiles ranging from ambient conditions to 93°C. This exposure resulted in a total radiation dose of approximately 61 Gy(Si) [87]. Additionally, upon initial use, it was found that the sensor was operating outside the linear range, as indicated in the datasheet [4].

Since different sensors exhibit slight variations in behavior, and the conditions of this test were not ideal, repeating the experiment in the future could be beneficial. A particular focus on repeated temperature cycling would provide a deeper understanding of the sensor's behavior.

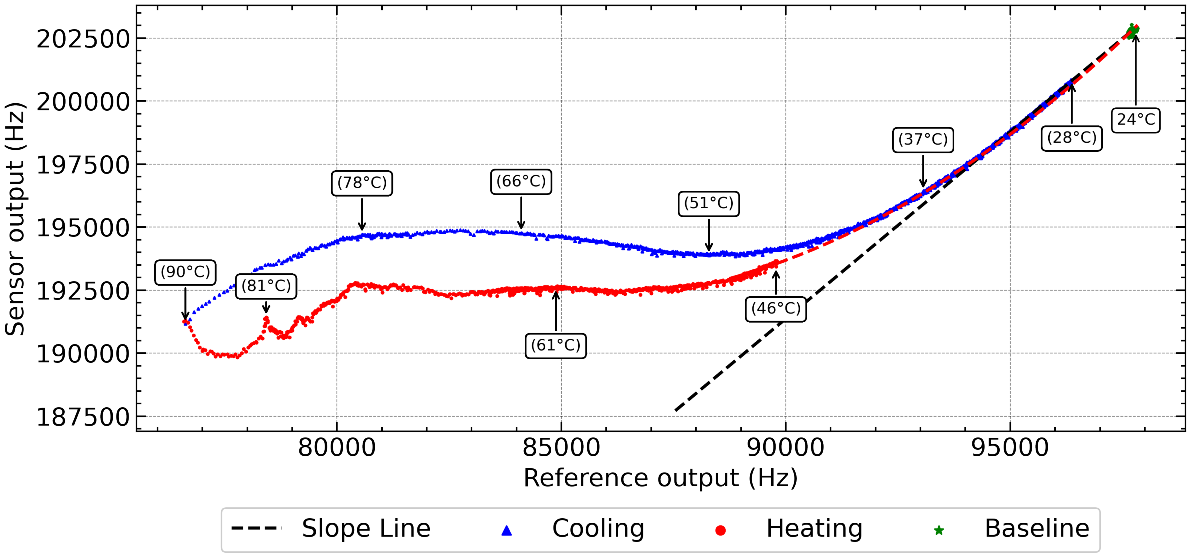

Figure B.4: Sensor and reference output as a function of temperature. This data corresponds to the second sensor used by Shanbhag [2], which was simultaneously exposed to high temperatures and pre-irradiation during testing. The red line represents the sensor response during heating, while the red dashed line indicates a second-order polynomial interpolation between the first 250 data points and the baseline. The blue line represents the sensor response during natural convection cooling, and the black line shows a linear fit through the final cooling points and the baseline. Sensor details: FGD-03F Z1.1 (serial number: 192301, sensor ID: 65557).

Overal remarks

- A quicker approach to heating the sensor could be placing the PCB in a container and heating the surrounding air, for example, using a heat gun.
- When repeating the process of conducting a linear fit through the data (starting with the baseline and sequentially adding points from the cooling phase in reverse order) and plotting the R^2 value as a function of the number of points, it can be observed when R^2 drops below 0.95. In this test, that corresponded to a point where the temperature was 36 °C. At that point, the error increased so significantly that temperature compensation using a linear assumption was no longer valid. In such cases, a lookup table is required.

---

[2] serial number: 192301, sensor ID: 65557

C

HollandPTC campaign

Located next to RID, the Holland Proton Therapy Centre (HollandPTC) is an independent outpatient facility specializing in proton therapy. However, as the underlying biological mechanisms are not yet fully understood, and proton therapy could benefit from further technological advancements, the facility also houses an R&D proton beamline [109]. Since previous students (De Meyere [1] and Shanbhag [2]) have used this facility for their experiments, the purpose of this appendix is to provide a brief introduction to the HollandPTC and present an exploratory experiment conducted as part of this thesis.

C.1. The facility

Figure C.1: Photo of HollandPTC R&D beam line [110]

HollandPTC uses an isochronous cyclotron to accelerate the protons [109]. Cyclotrons use electromagnetic fields, where magnetic fields are used to confine particles while oscillating electric fields (positive and negative polarity) are used to accelerate them. In classical cyclotron, as particles gain energy they

take longer to complete a circular orbit, making it difficult to allow for a continuous acceleration of particles as the oscillating electric field required must match the particle orbit frequency. The isochronous cyclotron solves this by having a magnetic field that increases with the distance from the cyclotron centrum. This allows the orbital frequency to remain contained, while their energy increases, enabling a steady and high-intensity particle beam. After the desired energy is reached, the particles are moved around using a vacuum beam pipe and magnetic field to four different rooms, one of them is the R&D room, as displaced in Figure C.1. From the beam exit, a pencil beam originates. This is a highly focused, narrow beam of particles[1] (often just a few millimeters wide)[2].
The particles will then travel through a custom setup that allows for live monitoring of the beam and the production of large uniform fields ranging from 2x2 cm up to 20x20 cm[3]. After this, the protons will hit the device under target (DUT). The user has control over the field shape (pencil beam or passive scattering mode), the proton energy (between 70 MeV and 240 MeV, with energy steps of 0.5 MeV), the duration, and the beam current. The latter is a measure of the flow of charged particles in a particle beam, in units of number of particles per second [109, 110]. It can be expressed as follows:

$$I_b = e \cdot n, \tag{C.1}$$

Where,

- I_b is the beam current in Ampere
- e is the charge of a single proton ($e = 1.602 \cdot 10^{-19}\ C$)
- n is the number of particles per second passing through a point.

Using proton energy and beam current, the HollandPTC internal calibration provides other units to users such as flux, fluence at the DUT, and dose rate.

C.2. Methodology

The objective of this experiment was to evaluate the performance of the FGDOS under proton irradiation. Additionally, secondary objectives were considered, such as assessing the behavior of the Lunar Zebro chassis and investigating lower dose rates. However, because of personal circumstances, and adding shielding material to the beamline required permission from RID Radiation protection unit, the tests were limited to replicating Run 1.2 and 1.4–1.6 from Shanbhag [2, Table 5.10].

For this experiment, the same setup was used as described in Appendix A, with the daughterboard referred to as ”hot” by Shanbhag [2]. The device in question was an FGD-03F Z1.1[4]. Prior to this, the sensor had been exposed to simultaneous irradiation and temperature cycling [2, Chapter 5.3]. In addition, a single high-temperature heating cycle was conducted to investigate extreme temperature behavior, as seen in the last page of Appendix B. Furthermore, sensor 2 was subjected to discharge and recharge mapping, pushing it far beyond the linear range.

In summary, the FGDOS IC used in this appendix had already undergone significant exposure to various conditions. Below, Table C.1 presents a summary of the different runs, along with their respective physical parameters. As shown in Table C.1, the reported values are given in Gy(air), which represents the dose received at the Device Under Test (DUT). However, the device itself absorbs only a portion of this energy. To account for this, a comparison is made using the stopping power of dry air and Si, allowing for the establishment of a conversion factor, as presented in Table C.2.

The stopping power can be divided into two components: electronic stopping power and nuclear-stopping power. The former refers to energy loss due to interactions with electrons in the material, while the latter results from elastic collisions with nuclei in the target material.

---

[1] Gaussian shape in both x and y direction with σ values ranging from 3.6 mm up to 5.4 mm for the maximum and minimum energy, respectively

[2] In other particle accelerators, other beam shapes can be encountered like: Gaussian beam, scattering beam, spot beam, and so on.

[3] Using a dual-ring passive scattering system, with one ring used for low dose rate that produce uniform fields up to 20 cm diameter, referred to as thick ring, and the other one for high dose rate that produce fields up to 8 cm diameter, referred to as thin ring.

[4] serial number: 192301, sensor ID: 65556 and 65557

Table C.1: The HollandPTC proton campaign summary of 27-08. The beam energy was kept at 120 MeV, the field size was 10x10, and proton intensity was $8.77 \cdot 10^5$ protons/s/nA

Beam current [nA]	Flux [$\frac{Protons}{cm^2 \cdot s}$]	Dose rate [$\frac{Gy(air)}{min}$]	Run	Duration [s]	TID [$Gy(air)$]	Anomlies
700	$6.14 \cdot 10^7$	0.65	1	9.6	0.53	Run cut short
			2	275.8	15.24	
			3	25.6	1.41	Run cut short
			4	233.6	12.91	
			8	357.8	19.78	
70	$6.14 \cdot 10^6$	0.065	5	109.8	0.61	Run cut short
			6	654.0	3.61	
7	$6.14 \cdot 10^5$	0.0065	7	825.8	0.46	
-	-	-	Base	370.1	-	
-	-	-	End	415.0	-	
				Total:	54.56	

Energy (MeV)	Stopping Power in Si (MeV cm^2/g)	Stopping Power in Air (MeV cm^2/g)	Conversion Factor (Air to Si)
70	7.611	8.440	0.902
120	5.118	5.636	0.908
200	3.627	3.975	0.912

Table C.2: Electronic stopping powers for Si and dry air. Using this, the conversion factors can be calculated. [111]

C.2.1. Facility uncertainty

Communication with the facility indicates that internal calibrations are performed using a Markus chamber PTW. Specifically, this is a Type 34045 chamber, capable of measuring with 1% accuracy. [89, 112] Since this is an exploratory experiment, the uncertainty in the dose rate is neglected for the remainder of the analysis.

C.3. Results

In Figure C.2, the raw results of the HollandPTC test are shown. At first glance, the values appear to be multivalued, but this is not the case. Due to noise in the system, the values intermittently drop to a lower denominator at irregular time intervals.

Noise

The true origin of the noise observed in this test was never fully determined. It is presumed to be partially caused by degradation of the readout circuitry. Additionally, it was observed that several resistors and capacitors were not properly soldered onto the PCB, which could have introduced further noise into the system. This could also be caused by the previously mentioned temperature cycling.

Filtering

By combining the data into a single data frame and using the fact that FG discharges as a function of radiation, the data can be filtered. As a first-order approach, a selective filtering method was applied to the overall dataset to roughly remove outliers. This was followed by an iterative linear regression, which excluded data points that deviated by more than three standard deviations from the fit. This process resulted in two datasets: one containing the ”true” sensor data and another containing the outliers. This method could be further improved to minimize human bias in the results.

In the next subsections, the discussion will primarily focus on the results obtained using the ”true” dataset.

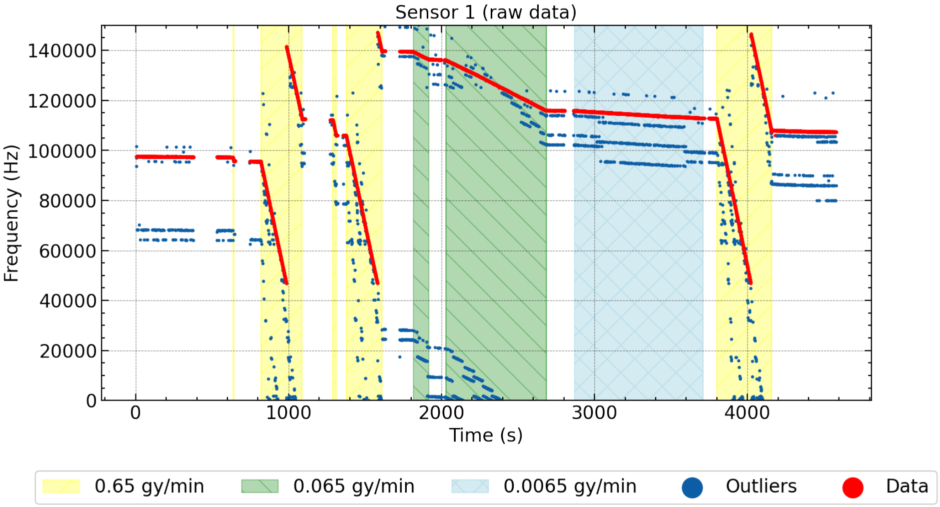

(a) Sensor 1

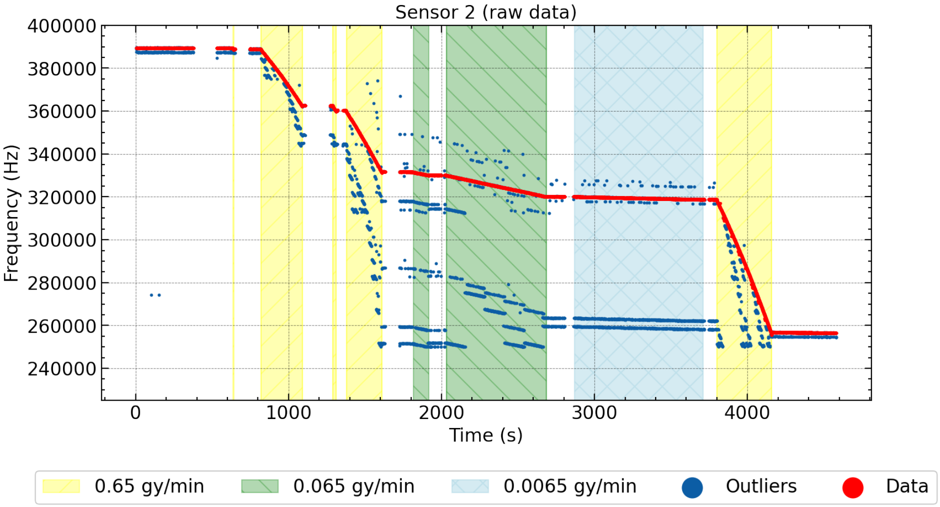

(b) Sensor 2

Figure C.2: The raw sensor data collected during the experiment, with different dose rate regions highlighted throughout the irradiation campaign. Outliers have been filtered out to improve data clarity.

Recharging

Firstly, as seen in Figure C.2a, the sensor automatically recharged three times after its value dropped below 46,875 Hz. However, instead of recharging to 85,937.5 Hz, as specified in the register map, the sensor recharged to 141.6 kHz, 147.22 kHz, and 146.56 kHz in approximately 1.054, 0.77, and 1.043 seconds, respectively.

As a result, the sensor operated outside its linear range for a bit, as defined in data sheet [4].

Sensor 1 vs Sensor 2

The only instances where the sensor values fall within the linear range occur when both sensors are irradiated at 0.65 Gy(air)/min, allowing for a direct comparison between Sensor 1 and Sensor 2 within the same time interval.

Sensor 1 exhibits a decrease in frequency at rates of -293.4 ± 0.3 Hz/s, -290.6 ± 0.3 Hz/s, and -299.04 ± 0.3 Hz/s, while Sensor 2 decreases at rates of -93.4 ± 0.3 Hz/s, -124.9 ± 0.3 Hz/s, and -169.6 ± 1.0 Hz/s. This suggests that sensor sensitivity increases over time as it approaches the linear range. Within the linear range, Sensor 1 has an average sensitivity of -29.65 ± 1.3 kHz/Gy[5], while Sensor 2

---

[5] Using Equation 2.10

shows an increasing sensitivity from -9.51 ± 0.03 kHz/Gy (at 379 kHz) to -17.2 ± 0.1 kHz/Gy (at 293 kHz). This raises the question: how does the charge on the FG affect sensitivity? To investigate this, all data points subjected to 0.65 Gy(air)/min were considered, with the data binned every 80 points, unless the sensor recharged or a different run was initiated (i.e., runs were not combined). Based on this, the sensitivity as a function of charge accumulation on the FG was plotted, as shown in Figure C.3b.

The uncertainty in the y-axis represents the fit accuracy but does not account for uncertainties in the dose rate measurement and the air-to-Si conversion factor. The x-axis error bars indicate the bin width.

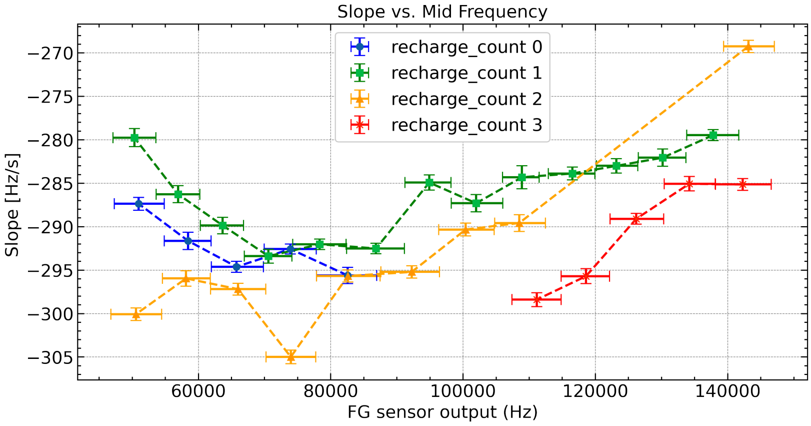

(a) Sensor 1 response to 0.65 Gy(air)/min. Data points are categorized based on the number of recharge events triggered during the experiment.

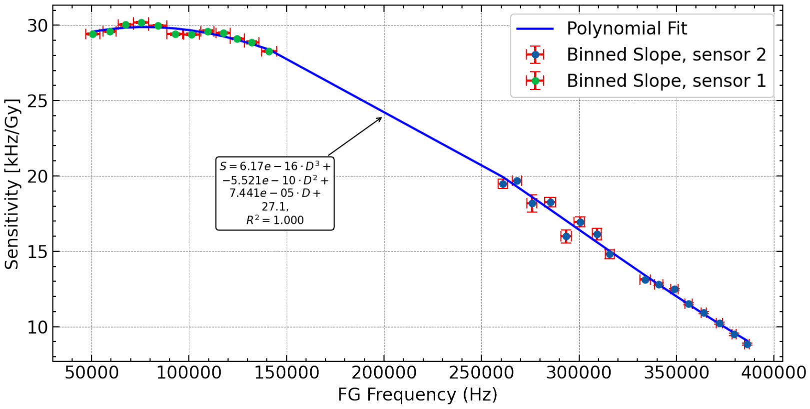

(b) A combined sensitivity curve as a function of the number of charges on the FG.

Figure C.3: Sensitivity measurements at a proton energy of 120 MeV and beam current of 700 nA.

Dose rate comparison

Thirdly, a comparison between different dose rates is conducted. For this analysis, only the results from Sensor 1 are considered. The assumption is that each value experiences the same sensitivity. In reality, this is not entirely the case, as not all values fall within the linear range. However, the differences in dose rate are significantly larger than the fluctuations in dose rate, making it reasonable to assume that sensitivity remains constant.

For each dose rate, the average sensor response is calculated to smooth out uncertainties caused by temperature variations or sensitivity degradation as a function of TID (see section 2.5 for further explanation). The dose rate is converted from Gy(air)/min to Gy(Si)/s to ensure that sensitivity is determined by the slope coefficient of the linear regression applied to the data.

The results are presented in Figure C.4. From this, it can be concluded that there is a correlation between proton flux and the sensor response, as expected.

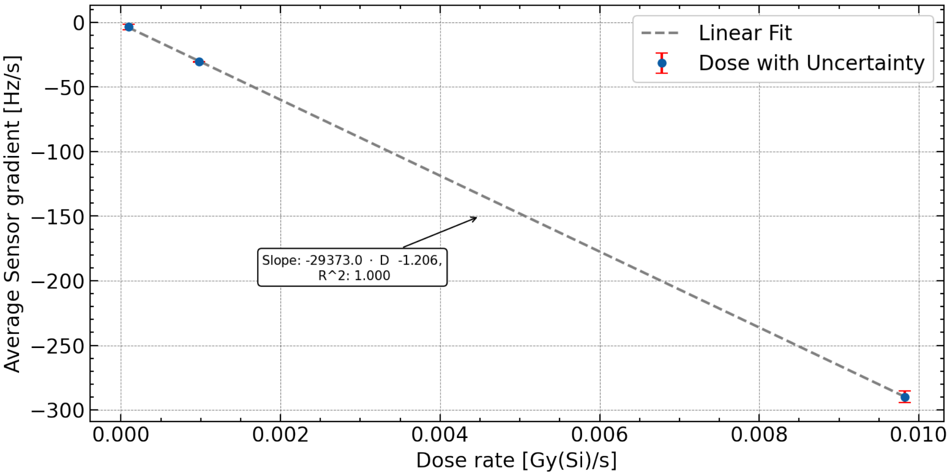

Figure C.4: Floating Gate dosimeter response to different proton fluxes at 120 MeV.

post-irradiation characteristic

Finally, during the end-line measurement, a non-linear decay was observed (see Figure C.5). This occurred immediately after exposure to a dose rate of 0.65 Gy(air)/min. Even after temperature correction, the trend remained unchanged. One possible explanation is that this decay is caused by the activation of the device, leading to a gradually decreasing dose rate after irradiation. However, another possibility is that the effect is driven by an annealing process occurring immediately after irradiation. An exponential decay was fitted to the data, resulting in a decay constant of 0.0036 s^{-1}. However, this value does not yet correspond to a direct physical quantity, as it is still biased by the sensor's response. Additionally, the specific component responsible for activation remains unknown, and the observed decay is likely the result of a summation of multiple decaying isotopes.

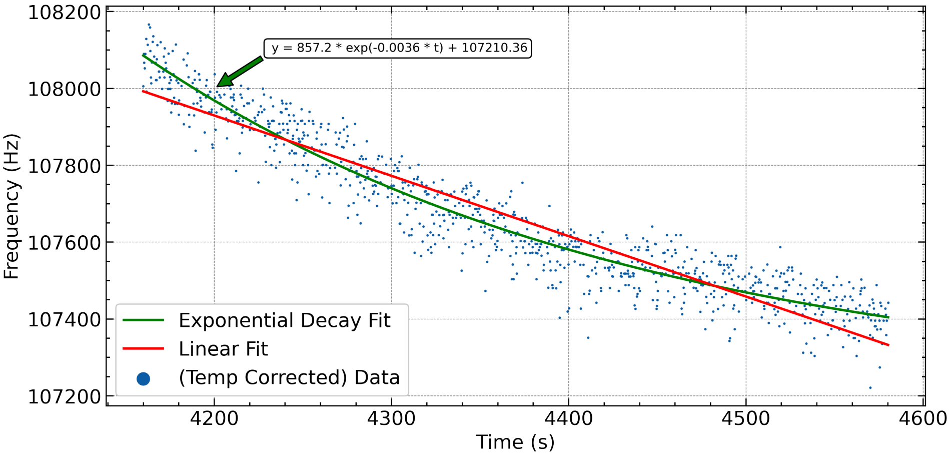

Figure C.5: Post-experiment temperature-corrected sensor response as a function of time. Both linear and exponential fits are plotted to illustrate the data trends.

C.4. Discussion and comparison to literature

During this experiment, the FGDOS was exposed to 120 MeV protons at three different dose rates, allowing for an investigation of the sensor's behavior under irradiation. A lower sensitivity than that reported in the data sheet [4] was observed. This finding is consistent with the results of Shanbhag [2], who measured a sensitivity between 33 and 37 kHz/Gy for the same sensor. Similarly, De Meyere [1] reported a sensitivity of 35 kHz/Gy in his tests.

Additionally, Danzeca et al. [58] found a sensitivity of 28.87 kHz/Gy(Si) using 101 MeV protons at 5.30

Gy(Si)/h and 29.7 kHz/Gy with Co-60 at 0.87 Gy(Si)/h. Álvarez et al. [67] reported a sensitivity between 23.0 and 27.1 kHz/Gy(Si) with Co-60 at 1.15 Gy(Si)/h.

Furthermore, De Meyere [1] mentioned discussions with researchers at CERN, where it was hypothesized that low sensitivity could be attributed to low energy levels. Regardless, the results of this experiment further confirm the observations reported in previous studies.

D

Source Code Example

D.0.1. CERN MCU Code

```
Initialize MCU :
    Load Libraries ;
    Configure GPIO pins ;
    Initialize variables ;
    Initialize flags ;

    Initialize Clock module ;

    Configure RS485 transceiver ;
    Initialize payload internal SPI comms ;
    Initialize payload internal Serial comms ;

    Configure onboard memory storage ;

Initialize FGDOS :
    Initialize SPI registers ;
    Set FGDOS sensitivity mode ;
    Set FGDOS recharging mode ;
    Set FGDOS measurement window ;
    Set FGDOS recharging mode ;
    Set FGDOS recharging source to internal charge pump ;
    Disconnect recharging system ;
    Set recharge target and threshold ;
    Set recharge voltage ;
    Enable recharging system ;
    Wait ;
    Read all FGDOS registers ;

Loop:
    Set WCK signal
    Wait
    For each sensor (1 to 4):
        Read sensor data
        Store sensor data
    Wait
    Reset WCK signal
    Enable RS485 communication
    Transmit stored sensor data
    Disable RS485 communication
    Check for received command
```

```
    Interpret command
    If loop count == 50: (example number)
        Calculate CRC-8
        Save sensor 1-4 data to internal memory
        Reset loop counter

```

E

Activity CHARM setup

On the 22th of January 2025 on 15:22:05, the setup used in CERN underwent a spectra, to understand how radioactive this was and see if it was ready for transportation. This analyse was done 85 days, 13 hours, 12 minutes and 34 seconds after the charm beam was stopped. Meaning to say, all short lived isotopes have long decayed.

Table E.1: An overview of active isotopes in the CERN device.

Nuclide	Half-life	Activity (bq)	Heat (W)	Ambient dose Rate H_{10} ($\mu Sv/h$)	E_{ing} (mSv)	E_{inh} (mSv)	$\frac{A(Bq)}{LA(Bq)}$	Radio-active Content
Ag-105	41.3 d	6.28e+0	5.54e-13	6.41e-5	2.95e-6	5.09e-6	1.05e-6	(β/γ)
Ag-110m	249.78 d	8.21e+1	3.73e-11	3.36e-3	2.30e-4	9.85e-4	1.17e-4	(β/γ)
Be-7	53.22 d	2.87e+3	2.29e-11	2.30e-3	8.04e-5	1.58e-4	2.87e-5	(β/γ)
Co-56	77.31 d	1.18e+2	7.02e-11	5.72e-3	2.95e-4	7.91e-4	1.18e-4	(β/γ)
Co-57	271.80 d	1.55e+2	3.56e-12	3.26e-4	3.26e-5	1.55e-4	1.94e-5	(β/γ)
Co-58	70.86 d	5.89e+2	9.54e-11	8.66e-3	4.36e-4	1.24e-3	1.96e-4	(β/γ)
Co-60	5.271 y	5.19e+1	2.16e-11	1.90e-3	1.76e-4	1.61e-3	1.73e-4	(β/γ)
Cr-51	27.703 d	7.36e+2	4.29e-12	3.68e-4	2.80e-5	2.72e-5	7.36e-6	(β/γ)
Fe-59	44.495 d	1.09e+2	2.28e-11	1.91e-3	1.96e-4	4.36e-4	5.45e-5	(β/γ)
Ir-192	73.822 d	7.26e+0	1.20e-12	9.51e-5	1.02e-5	4.79e-5	7.26e-6	(β/γ)
Mn-52	5.595 d	3.66e+0	2.07e-12	1.87e-4	6.59e-6	5.12e-6	1.22e-6	(β/γ)
Mn-54	312.13 d	4.91e+2	6.61e-11	6.19e-3	3.49e-4	7.37e-4	1.23e-4	(β/γ)
Na-22	2.6027 y	2.42e+2	9.25e-11	7.99e-3	7.74e-4	3.15e-4	8.07e-5	(β/γ)
Ni-56	6.075 d	4.31e+0	9.83e-13	1.12e-4	3.71e-6	4.31e-6	8.62e-7	β/γ
Sb-124	60.20 d	2.34e+2	8.37e-11	6.11e-3	5.85e-4	2.01e-3	2.34e-4	(β/γ)
Sc-46	83.79 d	2.01e+2	6.83e-11	6.01e-3	3.02e-4	1.37e-3	2.01e-4	(β/γ)
Se-75	119.6 d	1.52e+1	9.86e-13	9.73e-5	3.95e-5	1.98e-5	5.07e-6	(β/γ)
Sn-113	115.09 d	6.12e+1	2.90e-13	1.16e-4	4.47e-5	1.65e-4	2.04e-5	(β/γ)
V-48	15.974 d	3.50e+1	1.72e-11	1.51e-3	7.00e-5	8.40e-5	1.75e-5	(β/γ)
Zn-65	244.15 d	2.86e+3	2.70e-10	2.46e-2	1.12e-2	6.29e-3	1.43e-3	(β/γ)
Zr-88	83.0 d	4.03e+1	2.62e-12	3.06e-4	1.81e-5	1.45e-4	4.03e-5	(β/γ)
Total: 21		**8.91e+3**	**8.84e-10**	**7.79e-2**	**1.48e-2**	**1.66e-2**	**2.88e-3**	

F

Extra images

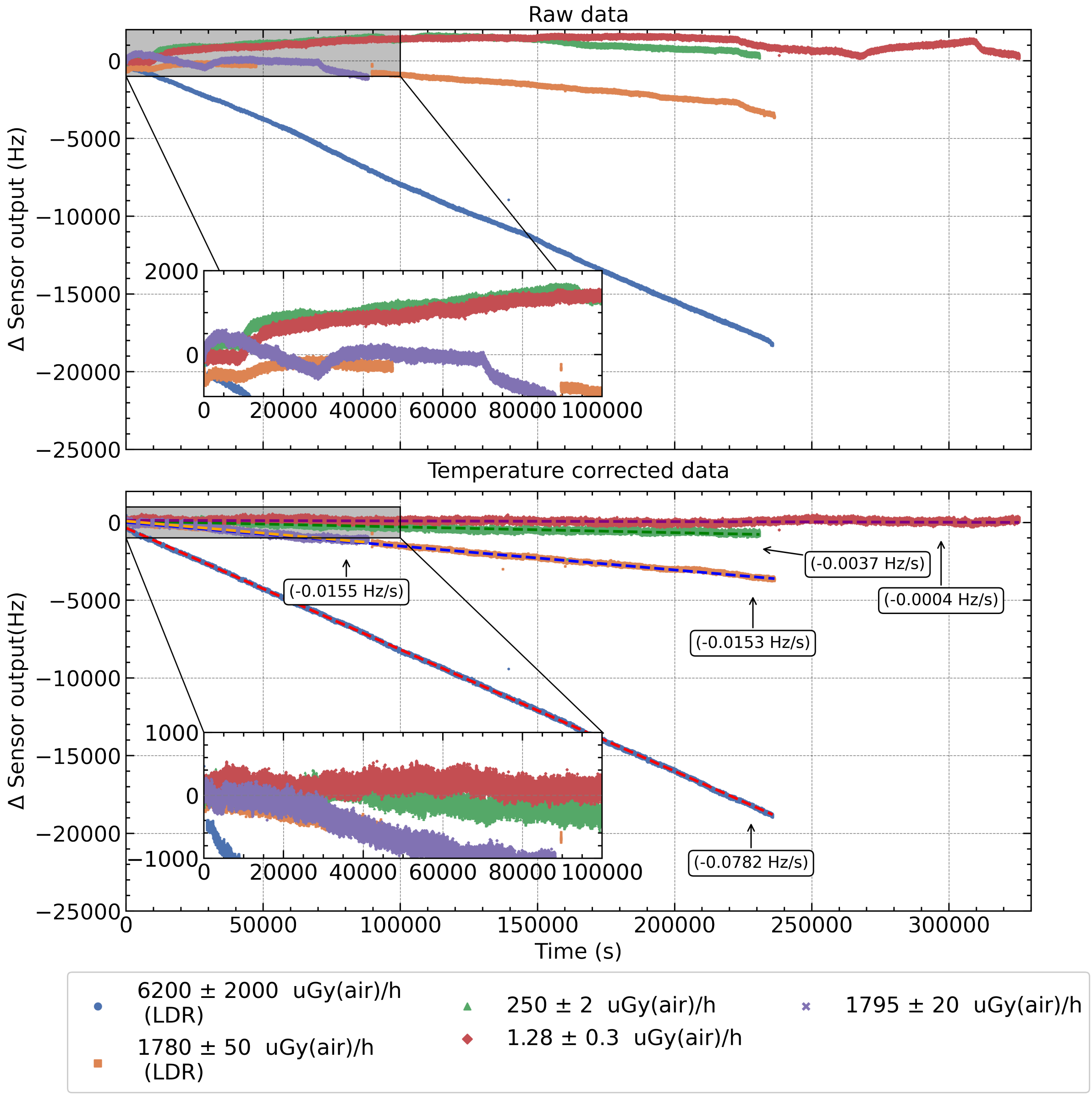

Figure F.1: Sensor 1 of the ”cold” board during low gamma irradiation campaign, see chapter 3 for more explanation

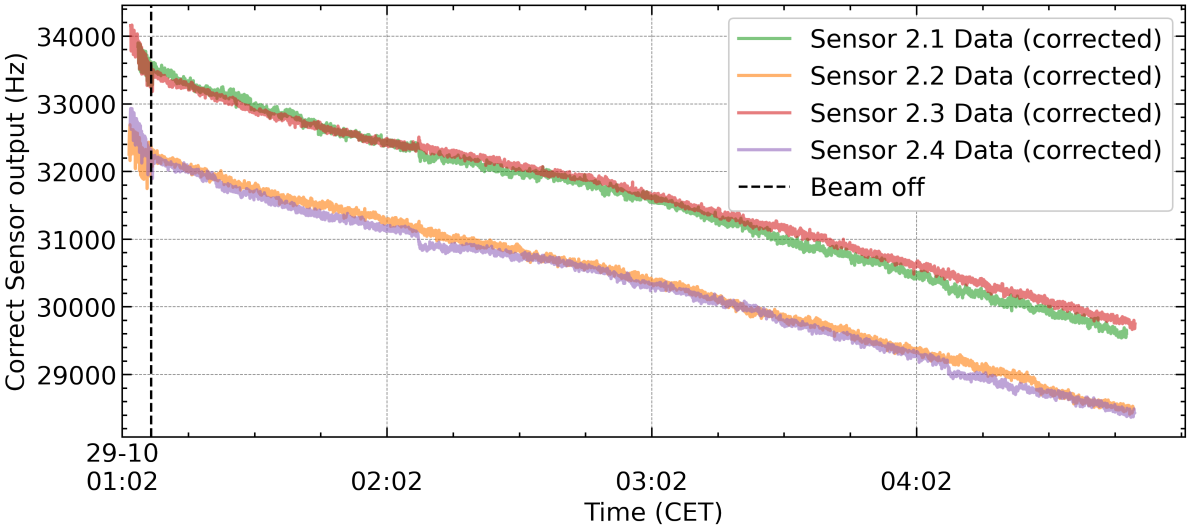

Figure F.2: The temperature-corrected sensor data immediately after the CHARM beam shutdown, with corrections applied for the recharging effect.

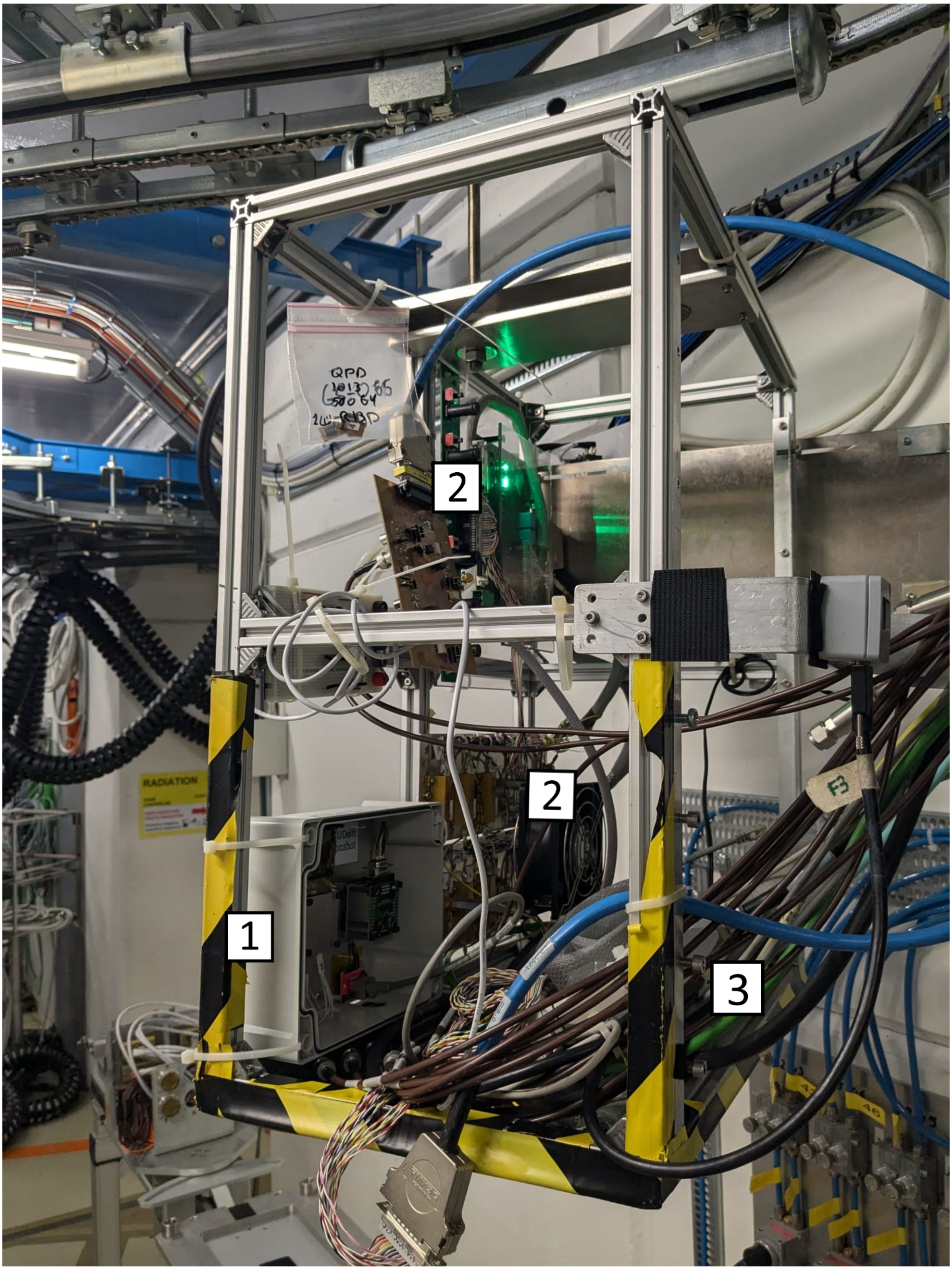

Figure F.3: The CHARM setup in the overhead conveyor. 1) The experimental setup used in this thesis. 2) Other uses setup. Each quadrant had a user. 3) The facility provided wires that allow the setups to connect to the patch panel in the control room.

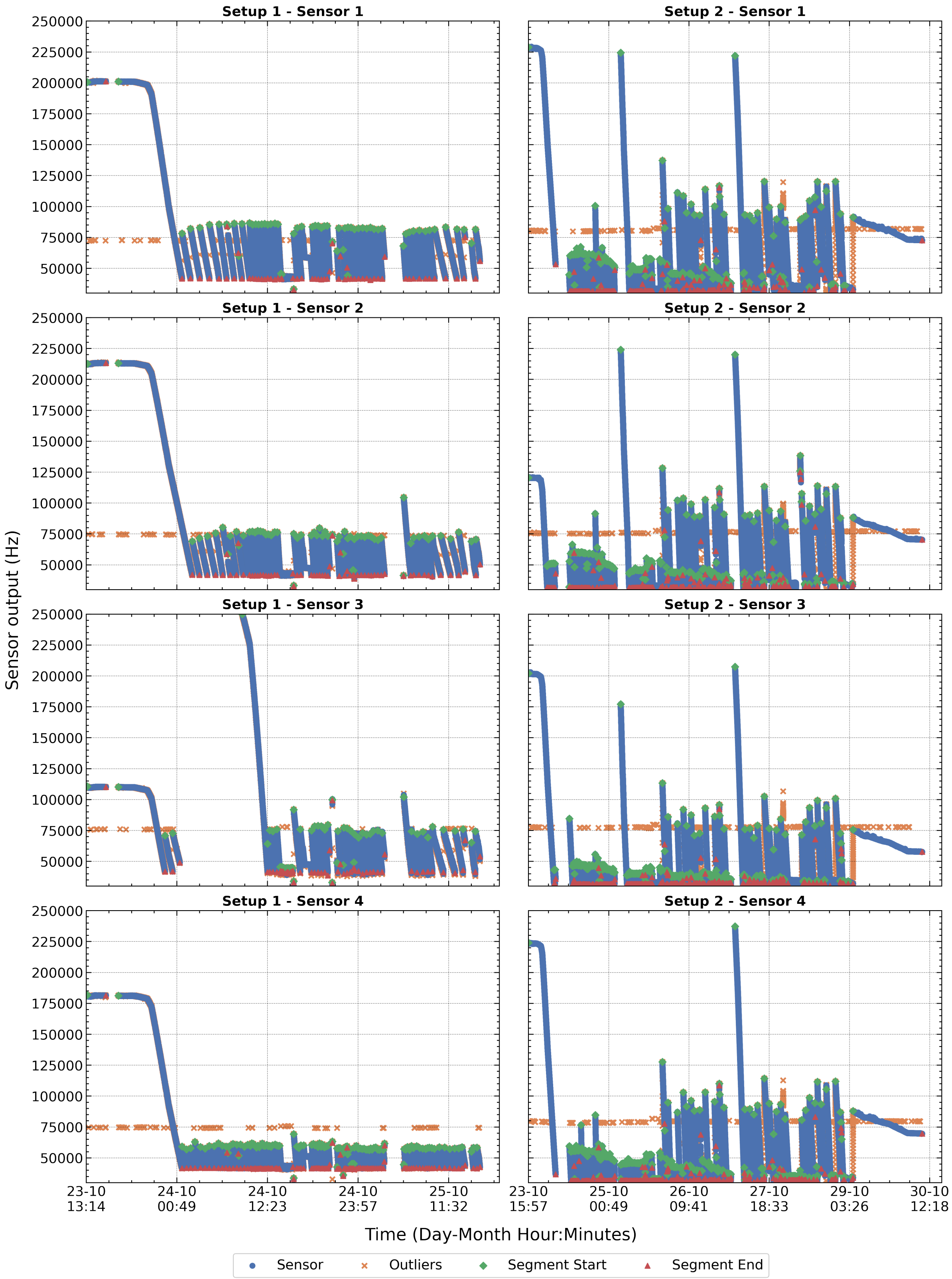

Figure F.4: The raw CHARM sensor data during second irradiation week. Setup 1 experienced a destructive event, resulting in less data compared to Setup 2.

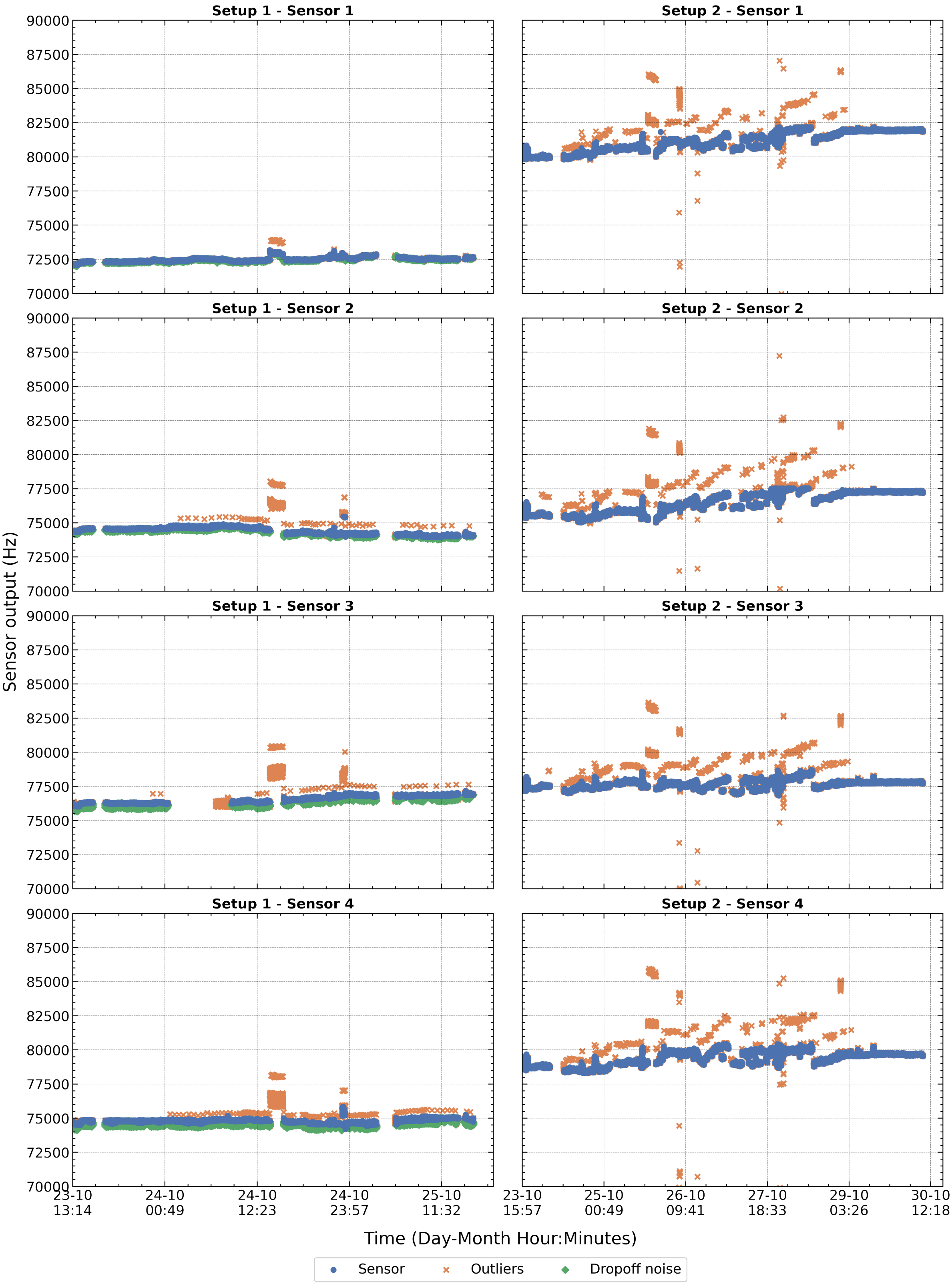

Figure F.5: The raw CHARM reference data during second irradiation week. Setup 1 experienced a destructive event, resulting in less data compared to Setup 2. In addition, setup 1 experiences some drop-off noise, as explained in section 4.4. In Setup 2, further filtering can be applied to reduce upsets and enhance data quality.

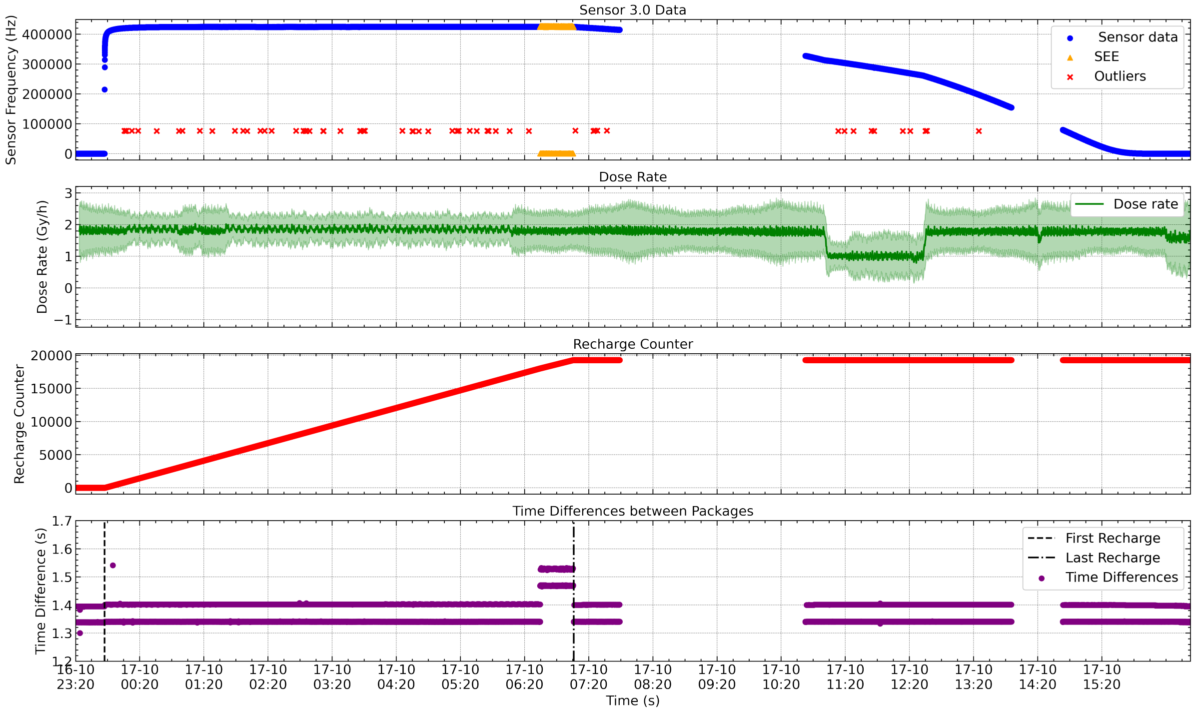

Figure F.6: A SEEs was observed in sensor 1.3 during the first week of the CHARM experiment. The first graph is the sensor output, capturing both the SEEs and the subsequent full discharge. The second graph presents the facility's dose rate, smoothed using a 15-point rolling average, with the 1-sigma uncertainty range highlighted. The third graph displays the recharge counter, a value provided by the sensor. Interestingly, this value increased even though the sensor had not yet completed recharging. Finally, the fourth graph plots the time difference between consecutive data packages.

Figure F.7: EAST area hall schematic [91],located next to the PS. Modified to highlight CHARM Controlled Area, and reduce unrelated details.

G

Timepix for the Lunar Zebro Rover

At the beginning of this thesis, a key question arose: ”Can we replace the current detector with an alternative instrument that enhances the scientific yield?” While the primary goal of the first Lunar Zebro mission is not necessarily to conduct scientific measurements, exploring this possibility for future missions remains an interesting avenue worth documenting.

This appendix serves as an internal memo, outlining the investigation and aiming to document findings while inspiring potential future research.

In 1990, a collaboration between four institutes—the Medipix1 Collaboration—demonstrated the feasibility of using hybrid pixel detectors for photon counting and high-resolution imaging. Over time, further collaborations led to the development of three new generations of Medipix chips, each introducing improvements and new features (released in 1999, 2005, and 2016).[113, 114]

From the second collaboration, two distinct branches emerged:

- The Medipix line, focused on enhancing spatial resolution.
- The Timepix line, which introduced additional functionalities for time or amplitude measurements.

The following sections provide an overview of each of these detector families before proceeding with the analysis.

Medipix

Table G.1 illustrates an overview of the different Medipix chip generations.

The Medipix series integrates data from multiple hits on a pixel and provides images in the form of frames. These chipsets are primarily designed for medical imaging and other photon or particle-counting applications. The approach is frame-based, meaning data is collected over a defined period before being read out, rather than processing each event individually.[115]

Feature	**Medipix**	**Medipix2**	**Medipix3**	**Medipix4**
Tech. node (nm)	1000	250	130	130
Year	1997	2005	2013	2021
Pixel size (µm)	170	55	55	70/140
# pixels (x x y)	64 x 64	256 x 256	256 x 256 / 128 x 128	320 x 320 / 1690 x 160
Charge summing mode	No	No	Yes	Yes
Readout architecture	Sequential R/W	Sequential R/W	Sequential or continuous R/W	Sequential or continuous R/W
# sides for tiling	0	3	3	3

Table G.1: Comparison of Medipix generations[114].

Timepix

Whereas the Medipix series focuses on spatial resolution, the Timepix series is designed to capture and transmit as much information as possible about individual interactions for further off-chip processing.

Feature	**Timepix**	**Timepix2**	**Timepix3**	**Timepix4**
Tech. node (nm)	250	130	130	65
Year	2005	2018	2014	2019
Pixel size (µm)	55	55	55	55
# pixels (x x y)	256 x 256	256 x 256	256 x 256	448 x 512
Time bin (resolution)	10ns	10ns	1.6ns	200ps
Readout architecture	Frame based (sequential R/W)	Frame based (sequential R/W or continuous R/W)	Data-driven or Frame based (sequential R/W)	Data-driven or Frame based (sequential or continuous R/W)
# sides for tiling	3	3	3	4

Table G.2: Comparison of Timepix generations [114]

Unlike Medipix, Timepix operates in an event-based manner, meaning it records information for each detected interaction rather than accumulating data over a fixed time frame. Timepix can operate in three different modes: A) Counting Mode – Counts the number of detected particles per pixel. B) Time of Arrival (ToA) Mode – Records the precise timing of each interaction. C) Time-over-Threshold (ToT) Mode – Measures the duration a signal remains above a predefined threshold. An overview of the different generations is shown in Table G.2.

Companies with Timepix or Medipix licensees

Company	**Activity**	**Country**	**Licensed Technologies**
Advacam s.r.o.	Radiation imaging detectors for the scientific and industrial market	Czech Republic	Medipix2/Timepix, Medipix3, Timepix3
Amsterdam Scientific Instruments (ASI)	Hybrid pixelated detectors for scientific and industrial users	Netherlands	Medipix2/Timepix, Medipix3, Timepix3
Kromek	Radiation detection solutions for applications in the medical, nuclear, and security screening markets	United Kingdom	Medipix2/Timepix
Malvern Panalytical	Materials analysis and non-destructive testing	Netherlands	Medipix2/Timepix, Medipix3
MARS Bio Imaging	X-ray detectors for spectral molecular imaging	New Zealand	Medipix3
Quantum Detectors	Detectors for synchrotron radiation, LASER, and other large-scale facility applications	United Kingdom	Medipix3
X-ray Imaging Europe (XIE)	Semiconductor detectors and electronics for X- and Gamma-rays	Germany	Medipix2/Timepix
X-spectrum	X-ray cameras for high-end research projects at advanced X-ray sources	Germany	Medipix3
PITEC	X-ray cameras for high-end research projects at advanced X-ray sources	Brazil	Timepix2, Medipix3

Table G.3: Companies that have licensees of Medipix and/or Timepix Technologies[113]

G.0.1. For Space Applications

From meetings with Advacam, it became clear that for the Lunar Zebro application, the Timepix2 is the most suitable option. It was also reported to be particularly designed for space applications, where measurements in mixed radiation fields are expected [114]. The Timepix2 consists of a 256 × 256-pixel matrix with a 55 µm pitch[1]. The chip is highly programmable, with 28 bits per pixel, which can be configured as counters of varying depths in different modes for different purposes. It is also possible to power down individual pixels, either to read out only a specific region of interest or when using larger pitch pixel sensors. Data from the pixel matrix is typically output in full frames via either a 100 Mbps serial port or a 3.2 Gbps parallel bus.[116]

---

[1] The distance from the center of a pixel to the adjacent pixel.

G.0.2. Selection of Timepix products

After a quick comparison, the MiniPIX Sprinter, developed by Advacam, was chosen as the starting point for this investigation. This is a compact, high-speed radiation detection camera based on Timepix2. It achieves 99 frames per second with a signal-to-noise ratio (SNR) of 2000.[117]

The device has dimensions of 80 × 21 × 14 mm, weighs over 37 grams, and is controlled via a USB 2.0 interface. It offers three count bit-depth profiles: 10, 14, and 18 bits. The detector is available in silicon (Si) with different thickness options (100, 300, and 500 µm), which influence detection efficiency at higher energies.[117]

The device operates at 5V, consuming 550 mA, resulting in an average power consumption of 2.75 W.[117]

Implications for the Current Rover Design

- RADPAY-SH-1.5 – The power consumption must be below 1 W. This requirement is not met.
- RADPAY-SH-1.6 – The required dimensions must remain below 50 × 50 × 50 mm. This would need to be extended, especially considering that this does not include supporting instruments such as memory and the microcontroller.
- RADPAY-SH-1.7 – The payload shall have a mass lower than 100 g. This requirement is met, but with the addition of supporting hardware, the total mass will likely exceed this limit.

Assuming all pixels are used, with 99 frames per second and an 18-bit depth, this results in a data rate of 10.83 MB per second. However, the data sheet also mentions the possibility of operating at 64 frames per second with a 14-bit depth, which would reduce the data rate accordingly.

Compared to the FGDOS, Timepix would allow for particle type and energy discrimination, significantly increasing the scientific yield. This could be further enhanced by the addition of neutron conversion, as demonstrated by Šagátová et al. [118].

In the current rover design, Timepix would not be a viable fit for the first mission. However, for future missions—potentially involving a swarm-based approach—it could be interesting to introduce different rover roles, a bit similar to an ant colony. Meaning, there could be a "queen" rover, equipped with a more powerful payload containing the Timepix, operating alongside "explorer ant" rovers, fitted with current payload FGDOS.

This, however, requires further research, with several key questions still needing to be addressed.

- How well does the Timepix withstand radiation exposure? What is its maximum TID?
- What is the minimum number of frames required to obtain useful data?
  - Does this change depending on different mission operations?
- How many pixels are needed to extract meaningful scientific insights?
- What thermal constraints does the Timepix impose on the rover design?
- What limitations does data communication introduce to the rover design?
- What power constraints does the Timepix, including its supporting electronics, impose on the rover?
  - How much memory is required?
  - How powerful does the GPU need to be?
  - How much data processing must be conducted on the rover before transmission?
- How can the Timepix be integrated into the rover system?
- Does it require temperature compensation? [119]

H

Neutron and detection of neutrons

In this appendix, the literature on neutrons is explored. This overview remains at a surface level, as the field of neutron research is vast and complex. For a more in-depth understanding, readers are referred to the following sources:

- An Introduction to the Passage of Energetic Particles through Matter by N. J. Carron
- Radiation detection and measurement by Glenn Knoll

As mentioned in section 2.1, neutrons interact with matter through four distinct processes. In the literature, it is common to classify neutron energies using specific designations. However, these classifications are not strictly defined, as they vary between sources and are primarily suggestive of the typical interactions and consequences of neutron reactions. The classification is presented in Table H.1

Energy Range	Name
0–0.025 eV	Cold
0.025 eV	Thermal
0.025–0.4 eV	Epithermal
0.4–0.6 eV	Cadmium
0.6–1.0 eV	Epicadmium
1–10 eV	Slow
10–300 eV	Resonance
300 eV–1 MeV	Intermediate
1–20 MeV	Fast
>20 MeV	Relativistic

Table H.1: Neutron energy classification [120]

The shielding mechanism of neutron radiation is quite complex due to its charge-less nature, making it different from other types of radiation. Neutrons interact with matter through three main phenomena: inelastic scattering, elastic scattering, and neutron absorption. The interaction cross-section of neutrons with an isotope's nucleus depends on the energy of the incoming neutrons. Neutrons above 10 MeV, are subject to inelastic scattering, while neutron between 1 and 10 MeV lose their energy by means of elastic scattering. In contrast, slower (thermal) moving neutrons interact mostly with the nucleus using absorption.[121] On a macro scale the interaction with neutron can be explained using the cross sections σ_{cs} . Assume a beam of neutron, with a spot area of A is heading towards a slab of matter. The slab has a density of ρ with a thickness Δx[122]. Each nucleus in the matter represents a possible target area:

$$\sigma_{cs} = \pi R_0^2, \tag{H.1}$$

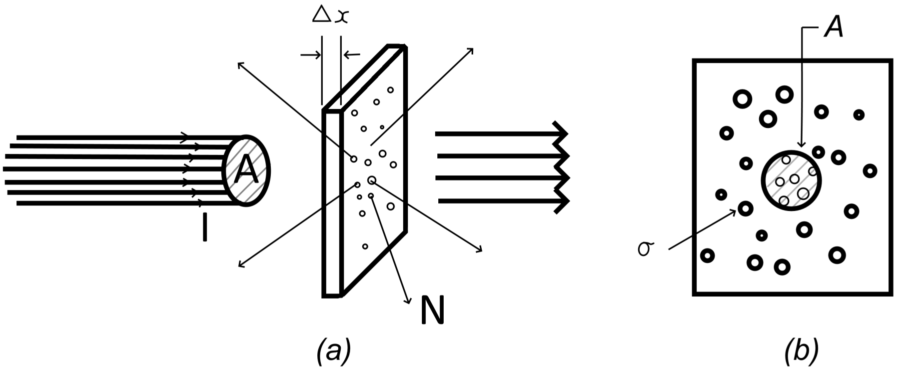

Figure H.1: Basic experimental arrangement to determine the cross-section of a nuclear reaction. a) Side view. b) View along beam direction. recreation based on an image by Burcham [122]

with R_0 the nuclear radius. The total target area then

$$A = \Delta x\ \rho\ \sigma_{cs}. \tag{H.2}$$

The rate of removing neutrons from the beam is proportional to the number of neutrons (N) crossing through A and the total target area, expressed as follows:

$$dN/dt = \varphi \Delta x \rho \sigma_{cs}, \tag{H.3}$$

with φ the neutron flux ($\frac{neutrons}{s \cdot cm^2}$). This can also be expressed as:

$$\varphi = \rho_n \cdot v_n, \tag{H.4}$$

with ρ_n the neutron density per cm^3 in the beam and v_n the relative velocity of neutrons in the beam.

The cross-section for different materials and different energy can be experimentally measured, with σ being defined in ”barns” (b). A barn is equal to $10^{-24}\ cm^2$[19]. The total cross-section of boron-10 and Cadmium are shown in Figure H.2

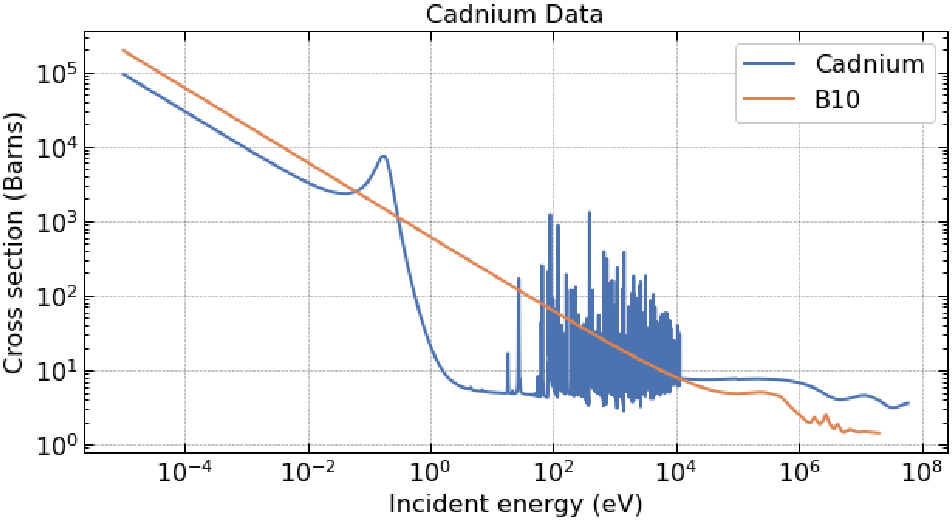

Figure H.2: Total neutron cross-section for cadmium and boron-10. The CENDL-3.2 dataset was used for cadmium, while the JEFF-3.3 dataset was used for boron-10[123].

I

Mathematics of TID in Mixed-fields

This appendix describes the mathematical framework of Total Ionizing Dose (TID) in mixed-field radiation environments.

For this description, the text from Ferraro [86] is used as a baseline. The energy deposited in matter by a single charged particle is commonly expressed using the linear energy transfer (LET):

$$LET = \frac{dE}{dx}|_{iel}, \tag{I.1}$$

describes the rate of energy loss per unit distance travelled.
In CHARM, a mixture of different charged particles are encountered (see Figure 4.2) .With most of the energy coming from heavy charged particles, electrons, and photons. For Heavy charged particles, the LET in silicon with a thickness used in microelectronics is constant, with the average value being calculated by the Berthe-block formula:

$$-\frac{dE}{dx} = 2\pi N_a r_e^2 m_e c^2 \frac{\rho Z}{A_w} \frac{z^2}{\beta^2} \left[\ln\left(\frac{2m_e \gamma^2 \nu^2 W_{\max}}{I^2}\right) - 2\beta^2 - \delta - \frac{2C}{Z} \right]$$

With:

$$2\pi N_a r_e^2 m_e c^2 = 0.1535 \text{ MeV} \cdot \text{cm}^2 \cdot \text{g}^{-1}$$

r_e : electron radius $(2.817 \times 10^{-13}$ cm)
m_e : electron mass $(511$ keV)
N_a : Avogadro's number
Z : atomic number of absorbing material
A_w : atomic weight of absorbing material
z : charge of incident particle
β : v/c of incident particle
ρ : density of absorbing material
γ : $1/\sqrt{1-\beta^2}$: Lorentz factor
δ : density correction
C : shell correction
I : mean excitation potential
$W_{\max}$: maximum transferable energy

Where:

$$W_{\max} = \frac{2m_e c^2 (\beta\gamma)^2}{1 + \frac{2m_e}{M}\sqrt{1+(\beta\gamma)^2} + \left(\frac{m_e}{M}\right)^2}$$

For elections and positrons, the equation changes slightly, as the possibility of a large deflection during collision needs to be taken into account.

For photons, the energy deposited by photons cannot be described by LET, as it can be absorbed in a single interaction or be scattered. For this reason, a common way is to use the mass-energy transfer coefficients, which are the fraction of energy transferred to the medium as a function of the photon energies:

$$\frac{\mu_{en}(E)}{\rho} = \frac{\mu(E)}{\rho} \cdot (1 - R(E)) \tag{I.2}$$

Where $\frac{\mu_{en}(E)}{\rho}$ represents the mass-energy transfer coefficient measured in cm$^2 \cdot$ g^{-1}. The term $\frac{\mu(E)}{\rho}$ is the mass interaction coefficient, which is also given in the same units. The function $R(E)$ indicates the fraction of photon energy that gets transferred during the interaction, taking into account the three main types of photon interactions.

I.0.1. Calculation of TID

The calculation of TID can be defined into two categories: charged particles and photons.

Charge particles

$$TID = K_{Gy} \cdot \frac{LET(E)}{\rho} \cdot \Phi(E) \tag{I.3}$$

Where the TID is in Gy, $\Phi(E)$ is the particle fluence in cm^2 and K_{Gy} is the unit conversion parameter equal to 1.6×10^{-7} Gy · g · MeV^{-1}.

$$TID = K_{Gy} \sum_{p=e^\pm,\pi^\pm,p^\pm,K^\pm,\mu^\pm} \int \frac{LET(p,E)}{\rho} \cdot \Phi(p,E)\, dE \tag{I.4}$$

Photons

The TID deposited by a specific photon fluence for specific energy is calculated by:

$$TID = K_{Gy} \cdot \frac{\mu_{en}(E)}{\rho} \cdot E \cdot \Phi(E) \tag{I.5}$$

In a mixed field, where TID are introduced by the whole photon spectrum, the contribution of all photons is summed:

$$TID = \int K_{Gy} \cdot \frac{\mu_{en}(E)}{\rho} \cdot E \cdot \Phi(E)\, dE \tag{I.6}$$

J

Analysis of the FGDOS sensitivity in a Mixed-field environment: Week two.

Observations in Figure 2.21 indicate that FGDOS degrades as a function of the total dose received. To further analyse the sensitivity as a function of TID, it would be valuable to replicate this result for the experiment conducted in this thesis. In section 4.6, it was demonstrated that this was feasible for the initial data points of the experiment. However, challenges arose in replicating this analysis for the second week.

Before discussing the results, the data filtering process will be explained, followed by the presentation of the results and discussion, and finally, the results will be summarized and concluded.

Data Filtering

As observed in Figure F.4, the degradation in charging speed, along with other operational events, caused the sensor to operate over a wide dynamic range. In addition, fluctuations in the number of protons delivered to the facility were more irregular during the second week compared to the first week, as seen in Figure 4.11. For this reason, a systematic filtering approach is required.

Firstly, only sensor data within the frequency range of 50–90 kHz is considered. As shown in Figure 4.17, the sensitivity varies significantly depending on the operating regime. By keeping the data within this range, the sensitivity can be assumed to be constant, which is also the manufacturer's recommendation [4].

Secondly, the remaining data segments must contain a sufficient number of reported facility points to ensure that the dose rate statistics can be compared. To achieve this, at least five facility points are considered, which corresponds to 118 sensor data points.

Thirdly, in some cases, a data segment may contain two or more significantly different dose rates, which would introduce inconsistencies in the analysis. In such cases, the segment needs to be excluded. As a first-order approach, a linear fit is applied to the data, and if the R^2 value is greater than 0.985, it is assumed that the dose rate remains constant within the segment.

This filtering process is repeated for all eight sensors. Once applied, the dose rate for each selected segment is determined, allowing the sensor response to be correlated with the dose rate. Due to the facility's low sampling rate, the endpoint of a sensor segment does not always align precisely with the reported dose rate. Since the facility provides readings every 45.05 seconds, this can result in a maximum time difference of 22.52 seconds between measurement points, which is not ideal. Nevertheless, the sensitivity can still be determined using Equation 2.10.

Results

Below (Figure J.1), the results are presented. In the first graph, the sensor response is shown, while in the second graph, the corresponding dose rate is displayed. In the background, the raw dose rate

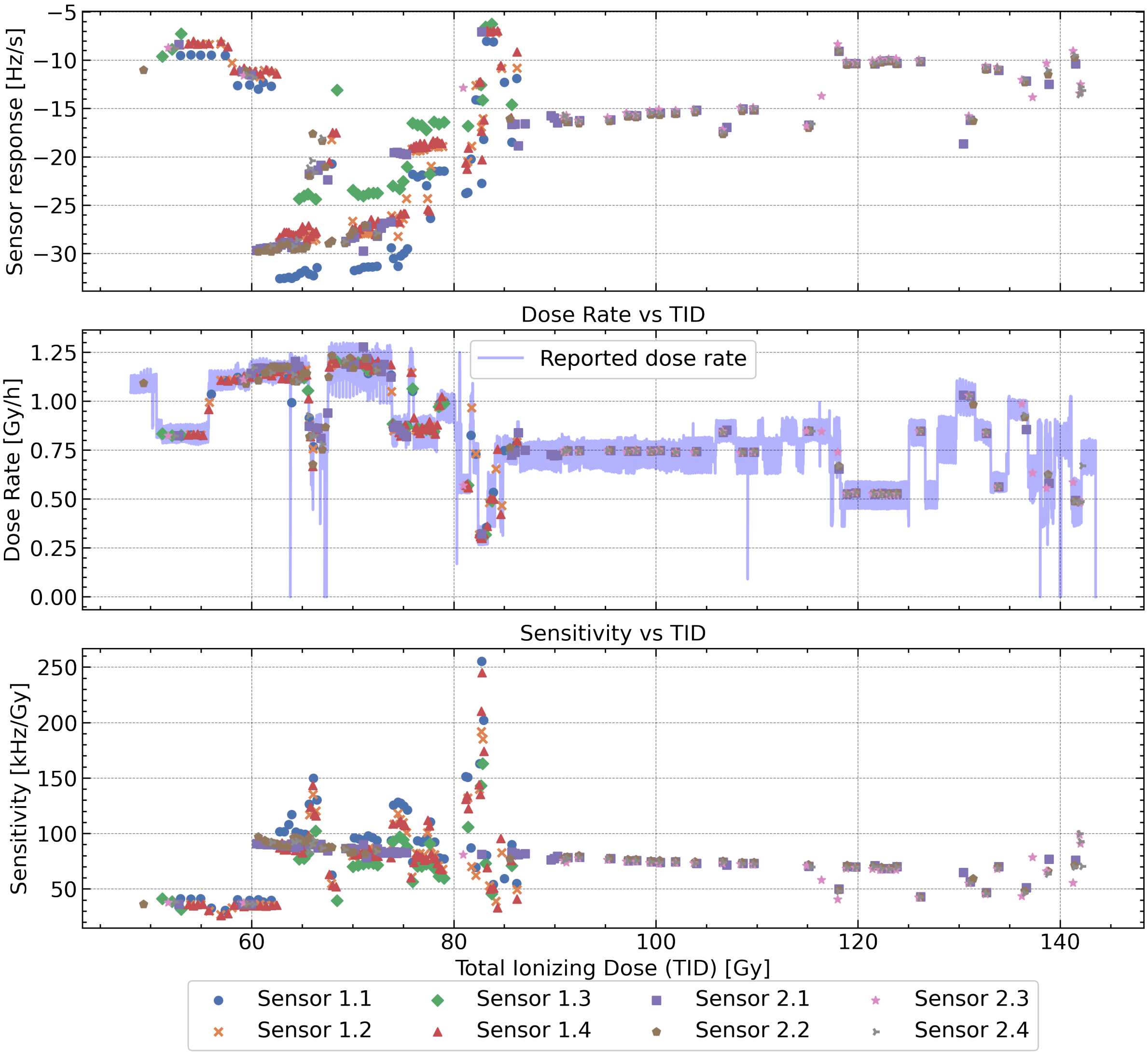

Figure J.1: Sensitivity as a function of Total Ionizing Dose (TID) during the second week at CHARM. The first graph presents the sensor response to the dose rate, which is plotted separately in the second graph. Finally, the third graph illustrates the calculated sensitivity as a function of TID. For clarity, uncertainties are not displayed.

is also shown to highlight possible misalignments between the determined dose rate and the raw dose rate. Finally, the sensitivity is presented. For clarity, the uncertainty is excluded in all plots.

Observing the sensitivity, it becomes evident that the current representation is not entirely realistic. For example, at 85 Gy, a sensitivity of 250 kHz/Gy is observed. If this were accurate, it would be an exceptional result; however, it is more likely that a mismatch between the dose rate and the sensor response has occurred. This discrepancy is probably caused by an underestimation of the actual dose rate, leading to an artificially high sensitivity value.

Another notable observation in the sensitivity data is the presence of a discontinuity jump. This behaviour is unexpected, and the underlying cause remains unclear.

Additionally, setup 2 exhibits significantly less fluctuation in sensitivity compared to setup 1. As described in chapter 4, setup 1 exhibited unexpected noise and high power consumption, which could not be fully addressed before the experiment. These effects may be attributed to these instabilities.

Finally, it is observed that from 60 Gy onward, the sensors in setup 2 exhibit an almost linear decrease in sensitivity, with minor fluctuations toward the end. A stable dose rate is observed from approximately 80 Gy to 110 Gy. A zoomed-in version of the sensitivity is shown in Figure J.2. Observing this result, an

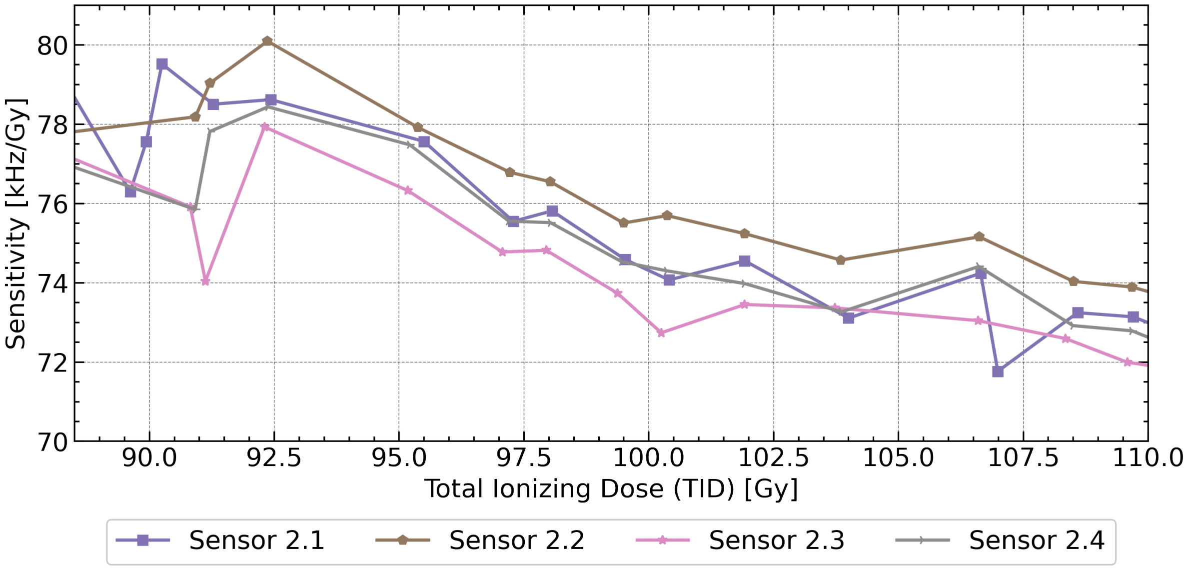

Figure J.2: Zoomed-in version of the sensitivity as a function of the TID. Sensors 2.1 and 2.2 were exposed to 1.5 mm Al and PCB shielding, while sensors 2.3 and 2.4 were exposed to the pure mixed field.

abnormal trend is apparent, as the sensitivity of the control and the shielded sensors has been reversed compared to what was found in previous measurements (see Figure 4.18).

Conclusion

The sensitivity calculations for this week may have been affected by three main factors. Firstly, there is a misalignment between the dose rate measurements and the sensor response, leading to inaccuracies. Secondly, influences such as fluctuations in voltage, temperature, and Single Event Effects (SEEs) may have altered the sensor response. Finally, the dose rate data from the CHARM facility fluctuates too much, and with only five data points per calculation, the results are not stable enough to draw meaningful conclusions. All three factors could be contributing to the observed inconsistencies at each measurement point.

To address these issues, further work is required to check for potential errors in the data processing code and to introduce additional constraints and mathematical methods to refine the calculations. This would help define the necessary post-processing steps and establish guidelines for creating more reliable and user-friendly tools for data analysis during lunar missions.

It is also possible that the fluctuations in both the experimental setup and the facility conditions are greater than currently assumed, making it difficult to extract any meaningful insights from the data or ensure reproducibility. In such a case, the only viable solution would be to repeat the experiment under more stable conditions, minimising variation to improve the reliability of the results.